P-type and N-type Semiconducting Thiophene Copolymers for Organic Electronic Applications

Peter D. Kazarinoff

A dissertation
submitted in partial fulfillment of the
requirements for the degree of

Doctor of Philosophy

University of Washington
2012

Reading Committee:
Professor Christine K. Luscombe, Chair
Professor Fumio S. Ohuchi
Professor Guozhong Cao

Program Authorized to Offer Degree:
Department of Materials Science and Engineering

University of Washington

Abstract

P-type and N-type Semiconducting Thiophene Copolymers for Organic Electronic Applications

Peter D. Kazarinoff

Chair of the Supervisory Committee:
Professor Christine K. Luscombe

There has been considerable research in the pursuit of organic materials to replace inorganic materials in electronic applications because of their advantages in being light weight, flexible, and solution processable over large areas. In this examination, novel p-type and n-type thiophene based semiconducting copolymers have been analyzed. First, a series of three air stable ester-functionalized p-type polythiophenes were tested for their performance in organic thin film transistors. Increased crystallinity as measured by XRD

and DSC accounts for the highest mobility polymer of this series. A HOMO level of 5.6 eV as measured by CV spectroscopy account for the air stability of the polymers over one month. Second, four highly soluble naphthalene diimide (NDI) based n-type polymers are presented - each differing only in the thiophene content comprising the material. Electron mobilities are as high as 0.076 cm^2/Vs for the novel material **PNDI-3Th**. Polymer crystallinity and general macromolecular order was shown to effectively improve by increasing the number of thiophene units along the polymer backbone. The structure-property relationship of NDI-thiophene copolymers is presented as it pertains to organic field effect transistor (OFET) performance. Third, a soluble ladder polymer precursor based on the NDI monomer, **PNDI-2Boc,** was investigated. After solid state ladderization methods were shown to be unsuccessful, a solution derived cyclization method was employed. Electron mobility improves by four orders of magnitude in **PNDI-2BocL** using this ladderization process.

In the fifth chapter, the **PNDI-xTh** n-type polymers are blended with **P3HT** and evaluated as candidate materials in all-polymer OPVs. Spectroscopic techniques including photo-induced absorption spectroscopy are employed and show that polymers **PNDI-1Th** and **PNDI-2Th** are the best candidates. The next chapter discusses a novel use for the **PNDI-xTh** series of polymers, as electron transport materials in inverted polymer solar cells. The polymers are crosslinked and doped in order to improve solvent resistance and electrical conductivity. Devices using this novel interfacial layer show a higher power conversion efficiency compared to devices fabricated with the traditional material, ZnO.

In the final chapter, the NDI monomer is polymerized with a series of fused thiophene monomers to create a series of donor-acceptor polymers. It is shown that as thiophene content increases, the band gap of these materials decrease. OFET devices fabricated from these materials show electron mobilities as high as 1.2×10^{-2} cm^2/Vs.

TABLE OF CONTENTS

LIST OF FIGURES

LIST OF TABLES

1 Introduction to organic electronics

1.1 Organic electronics

There is considerable interest in the design, synthesis, and testing of organic molecules to be used as replacements for inorganic materials in electronic applications.[1-6] These applications include transistors, solar cells, RFID tags, flexible display drivers, and other low-cost electronic circuitry components. Organic small molecules and polymers are advantageous compared to silicon or other inorganic semiconductors in these applications due to their processability from solution over large areas, and tunability of electronic and optical properties by use of different chemical functionalities. However, organic based semiconducting materials present challenges. They typically do not have the same performance as inorganic semiconductors in terms of charge transport. Organic semiconducting materials are less chemically stable than inorganic semiconductors. They are vulnerable to oxidative chemical attack,[7-10] and thermal decay at high temperatures. Accordingly, performance and stability are two important design considerations for semiconducting polymers.

1.2 N-type and p-type organic semiconductors

Silicon is considered p-type or n-type based on the type of dopant atoms incorporated into the crystal lattice. Semiconducting polymers are considered n-type or p-type based

on the majority carrier. The majority carrier in p-type organic semiconductors (also called donors) are holes, while the majority carrier in n-type organic semiconductors (also called acceptors) are electrons. By controlling the chemical and electronic structure of a semiconducting polymer, it is possible to synthesize either n-type or p-type materials. Ambipolar semiconductors operate as both p-type and n-type.

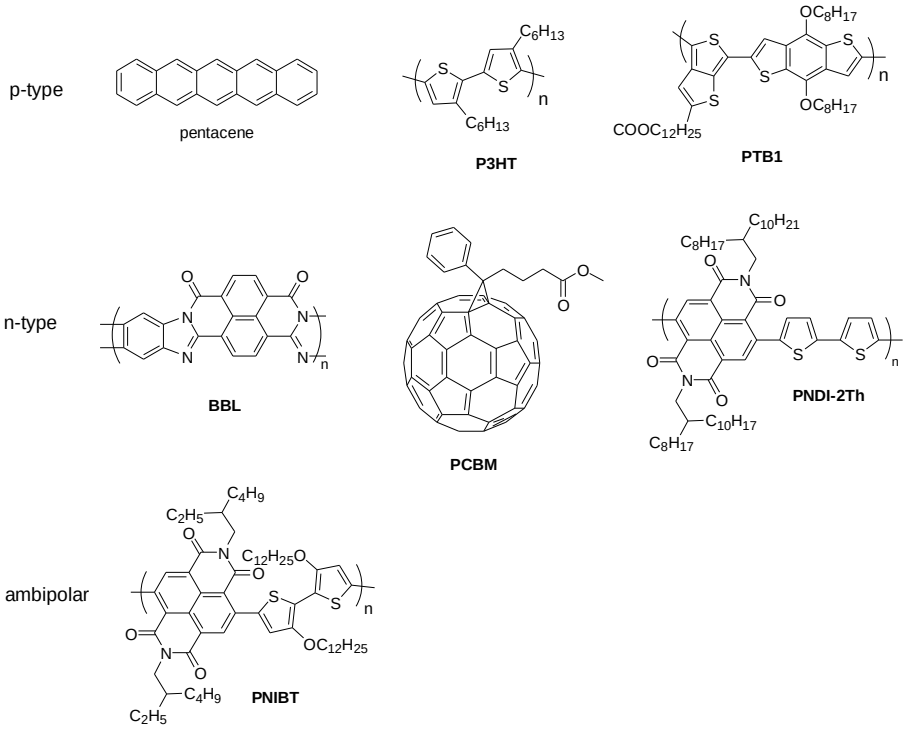

Figure 1.1 Various p-type and n-type organic semiconducting small molecules and polymers[11-16]

The chemical structure of various organic small molecule and polymer semiconductors is shown in Figure 1.1. Small molecule organic semiconductors include pentacene, and phenyl-C_{61}-butyric acid methyl ester (**PCBM**). Examples of p-type and n-type semiconducting polymers include poly(3-hexylthiophene) (**P3HT**) and poly(benzobisimidazobenzophenathroline) (**BBL)**. The naphthalenebiscarboximide-bithiophene polymer (**PNIBT**) has been shown to be amipolar.

1.3 OFET operation

Organic field effect transistors (OFETs) are one device application for semiconducting polymers. They are useful as the component building blocks in complementary inverters and could be applied in the back-plane circuitry of a flexible display. OFETs are also used as a characterization method to determine the charge transport properties of organic semiconductors.

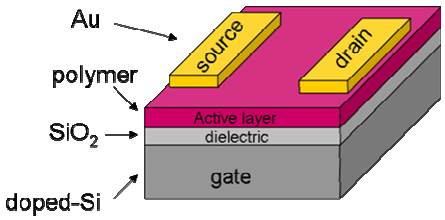

Figure 1.2 Schematic of an OFET in the top-contact geometry

As shown in Figure 1.2, OFETs consist of four layers: a gate electrode, an insulating dielectric layer, semiconducting active layer, and source/drain electrodes. In the top contact geometry shown in the Figure 1.2, the source and drain electrodes are thermally evaporated on top of the active layer. A doped-Si/SiO_2 substrate acts as the gate electrode, insulating dielectric layer, and substrate.

OFETs transport charge in an accumulation mode. Upon the application of a gate voltage, mobile carriers are formed along the dielectric/active layer interface. When a bias is applied between the source and drain electrodes, these charges move, creating a

flow of current. Thus an OFET operates like a switch for current flow, with the gate bias determining whether the switch is on (current flow) or off (no current flow).

The key parameters used to defined the electronic properties OFETs are charge carrier mobility (μ), threshold voltage (V_t) and current on/off ratio ($I_{on/off}$).[17] The field effect mobility in the saturation regime can be calculated using Equation 1.2.1 below:

$$I_{sd} = \frac{W C_i}{2 L} \mu \left(V_g - V_t\right)^2 \qquad \text{Equation 1.2.1}$$

I_{ds} is the source-drain current, W and L are the length and width of the channel, C_i is the capacitance density of the dielectric layer, μ is the charge carrier mobility, V_g is the gate voltage, and V_t is the threshold voltage. The capacitance density is calculated using the capacitance and thickness of the dielectric material as shown in Equation 1.2.2

$$C_i = \frac{C_0}{d} = \varepsilon \left(\frac{\varepsilon_0}{d}\right) \qquad \text{Equation 1.2.2}$$

C_0 is the capacitance of the dielectric material, d is the dielectric thickness, ε is the permittivity of free space, and ε_0 is the dielectric material's dielectric constant. The threshold voltage (V_t) of an OFET is calculated by extrapolating of the linear section of the plot of I_{ds} vs. V_g to where it crosses the x-axis. The on/off ratio ($I_{on/off}$) is calculated by comparing the maximum source-drain current (I_{ds}) in the on-state, typically at V_g = ±100 V for an organic semiconductor, to the minimum source-drain current in the off-state,

usually around $V_g = V_t$. A transfer curve indicating the common OFET parameters is shown in Figure 1.3.

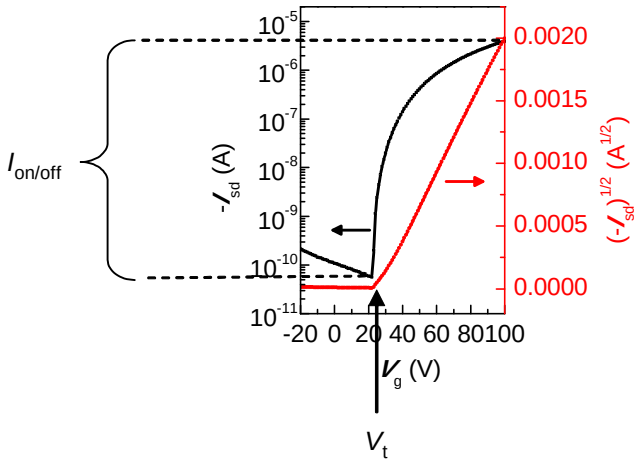

Figure 1.3 Typical transfer curve for an n-type organic semiconductor showing the on/off ratio ($I_{on/off}$) and the threshold voltage (V_t)

1.4 OPV operation

Organic photovoltaics (OPVs) are another device application for semiconducting polymers. Typically, a p-type polymer is used as the electron donor and the light absorber, such as **P3HT**. An n-type small molecule is often used as the electron acceptor, such as **PCBM**. Figure 1.4 shows a schematic of the bulk heterojunction OPV architecture.

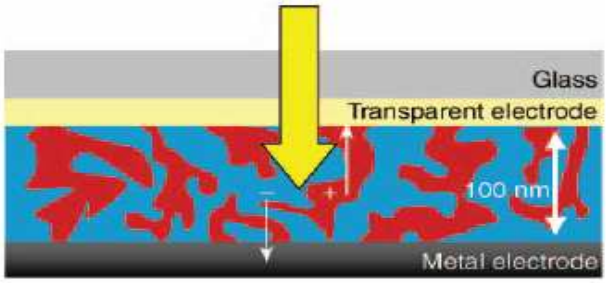

Figure 1.4 Structure of a bulk heterojunction organic photovoltaic device[18]

A photovoltaic operates in a manner similar to an electrical diode. The key difference in a photovoltaic is that additional current flows through the device when it is under illumination. In a diode, when a bias is applied in one direction, the amount of current flow is constant. When a bias is applied in the opposite direction, the current flow increases exponentially according to the relation:

$$J_{dark}(V) = J_o\left(e^{\frac{qV}{kT}} - 1\right) \qquad \text{Equation 1.3.1}$$

Here J_{dark} is the current flow through the device, q is the elementary charge, k is the Boltzman constant, T is the absolute temperature, and J_0 is a constant.

The basic mechanism of OPV cell operation consists of five steps to turn the energy of incoming illumination into a flow of electric current. First, light is absorbed by the material in the active layer. This produces an exciton, which is a bound electron-hole pair. Second, the exciton migrates to an interface between the p-type and n-type materials in the active layer. Third, the exciton separated into free charge carriers by the difference in chemical potential between the donor and acceptor materials. Fourth, these free charges are transported to their respective electrode. Finally, charge extraction at the

anode and cathode completes the process and produces a flow of current. The efficiency of a photovoltaic cell is determined by the amount of energy lost in these five basic steps.

The main metric used to compare photovoltaic device performance is power conversion efficiency (η_e).[19] Power conversion efficiency is the ratio of electrical power generated by the device (P_M) compared to the incident optical power (P_o).

$$\eta_e = \frac{P_M}{P_o} \times 100 \qquad \text{Equation 1.3.2}$$

The amount of electrical power generated by a photovoltaic device is dependent on three key parameters: the open circuit voltage (V_{oc}), the short circuit current (J_{sc}), and the fill factor (FF). The open circuit voltage is the voltage produced by the device when there is no current flow. ($J(V) = 0$). The short circuit current is the current flow under illumination when the device is under zero applied bias ($V = 0$). The fill factor is the ratio of the current and voltage at the maximum power point to the short circuit current and open circuit voltage.

$$FF = \frac{P_M}{J_{sc} V_{oc}} = \frac{J_M V_M}{J_{sc} V_{oc}} \qquad \text{Equation 1.3.3}$$

These three parameters can be used to determine the power conversion efficiency of a solar cell using the equation below:

$$\eta_e = \frac{V_{oc} J_{sc} FF}{P_o} \times 100 \qquad \text{Equation 1.3.4}$$

To increase the performance of a photovoltaic device, all three of these parameters need to be optimized. Figure 1.5 shows a characteristic J-V curve for an OPV device under illumination.

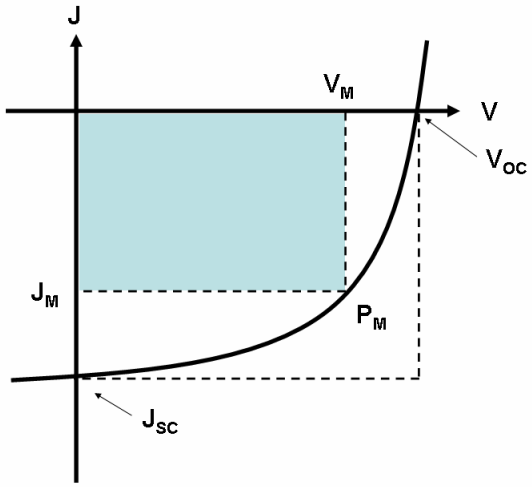

Figure 1.5 Typical I-V curve for a solar cell under illumination showing the common parameters, J_{SC} and V_{OC}. The ratio of the areas of the two squares shown in blue and white equals the fill factor (FF).

OPV cells are tested under standard conditions in order for device results to be comparable. The standard light spectrum used in solar cell testing is the AM 1.5 G solar spectrum, shown in Figure 1.6. The AM 1.5 spectrum takes into account the absorption of isolation by gasses in the earth's atmosphere. The incident power of solar radiation is about 1000 W/m^2.

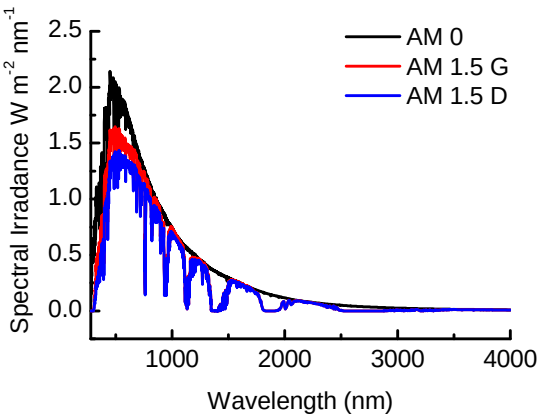

Figure 1.6 AM 1.5 Solar spectrum used in the standardized testing of photovoltaics

2 P-type carboxylated polythiophenes

2.1 Literature review and introduction

A prerequisite for the widespread adoption of organic field-effect transistors (OFETs) is the ability to construct high performance air-stable devices. Air-stability in organic electronics has been pursued in a variety of ways. OFETs made from small molecule oligiothiophene and oligiothiophene derivatives have achieved both high mobility (up to 0.4 cm^2/Vs) and air stability.[20-22] However, these small molecules must be processed using vacuum sublimation, which negates the potential commercial benefits of solution processable organic electronic materials.

In semiconducting polymers, ionization potential determines the resistance to oxidative doping by O_2 and thus, also controls air-stability. As the energy of the highest occupied molecular orbital (HOMO) decreases, the polymer becomes more air-stable. This has been accomplished in a variety of ways. For example, fused ring polymers have been explored, including poly(2,5-bis(2-thienyl)-3,6-dialkylthieno[3,2-*b*]thiophene)[23] which has shown good air stability and high mobility (0.72 cm^2/Vs). Donor-acceptor systems can also be used to change HOMO level and increase air-stability.[24-27] Mobilities up to 2×10^{-2} cm^2/Vs has been reported.[25] Attachment of electron withdrawing groups to the polymer backbone is another method of lowering the HOMO level. Recent work has been done to synthesize air-stable silole-containing thiophene polymers (HOMO levels as low as 5.8 eV) that also exhibit high hole mobilies (up to 0.08 cm^2/Vs).[4] Another method has been to add cyano groups to the polythiophenevinylene main chain yielding materials with hole mobilities in the range of

6×10^{-3} cm^2/Vs.[22] A considerable amount of effort has been invested in synthesizing semiconducting polymers with a variety of oxygen-containing electron withdrawing groups.[24, 30-37] Carboxylated thiophenes are a promising method to decrease the HOMO level of the polymers. Although the electrochemical and optical properties of these materials have been systematically studied, there have been few examples reports on their device performance,[28] and results have not expanded upon the structure-property-performance relationship of these materials in OFET devices.

This work is based on our previously synthesized polymers.[28] Figure 2.1 shows the chemical structure of the ester-functionalized polymers. Our approach was to synthesize several esterified polythiophenes with slightly varying chemical structures in order to test the air-stability and performance of ester-functionalized polymers in electronic devices. We demonstrate that these polymers are air stable, and that all device processing, fabrication, and characterization steps can be conducted in ambient atmosphere with roughly 70% relative humidity without curtailing device performance. By investigating the structure and electronic properties of the three polymers, we can gain insight into the rational design of future ester-functionalized semiconducting polymers.

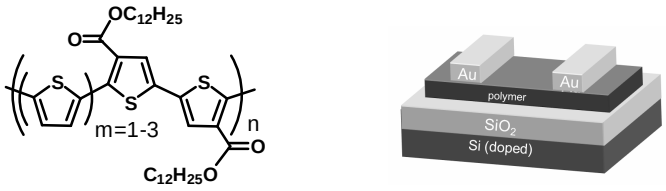

Figure 2.1 (a) Chemical structures of polymers M1, M2 and M3 (b) Schematic view of top contact OFET.

2.2 Synthesis of p-type carboxylated polythiophenes

The synthesis of polymers **M1, M2**, and **M3** are shown in Scheme 1. The three alternating copolymers were prepared via Stille-coupling polycondenstation from didodecyl(5,5'-dibromo-2,2'-bithiophene-4,4'-dicarboxylate) and a tin-functionalized thiophene monomer using our previous procedure.[28] The synthesis of the ester functionalized monomer has been changed to a more reproducible procedure compared to what was previously reported.

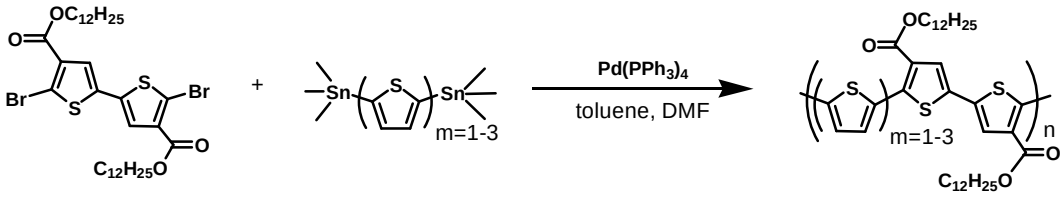

Scheme 1 Synthesis of polymers M1, M2 and M3

The Stille polymerization method was chosen over $FeCl_3$-mediated polymerization[28] because it avoids the step of removing residual $FeCl_3$, which acts as a dopant and increases the conductivity of the final polymer. Carboxylate groups were incorporated into the polymer side chain by design to lower the ionization potential of the polymer. Dodecyl alkyl chains were utilized to increase the solubility. Tin functionalized monothiophene, bithiophene, and terthiothiophene monomers were reacted with the ester functionalized bithiophene to create polymers **M1**, **M2**, and **M3** respectively.

The three polymers were analyzed by ^{1}H NMR as well as GPC-SEC giving a number average molecular weights of 7,100 Da (PDI = 1.6), 6,700 Da (PDI = 1.9) and

5,100 Da (PDI = 1.2) for polymers **M1**, **M2** and **M3**, respectively, as shown in Table 2.1 below:

Table 2.1 Number average molecular weigh (M_n) and polydispersity index (PDI) of polymers M1, M2 and M3

Polymer	M_n	PDI (M_w/M_n)
M1	7,100	1.6
M2	6,700	1.9
M3	5,100	1.2

2.3 Results p-type carboxylated polythiophenes

2.3.1 OFET Characterization

In order to address the feasibility of these polymers as a candidate for the active layer in organic electronics, transistor devices were fabricated from the three polymers. Three rounds of device testing were conducted: devices with freshly synthesized polymers, devices with polymers that had been stored in air for one year, and the latter devices stored in air for one month. These devices were used to evaluate charge carrier mobility, and air-stability, two important performance metrics in OFETs. Figure 2.1 shows the simplified top contact OFET device architecture. **M1**, **M2** and **M3** were all found to exhibit typical p-channel OFET characteristics. The saturated field-effect mobility (μ_{sat}) of each polymer was calculated in the saturation regime from the linear $(-I_{ds})^{½}$ versus V_g curves using equation 1.2.1 below:

$$I_{ds} = \frac{W C_i}{2L} \mu \left(V_g - V_t\right)^2 \qquad \text{Equation 1.2.1}$$

In equation 1.2.1, V_g is the voltage between the gate and source electrodes, V_t is the threshold voltage, L is the channel length, W is the channel width, and C_i is the capacitance density. The air-stability was investigated by measuring the mobility of the year-old polymers in devices, and then measuring the mobility of these devices again over the course of a month. All OFET devices made from the ester-functionalized polymers were processed, fabricated, and tested in air with ~70% relative humidity.

Table 2.2 OFET data for M1, M2 and M3 devices fabricated in air. μ_{sat}, saturation field-effect mobility; V_t, threshold voltage; and $I_{on/off}$, on-off current ratio

	Immediatelyafter fabrication			Stored for one month in air		
Polymer	μ_{sat} (cm^2/Vs)	V_t (V)	$I_{on/off}$	μ_{sat} (cm^2/Vs)	V_t (V)	$I_{on/off}$
M1	$3.3 \times 10^{-3} \pm 5 \times 10^{-4}$	-5	10^5	$1.2 \times 10^{-3} \pm 5 \times 10^{-4}$	-12	10^4
M2	$2 \times 10^{-4} \pm 1 \times 10^{-4}$	-8	10^5	$1.2 \times 10^{-4} \pm 5 \times 10^{-5}$	-8	10^4
M3	$4 \times 10^{-4} \pm 1 \times 10^{-4}$	-5	10^3	$1.0 \times 10^{-4} \pm 5 \times 10^{-5}$	-3	10^3

Figure 2.2 shows the transfer curve and output characteristics of the **M1** and **M3** polymer OFETs tested immediately after fabrication with year-old polymers. Both the freshly synthesized polymers and year-old polymers showed the same performance in terms of hole mobility and on/off ratios ($I_{on/off}$). The summary of all OFET measurements obtained from the year-old **M1**, **M2**, and **M3** polymers are listed in Table 2.2. The mobility measurements represent an average of at least 6 devices. As seen in Table 2.2, **M1** polymer based devices exhibited an average saturation field-effect mobility (μ_{sat}) of 3.3 ×

10^{-3} cm^2/Vs and an on/off current ratio ($I_{on/off}$) of 10^5. The mobility of the **M1** polymer stayed within the same order of magnitude once placed in a device and left in ambient air over the course of one month. However, the on/off current ratio decreased by one order of magnitude. This indicates that the **M1** polymer is an air-stable material. In addition, the year-old **M2** and **M3** polymers maintained similar mobilities over the course of one month. Both stayed within the same order of magnitude over this storage period. The on/off ratio of the **M2** polymer decreased from 10^5 to 10^4. The **M3** polymer maintained the same on/off ratio over the course of one month (10^3).

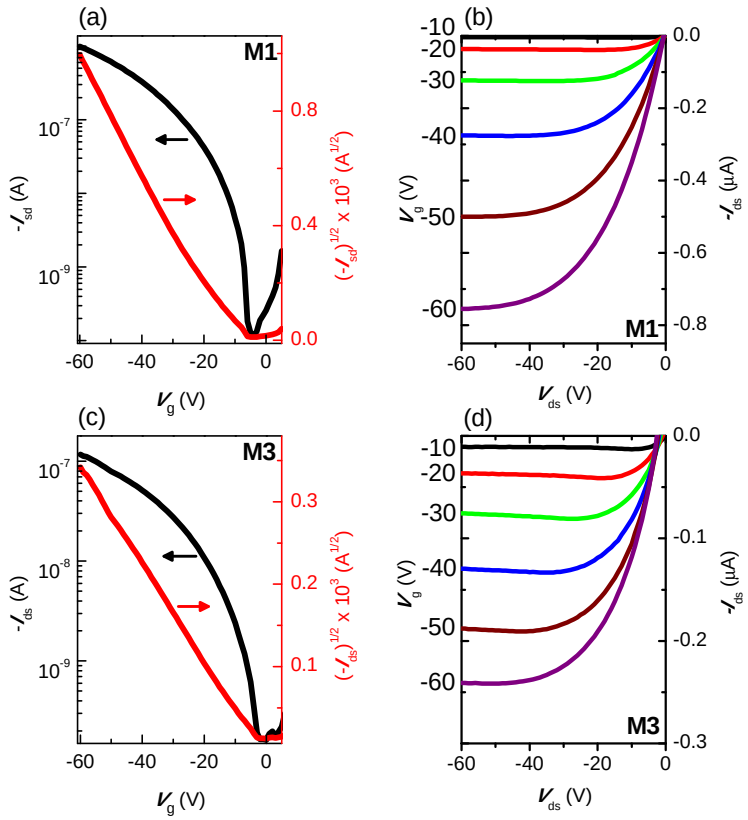

Figure 2.2 Electrical characteristics of p-type OFETs. Transfer curves [$-I_{ds}$ vs. V_g and $(-I_{ds})^{1/2}$ vs. V_g] for M1 (a) and M3 (c). Output curves (V_{sd} vs. $-I_{ds}$) at various gate voltages for M1 (b) and M3 (d).

By comparison, devices fabricated from freshly-synthesized **P3HT** showed an initial mobility of 3.0×10^{-3} cm^2/Vs, but over the course of one month, these devices completely lost their functionality, and were rendered inoperable due to oxidative doping, which increased the off state of the devices.[28-31] The **M1**, **M2**, and **M3** polymers maintain high on/off ratios and mobilities within the same order of magnitude over the same period. They show air-stability which is considerably higher than **P3HT**. The mobility of **M1** (3.3×10^{-3} cm^2/Vs) was significantly higher than the mobility of **M2** (2×10^{-4} cm^2/Vs) and **M3** (4×10^{-4} cm^2/Vs). The explanations for their increased air-stability and performance were investigated using various characterization methods below.

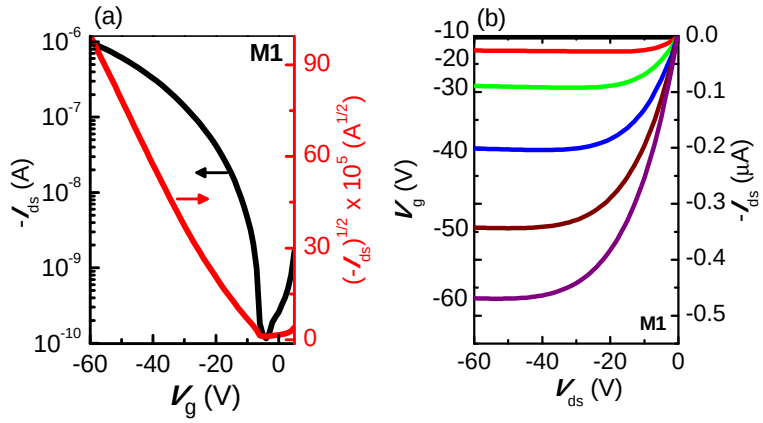

Figure 2.3 Electrical characteristics of M1 p-type OFETs stored in air tested one month after fabrication. Transfer curve (a) and output curves (b).

2.3.2 Air-stability

In semiconducting polymers, air stability is controlled by ionization potential, or IP. In alkyl substituted polythiophenes poor air-stability is due to oxidative doping by O_2, which decreases the on/off ratio by shifting the off-current and also shifts the threshold voltage.[29-31] This results in increased conductivity, and poor performance in transistor

devices. Cyclic voltammetry (CV) was used to determine the HOMO levels of **M1**, **M2** and **M3**. Measurements were made at room temperature in a standard three electrode electrochemical cell made from a working electrode (Pt), reference electrode ($Ag/AgNO_3$ referenced against ferrocene), and a counter electrode (Pt). A 0.1 M solution of tetrabutylammonium hexafluorophosphate ($TBAPF_6$) in acetonitrile was used as electrolyte. Polymer films were made by dipping a working Pt electrode in a $CHCl_3$ solution of the polymer, then annealing the electrode on a hot plate, under a nitrogen atmosphere for 20 minutes. After bubbling the electrolyte solution with nitrogen gas for 10 minutes, a scan rate of 50 mV/s was employed for all measurements.

Each polymer showed a chemically reversible redox process in the positive direction, with small fluctuations in peak height which stabilized after approximately four scans. The CV of ferrocene was conducted immediately after the polymers were measured, and used as an internal standard. The HOMO level of all three polymers was calculated from the onset potentials determined by the intersection of two tangents drawn at the rising current and background current of the cyclic voltammograms (Figure 2.4), and using 4.8 eV as the reference energy level of ferrocene compared to vaccum.[32]

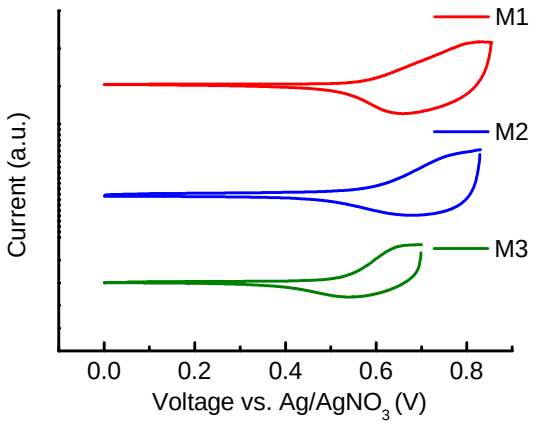

Figure 2.4 Cyclic voltammograms of M1, M2 and M3 polymer thin films on a Pt working electrode vs. a standard Ag/$AgNO_3$ reference electrode

On the basis of the potential of these oxidation onsets, the HOMO level of the **M1** and **M2** polymers was found to be -5.6 eV, while the HOMO level of the **M3** polymer was found to be -5.5 eV. The lower HOMO level of **M1** and **M2** compared to **M3** can be explained by the fact that these polymers have a higher ratio of ester groups per thiophene unit compared to **M3**. As seen in Table 2.3, all of the polymers show HOMO levels lower than **P3HT** (-5.2 eV).[33] Although the measured HOMO level of the **M3** polymer is lower than either **M1** or **M2**, there was no substantial difference in the air stability of OFET devices made out of each.

Table 2.3 Optical properties and energy levels of polymers M1, M2, and M3

Polymer	λ_{max} solution[a] (nm)	λ_{max} thin film[b] (nm)	E_g thin fim (eV)	Peak oxidation potential[c] (V)	Onset oxidation potential[c] (V)	HOMO[d] (eV)
M1	451	519	1.97	0.84	0.62	-5.6
M2	470	536	1.93	0.84	0.59	-5.6
M3	473	526	1.95	0.70	0.54	-5.5

[a]Measured in dilute $CHCl_3$ solution. [b]Thin films spin cast from $CHCl_3$ solution. [c]Oxidation potentials vs. $Ag/AgNO_3$. [d]Calculated using the oxidation potential onset compared to ferrocene

The band gaps of the three polymers were determined using thin film UV-Vis absorption onsets (Figure 2.5) because the irreversible reduction cycles decomposed the p-type polymers during CV measurements. When spun cast from $CHCl_3$ as a smooth and continuous thin film, the **M1** film spectrum showed an absorption onset at λ = 628 nm, corresponding to a band gap of 1.97 eV. The **M2** polymer film showed an absorption onset at λ = 640 nm or 1.93 eV, similar to the **M3** polymer which showed an absorption onset at λ = 637 nm (1.95 eV). The thin films of the **M3** polymer were smooth and continuous, but displayed a slightly cloudy appearance. Annealing the films had no effect on the thin film absorption spectra.

The UV-Vis absorption spectra of the polymers in dilute chloroform solutions were also recorded (Figure 2.5). The **M1** polymer dissolved in $CHCl_3$ solution showed an optical absorption band starting at λ = 552 nm, corresponding to a band gap of 2.25 eV. The red shift in the thin film absorption spectra of these polymers, compared to the solution spectrum, suggests molecular organization in the thin film phase. The polymers had similar changes between the thin film and solution absorption edges with respect to one another. This is due to the planarization of the polymer chain as a result of solid-state

packing which decreases the band gap of the polymer. Due to some aggregation of the **M3** polymer in solution (as compared to the solid-state spectrum), **M3** displayed weaker absorbance than the other polymer solutions. The results are summarized in Table 2.3.

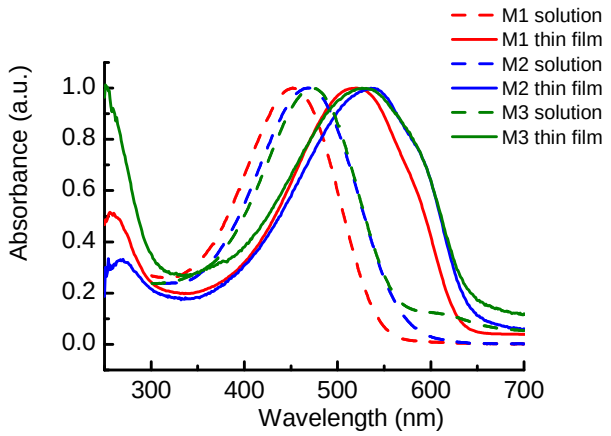

Figure 2.5 UV-Vis absorption spectra of M1, M2 and M3 thin films (solid lines) and in dilute chloroform solution (dotted lines).

2.3.3 Structure

Differential scanning calorimetry (DSC) was performed in order to determine any thermal transitions of the polymers. The samples were heated and cooled at 5 °C/min under a nitrogen atmosphere. Polymers **M1** and **M2** show a sharp endothermic transition upon heating at 180 °C. Upon cooling, **M1** crystallizes at 177 °C and **M2** at 170 °C. Polymer **M3** shows a broader, less distinct endothermic transition upon heating at 156 °C (barely visible by DSC), and undergoes a broad transition at 150 °C when cooling. These endotherms and exotherms are reversible over many cycles. The **M3** polymer shows less defined thermal crystalline transitions compared with the **M1** and **M2** polymers. This indicates that it has a more amorphous structure in the bulk compared to the others, and supports the XRD data, which suggests the difference in mobility is due to crystallinity.

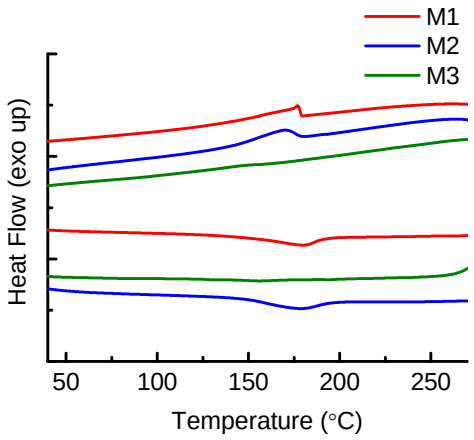

Figure 2.6 Differential scanning calorimetry of polymers M1, M2 and M3

The level of crystallinity in the polymers was confirmed using X-ray diffraction (XRD). Previous studies have suggested that an increase in crystallinity in semiconducting polymer thin films leads to higher mobility.[11, 34, 35] In these air-stable polymers, **M1** had the highest mobility of the series. To account for this, the comparative crystallinity and microstructural order of the three polymers were investigated using X-ray diffraction (XRD). The three polymers were drop cast on Si/SiO_2 wafers (as used in the OFET devices) from *o*DCB solution, and dried in the presence of solvent vapor to produce uniformly thick films. The **M1** film was annealed at 200 °C, **M2** at 180 °C, and **M3** at 170 °C.

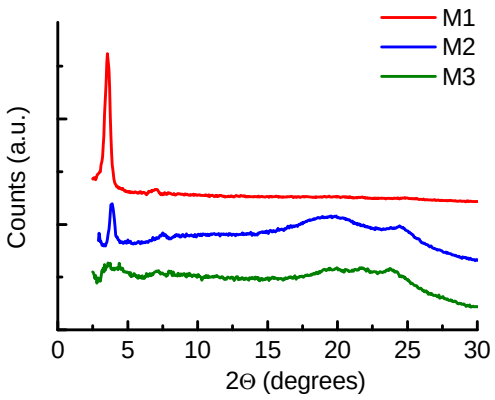

Figure 2.7 Thick film XRD patterns of polymers M1, M2 and M3

Polymer **M1** shows distinct diffraction peaks at 2θ = 3.5° and 2θ = 7.0°. These correspond to an inter-chain d-spacing of 24.7 Å and 12.6 Å respectively. A very small peak can be observed at 2θ = 24.7°. This corresponds to the π-π stacking distance of the **M1** polymer which falls in the range of π-π stacking distances observed in other thiophene polymers (3.5-3.8 Å).[11, 36] As demonstrated by the XRD spectra, the **M1** film is also highly oriented such that the main chains are near to perpendicular to the plane of the substrate. The **M2** evinced similar (100) and (200) peaks to **M1** at angles of 2θ = 3.9° and 2θ = 7.5°. The orientation of the **M2** main chains compared to the substrate is less clear than for **M1**. However, the π-π stacking reflection appears stronger in the **M2** film than in the **M1** film. In addition, the side to side packing in **M2** is not as pronounced as in **M1**. This is likely due to the crystallinity difference in **M2** compared to **M1**, as suggested by the DSC discussion above, rather than a predominate orientation where the **M2** main chains are parallel to the substrate. In the **M2** spectra**,** a broad amorphous region is visible between 2θ = 15° and 2θ = 22°.

The **M3** polymer shows only one distinct diffraction peak at a low angle of 2θ = 3.7° corresponding to an inter-chain d-spacing of 23.8 Å. The **M3** XRD spectra also contains a broad amorphous region between 2θ = 16° and 2θ = 23° similar to the **M2** film. The increase in crystallinity of the **M1** polymer compared to either the **M2** and **M3** can account for **M1** having the highest mobility of the three polymers. A summary of the XRD results can be found in Table 2.4. Overall, the XRD data and DSC data are in agreement with the trends in hole mobilities, which suggest that the respective polymer mobilities are dictated largely by the polymer crystallinities.

Table 2.4 Thick film XRD analysis of polymers M1, M2 and M3 on Si/SiO_2 wafers

M1[a]		**M2**[b]		**M3**[c]	
Angle 2θ	d-spacing	Angle 2θ	d-spacing	Angle 2θ	d-spacing
3.5°	24.7 Å	3.9°	22.7 Å	3.7°	23.8 Å
7.0°	12.6 Å	7.5°	11.7 Å		
24.7°	3.6 Å	24.4°	3.7 Å		

[a]Annealed at 200 °C. [b]Annealed at 180 °C. [c]Annealed at 170 °C

2.3.4 Conclusion

We have synthesized three ester-functionalized thiophene based polymers for use in OFET devices. All three polymers have low ionization potentials of around -5.6 eV as measured by CV. This results in air-stable devices which can be left in ambient conditions without a substantial decrease in performance. The **M1** polymer was the most crystalline of the series as characterized by XRD and DSC. As a result, it has the highest

mobility of the series (3×10^{-3} cm^2/Vs). The use of ester functionalities in polythiophenes shows promise as a way to enhance long term air-stability and performance of OFETs.

3 N-Type PNDI thiophene copolymers

3.1 Introduction

3.1.1 Literature Review

Growth in the field of organic electronic materials and devices has led toward the development of new high performance semiconducting polymers.[1, 23, 37, 38] Polythiophenes, such as poly(3-hexylthiophene)[11, 39] and fused polythiophenes, such as poly(2,5-bis(3-alkylthiophen-2-yl)thieno[3,2-b]thiophene[3] have shown promise in terms of performance with measured hole mobilities of 0.1 cm^2/Vs and 0.60 cm^2/Vs respectively. Comparatively, there has been less development in the pursuit of high performance n-type polymers. In a photovoltaic device, the poor charge transport properties of the acceptor (n-type) material will ultimately decrease the performance of a device, regardless of the performance of the donor (p-type) material. There is a need to develop new high performing n-type materials.

Semiconducting materials with strong electron-withdrawing groups comprising the structure have been used to develop n-type functionality within solution processable polymers based-on naphthalene[40, 41] and perylene diimide[42-45] as well as the ladder-polymer BBL[46] and others.[40, 47] Naphthalene diimide (NDI) polymers in particular have begun to attract a great deal of attention with the recent report of a soluble naphthalene diimide-bithienyl copolymer capable of being used in printable electronics applications and achieving organic field-effect transistor (OFET) electron mobilities reported up to 0.85 cm^2/Vs using top-gate bottom-contact device architectures with polymeric

dielectrics.[48] An NDI-functionalized thiophene copolymer yielding high-performing ambipolar OFET devices was also recently reported in literature.[12] These developments with regard to n-type semiconductor performance provide further support and incentive toward the fabrication of complementary circuits possessing enhanced performance and device operation.[49, 50]

Further development into this chemical architecture is examined and presented in this report through the synthesis and characterization of a series of soluble high performance naphthalene diimide-core donor-acceptor based polymers (**PNDI-0Th**, **PNDI-1Th**, **PNDI-2Th**, and **PNDI-3Th** shown in Figure 3.1 possessing n-type character. Electron mobilities as high as 0.076 cm^2/Vs for the material **PNDI-3Th** were achieved using top-contact bottom-gate organic field-effect transistor (OFET) architectures with SiO_2 as the dielectric.

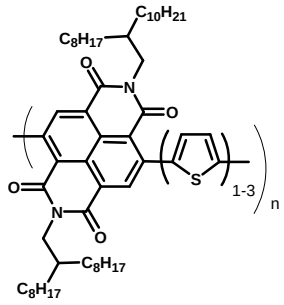

Figure 3.1 Chemical structure of n-type PNDI-thiophene based copolymers.

3.1.2 Synthesis of PNDI-thiophene copolymers

The monomers used to synthesize the four NDI-polymers were synthesized using standard literature procedures—specifically, NDI-Br_2,[13, 41, 48, 51] and the stannylated thiophenes, **1**,**2** and **3**.[41, 52]

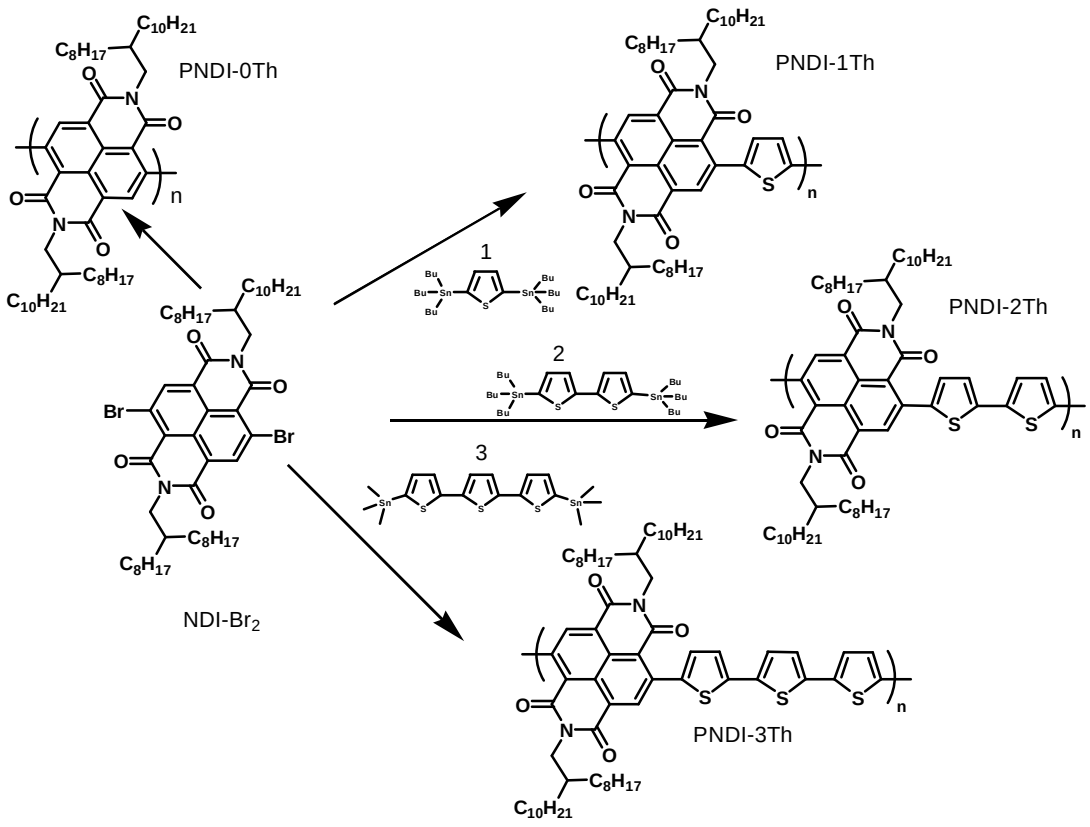

Figure 3.2 Synthesis scheme for the PND-xTh series of n-type thiophene copolymers from the NDI-Br_2 monomer

The highly electron-deficient naphthalene diimide (NDI) acceptor unit with branched-alkane, octadodecyl-, solubilizing groups was copolymerized with stannylated thiophene, bithiophene, and terthiophene donor units using Stille conditions and $Pd(PPh_3)_2Cl_2$ as catalyst to form the **PNDI-xTh** copolymers. The homopolymerization was performed via Yamamoto coupling conditions using $Ni(COD)_2$/bipy as catalyst to produce **PNDI-0Th**.

3.2 Results and discussion

3.2.1 Optical properties and energy levels

Optical absorption spectra shown in Figure 3.3 were taken for all four polymer films spin-cast from $CHCl_3$ onto glass revealing a progressive red-shifting of the absorption band (with increasing thiophene units in the polymer chain) from λ_{max} = 426 nm for **PNDI-0Th** to λ_{max} = 742 nm for **PNDI-3Th**. This shift reveals an effective π-conjugation length elongation likely due to the improved rigidity and planarization of the polymer as a result of the strong π-π interactions of the thiophene units. [53, 54] It was noted from the UV-Vis absorption spectrum that the conjugation length of the homopolymer does not appear to increase when cast into the thin film state. This is likely due to the poor π-π packing of the material as a result of the bulky octadodecyl solubilizing chain interference generating twists to the polymer backbone.

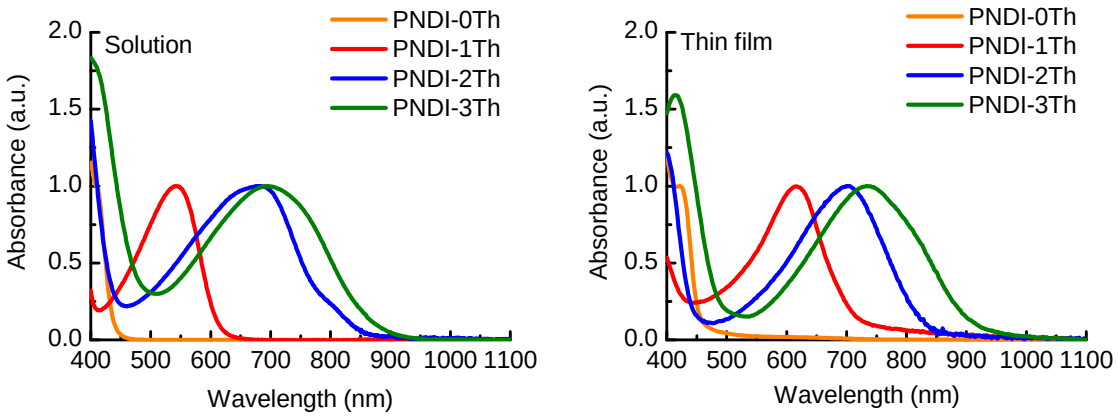

Figure 3.3 UV-Vis absorbance spectra of PNDI-xTh polymers in solution (left) and thin film (right)

The chemical energy levels of the polymer series were investigated using cyclic voltammetry (CV). The LUMO energy levels were calculated from the onset of the first polymer reduction peak. The reproducibility of these reduction scans is an encouraging sign that the **PNDI-xTh** polymers will operate as n-type semiconductors as they are able to stabilize the extra negative charge. Measurements were carried out in a standard three-electrode electrochemical cell employed with a platinum working electrode and a $Ag/AgNO_3$ reference electrode while using ferrocene as an internal standard. The energy level referenced for ferrocene compared to vacuum was 4.8 eV.[32]

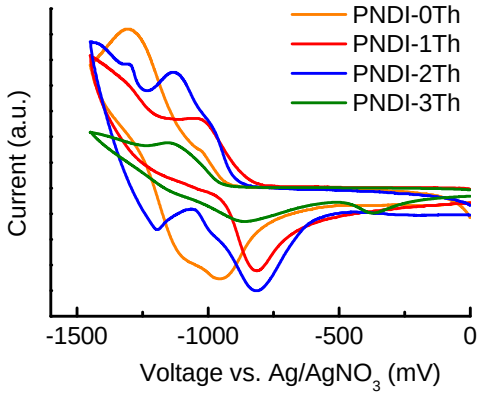

Figure 3.4 Cyclic voltammograms of PNDI-xTh polymers. Voltages are referenced vs $Ag/AgNO_3$

From the scans shown in Figure 3.4, the LUMO values for all four polymers were found to be approximated to ~-3.8 eV due to the intrinsic properties of NDI.[13, 48] The HOMO values were calculated using the optical band gap (E_g^{opt}) from the calculated LUMO. The compiled data is presented in Table 3.1. The electronic properties of the NDI constituting the LUMO of the polymer and the thienyl unit affecting the HOMO and E_g^{opt} of the material were further confirmed by reports stating similar values for related materials.[55-57]

It is noted that specific tuning of the band gap and HOMO of NDI-based polymers can be achieved by altering the thienyl content of the bulk structure which is similarly achieved in polyfluorenes.[58]

Table 3.1 Optical properties and energy levles of PNDI-xTh copolymers. HOMO levels were calculated using the optical thin film band gaps.

	soln λ_{max} (nm)	film λ_{max} (nm)	E_g^{opt} (eV)	$E_{1/2red}$ (V)	LUMO (eV)	HOMO (eV)
PNDI-0Th	409	426	2.74	-0.93	-3.76	-6.50
PNDI-1Th	548	623	1.77	-0.84	-3.85	-5.62
PNDI-2Th	672	696	1.50	-0.90	-3.79	-5.30
PNDI-3Th	701	742	1.37	-0.94	-3.76	-5.13

3.2.2 OFET Characterization

OFET devices were fabricated using the four polymers in the typical top-contact bottom-gate geometry on octadecyltrichlorosilane (OTS) treated doped-Si/SiO_2 wafers. The active layer of the devices was spin-cast from a 98:2 v/v solution of $CHCl_3$ and *o*DCB. The polymers produced optically smooth and continuous films. All fabrication and testing was performed in an inert nitrogen atmosphere. All four polymers showed n-type behavior at positive gate-source biases (V_g = +100 V). The polymers did not display ambipolar or p-type response, with low current flow and on/off ratios below 10 when a negative gate-source bias was applied (V_g = -100 V). The saturated charge carrier mobility of the four polymers was calculated using the saturation current equation: $I_{ds} = (\mu W C_o / 2L)(V_g - V_t)^2$.[59] Transfer curves can be seen in Figure 3.5.

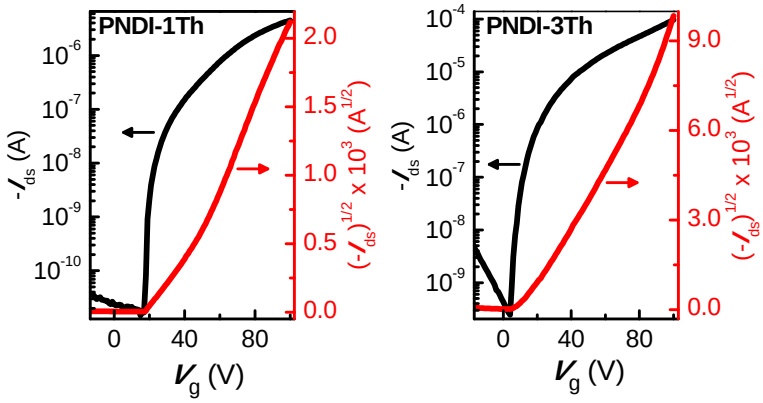

Figure 3.5 Transfer curves of PNDI-1Th (left) and PNDI-3Th (right) at a constant source-drain voltage of +100 V plotted with the square root of current as a function of gate voltage

A linear fit was applied in the saturation region of the $I_{ds}^{1/2}$ vs V_g curve of each of the polymers in order to calculate the mobility. An electron mobility (μ_e) as high as 0.076 cm^2/Vs was measured for OFETs produced from **PNDI-3Th** (Figure 3.5). As shown in Table 3.2, **PNDI-3Th** was found to possess the highest charge carrier mobility which was closely followed by **PNDI-2Th** (3.9×10^{-2} cm^2/Vs). This value is comparable to a prior report in which the mobility for **PNDI-2Th** was measured to be ~6.0×10^{-2} cm^2/Vs for devices using similar architectures.[19] **PNDI-1Th** and **PNDI-0Th** had significantly lower electron mobilities of 3.1×10^{-3} cm^2/Vs and 6×10^{-4} cm^2/Vs respectively. The on/off ratios followed a similar trend. **PNDI-2Th** and **PNDI-3Th** displayed the largest on/off ratios (10^5) whereas **PNDI-0Th** yielded the lowest (10^3). The larger on/off ratios of **PNDI-2Th** and **PNDI-3Th** are mostly due to a larger on-current, where as the off-current value for all four polymers was within the same order of magnitude.

The threshold voltage (V_t) was calculated as the x-intersect of this linear fit line. Following a similar performance trend, **PNDI-3Th** had the lowest threshold voltage

while **PNDI-0Th** had the highest. The electrical characterization results are summarized in Table 3.2. From this data it is clear that within the series of four polymers presented within this report, increasing the thiophene content of PNDIs improves the electron transport properties of the polymer.

Table 3.2 Electrical characterization of PNDI-xTh copolymers

	μ_e (cm^2/Vs)	$I_{on/off}$	V_t (V)
PNDI-0Th	6×10^{-4} ($\pm 2 \times 10^{-4}$)	10^3	40
PNDI-1Th	3.1×10^{-3} ($\pm 3 \times 10^{-4}$)	10^3	20
PNDI-2Th	3.9×10^{-2} ($\pm 3 \times 10^{-3}$)	10^5	10
PNDI-3Th	7.6×10^{-2} ($\pm 4 \times 10^{-3}$)	10^5	7

3.2.3 X-ray diffraction and atomic force microscopy

X-ray diffraction (XRD) and Atomic Force Microscopy (AFM) were used to probe the relative crystallinity of the four polymers.

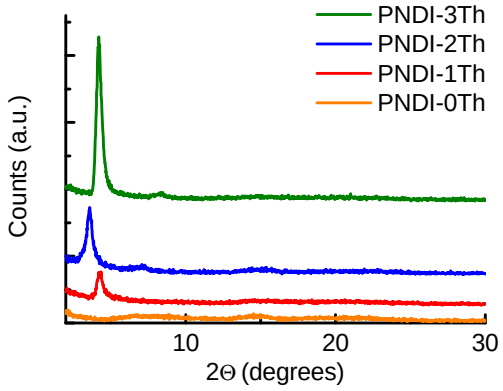

Figure 3.6 X-ray diffraction patterns of the PNDI-xTh polymers drop cast from $CHCl_3$ solution onto SiO_2 wafers

X-ray diffraction patterns were recorded of the four polymers and are presented in Figure 3.6. The spectra for **PNDI-1Th**, **PNDI-2Th**, and **PNDI-3Th** all show one peak at around 2θ = 3.5°. The peak intensity of **PNDI-3Th** was observed to be the largest series, followed by **PNDI-2Th** and finally **PNDI-1Th**. No diffraction peaks were observed in the **PNDI-0Th** spectrum indicating the material is largely amorphous with no observed long or short range order in the solid state. This is further supported by the lack of a significant shift between the solution and solid state UV-Vis spectra of **PNDI-0Th**. One aspect of particular interest is that **PNDI-2Th** has a peak at a slightly lower angle relative to the peaks present for **PNDI-3Th** and **PNDI-1Th**. A summary of the XRD peaks and the d-spacing is shown in Table 3.3 below.

Table 3.3 Angle 2θ and d-spacing of the XRD peaks observed in the PNDI-xTh polymers

Polymer	2θ	d(Å)
PNDI-0Th	-	-
PNDI-1Th	4.30°	20.5
PNDI-2Th	3.60°	24.5
PNDI-3Th	4.20°	21.0

The thin film morphology of all four polymers was examined with AFM. Thin films were prepared on Si/SiO_2 wafers using the same processing conditions as OFET fabrication, including OTS monolayers and annealing. This film preparation method enables a correlation between thin film morphology and measured charge carrier mobility. As observed in Figure 3.7 polymers **PNDI-0Th** and **PNDI-1Th** show no self-organization on the size scale observable in the AFM image. Polymer **PNDI-2Th** displays rod like features on the nanometer scale assembled into feather-like patterns.

The **PNDI-3Th** film shows rod or belt-like structures at a length scale smaller than the **PNDI-2Th** film also assembled in a roughly feathery pattern. This corroborates the XRD analysis to suggest that the **PNDI-2Th** polymers are more crystalline in the thin film phase compared to **PNDI-0Th** and **PNDI-1Th**.

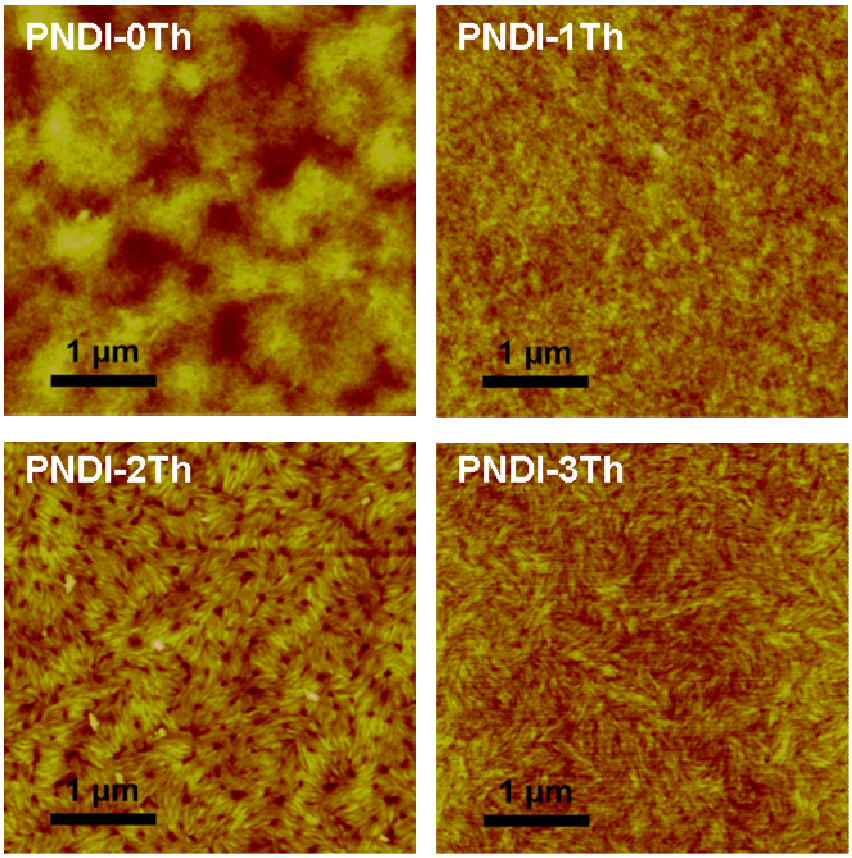

Figure 3.7 Tapping mode AFM height images of polymer thin films on OTS treated Si/SiO_2 wafers processed and annealed under the same conditions as OFETs.

3.2.4 Conclusion

We have demonstrated the synthesis and performance of a series of polymers will high electron mobilities. Electron mobilities as high as 0.076 cm^2/Vs were achieved in OFETs using **PNDI-3Th**. XRD results suggest increasing the thiophene content of **PNDI-xTh**

series effectively increases polymer crystallinity and order to a degree that leads to improved device performance. By employing alternative OFET device architectures such as top-gate bottom-contact and the use of various dielectrics and printing fabrication techniques, the measurable performance of **PNDI-3Th** should be able to exceed that of **PNDI-2Th** (0.85 cm^2/Vs) which was reported by Facchetti *et al.*[7] The high electron-mobility, energy levels, and good absorption spectrum of **PNDI-2Th** and **PNDI-3Th** suggest the possibility of yielding other moderately high-performance electronic devices with organic p-type semiconducting materials such as **P3HT**. Research into the performance of devices such as organic photovoltaic (OPV) devices and alternative OFET device architectures is the subject of future investigation.

4 Synthesis and characterization of solution-processable ladderized n-type naphthalene bisimide copolymers for OFET applications

4.1 Introduction

So called ladder polymers contain rigid π-conjugated backbones which produces structural planarity in the solid state. As a result, π- π stacking leads to molecular orbital overlap and π-electron delocalization. The ladder polymer poly(bensobisimidaxobenzophenanthroline (**BBL**) shown in Figure 4.1 has been shown to have an electron mobility as high as 0.1 cm^2/Vs.[16] However, it suffers from insolubility in common organic solvents due to its crystallinity and long-range order.

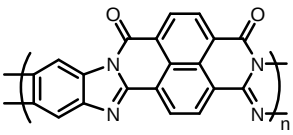

Figure 4.1 Chemical structure of BBL, a ladder polymer with high electron mobility, but poor solubility in common organic solvents

Despite the significant electrical performance of **BBL**, there have been few reports detailing other heteroaromatic ladder-polymers.[60] Previously, our group has synthesized a series of NDI-based thiophene copolymers with electron mobilites as high as 0.076 cm^2/Vs in transistors fabricated from **PNDI-3Th**.[61] With the aim of gaining insight into the structure-property relationships of high performing ladder materials and goal of synthesizing a fully soluble ladder-polymer, we devised a novel scheme involving

naphthalene diimide-based di-*tert*-butyldicarbonate substituted benzene polymers, here to fore referred to as **PNDI-0Boc**, **PNDI-1Boc**, and **PNDI-2Boc**.

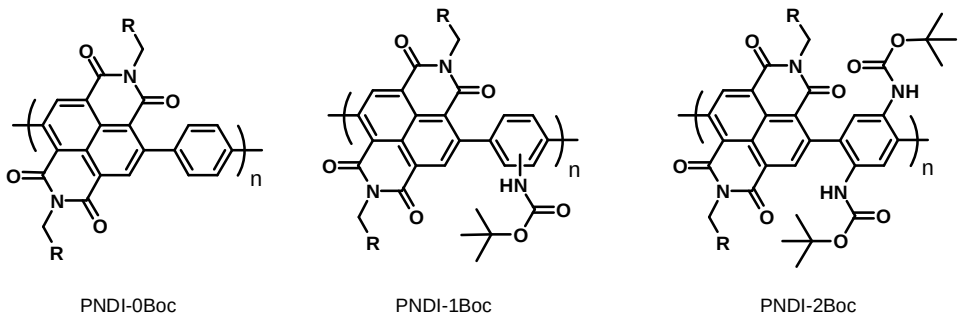

Figure 4.2 Chemical structure of polymers PNDI-0Boc, PNDI-1Boc, and PNDI-2Boc

As shown in Figure 4.2 above, this series contains a common NDI unit and a benzene moeity. **PNDI-0Boc** contains no Boc protecting groups on the benzene ring, while **PNDI-1Boc** and **PNDI-2Boc** contain one and two Boc protecting groups, respectively. Initially we sought to produce semiconducting ladder polymer films by making precursor films from these materials, then cyclizing them in the solid state at high temperature (300 °C); however, these films exhibited poor electrical performance, and little evidence of crystallinity. It was believed that the restricted conformational freedom in the solid state somehow affected the cyclization process, so the polymers were instead cyclized in solution before characterization. The octododecyl solubilizing chains attached to the NDI unit proved capable of solubilizing the final ladder polymers in common organic solvents. To the best of our knowledge, this is the first report of a n-type ladder polymer soluble in common organic solvents.[62]

4.2 Results and discussion

4.2.1 Thermal analysis

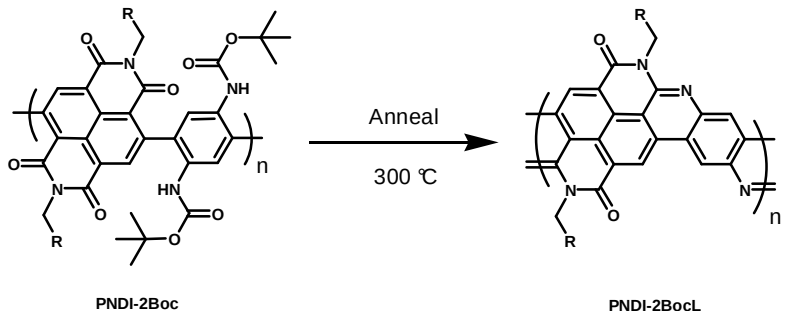

Figure 4.3 Chemical structure of soluble Boc-protected precursor polymer PNDI-2Boc and the cyclized ladder polymer PNDI-2BocL produced after thermal treatment at 300 °C

Thermogravimetric analysis (TGA) was used to determine the specific mass loss of the polymer after annealing in the solid state. In order to completely cyclize, the Boc protecting group needs to be removed, followed by removal of a water molecule. For **PNDI-2Boc**, this theoretically corresponds to a 16% mass loss (Boc group) and an additional 2% mass loss (water), if all of the Boc protecting groups are removed and complete cyclization occurs.

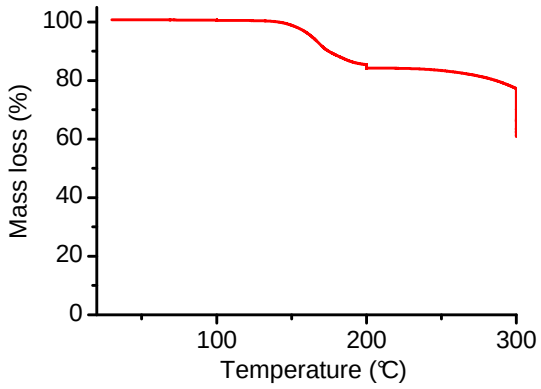

Figure 4.4 TGA of polymer PNDI-2Boc using ramped heating 20 °C - 300 °C

During the TGA run, the polymer film was heated from 20 °C to 300 °C with holds at 100 °C, 200 °C, and 300 °C for one hour each. As shown in Figure 4.4, between 150 °C and 250 °C the polymer loses 16% of its mass. This can be attributed to the cleaving of the Boc-protecting group. There is another small mass loss (approximately 3%) between 250 °C and 300 °C, possibly due to the cyclization process, which produces a water molecule. Above 300 °C the polymer rapidly begins to decompose.

OFET devices showed that thin films cast from **PNDI-2Boc** become insulating when heated above 150 °C. Because of this finding, further study was initiated using a solution-phase ladderization method, as it was found that the octadodecyl solubilizing chains on the NDI moiety were capable of bestowing solubility on the final ladder polymers in common organic solvents.

The solution-phase ladderization procedure was adapted from a previously published method[63] to form soluble ladder polymers in solution. The scheme is shown in Figure 4.5 below.

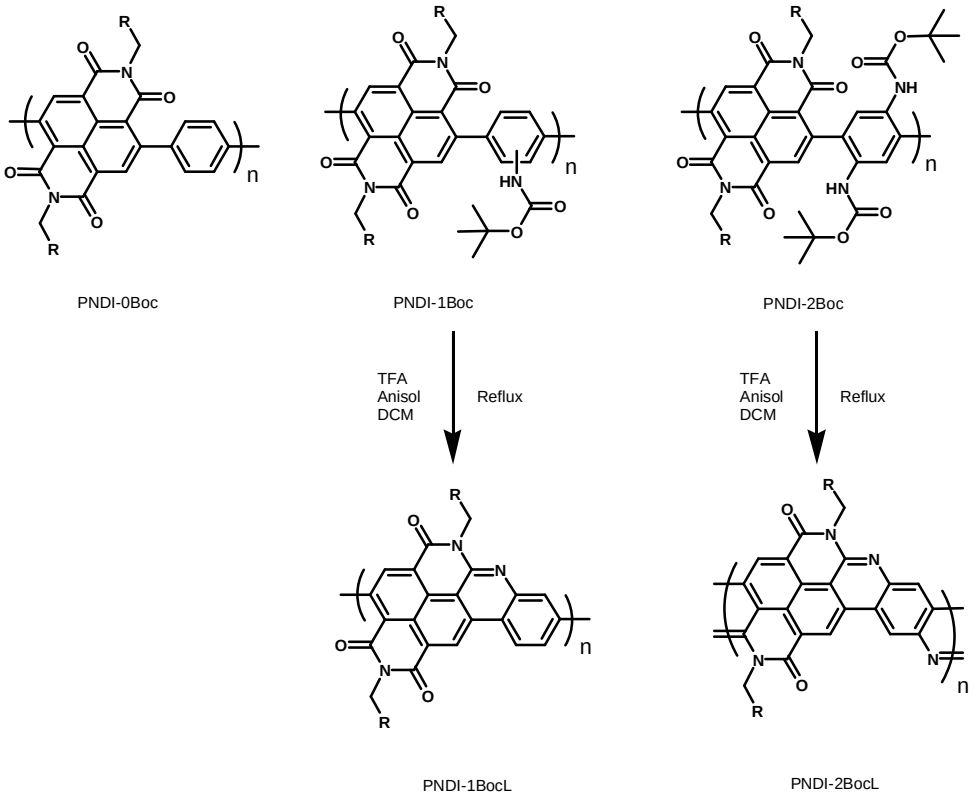

Figure 4.5 Solution ladderization method to form polymers PNDI-1BocL and PNDI-2BocL

The precursors **PNDI-1Boc** and **PNDI-2Boc** were dissolved in dichloromethane, and treated with trifluoroacetic acid and anisole, then heated at reflux overnight to cleave the Boc groups and form intramolecular imine bridges to produce the final ladder structures, **PNDI-1BocL** and **PNDI-2BocL**, respectively. The molecular weights of the polymers were determined with size-exclusion chromatography in THF relative to polystyrene standards. The results are shown in Table 4.1 below.

Table 4.1 Number average molecular weights and polydispersity index (PDI) for the PNDI-xBoc series of polymers

	M_n (kDa)	PDI
PNDI-0Boc	8.8	2.5
PNDI-1Boc	4.0	1.8
PNDI-2Boc	7.2	1.6
PNDI-1BocL	4.3	1.9
PNDI-2BocL	14	1.8

The measured molecular weights of the polymers are recognized to be overestimates of the actual molecular weights because of the rigid-rod-like structure of the NDI moeity and the additional planar structure induced by ladderization. The hydrodynamic radius, and therefore the measured molecular weight is increased by planarization. The measured molecular weights of the ladderized polymers are both larger than the Boc-protected precursors. The material with the greatest amount of ladderization, **PNDI-2BocL**, shows the largest increase from 7.2 kDa to 14 kDa.

4.2.2 Optical and electrochemical characterization

Optical absorption spectra of the five polymers in solution and thin film states are shown in Figure 4.6 below.

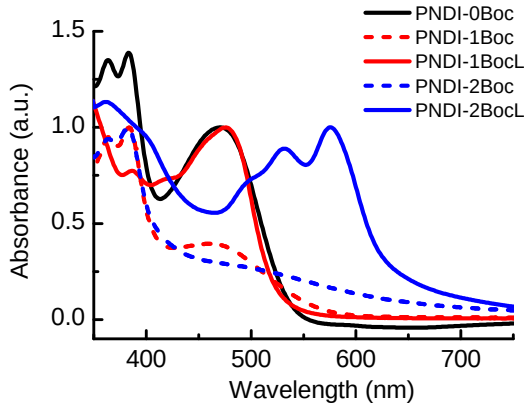

Figure 4.6 UV-Vis absorption spectra of spin-cast thin films of polymers PNDI-0Boc, PNDI-1Boc, and PNDI-2Boc .

As observed in the spectra, a pronounced red shift occurs due to the ladderization of both **PNDI-1Boc** and **PNDI-2Boc** to **PNDI-1BocL** and **PNDI-2BocL**, respectively. The absorption maximum of **PNDI-1Boc** increases from λ_{max} = 384 nm to λ_{max} = 476 nm after cyclization. There is an even greater shift in absorption maximum after the ladderization of **PNDI-2Boc**, from λ_{max} = 283 nm to λ_{max} = 576 nm. The difference in optical band gap between **PNDI-2BocL** (E_g = 1.96 eV) and **PNDI-1BocL** (E_g = 2.37 eV) is a result of an increase in the number of rotational degrees of freedom along the backbone of **PNDI-1BocL**, which allows breaks in the π-conjugation between individual sub-ladderized units. **PNDI-2BocL**, however, has a continuous ladderized structure along the entire rigid π-conjugated backbone. While **PNDI-2Boc** and **PNDI-2BocL** have similar band gaps, significant red shift in the feature at 531 nm is further evidence of extended conjugation in **PNDI-2BocL**. The non-ladderized polymer **PNDI-0Boc** has comparatively better absorption characteristics than the other non-ladderized polymers, **PNDI-1Boc** and **PNDI-2Boc**, due to its lack of Boc protecting groups. **PNDI-1Boc** and **PNDI-2Boc**

show similar absorption maxima due to the bulky Boc protection groups which inhibit absorption to a similar degree.

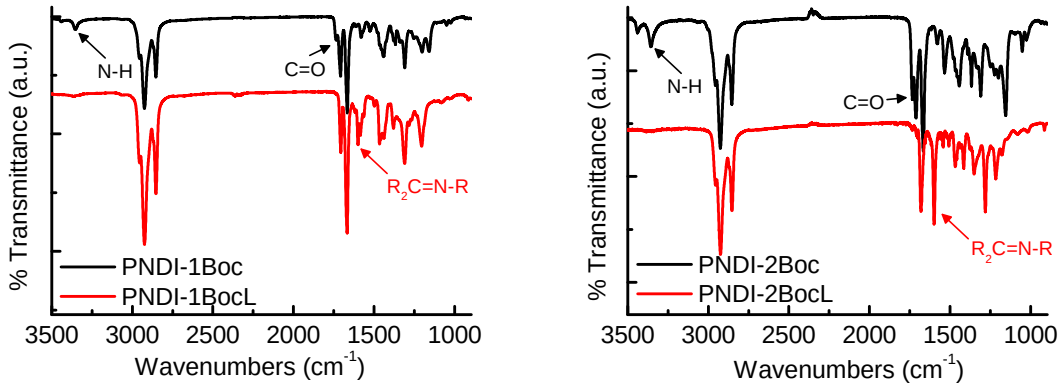

Figure 4.7 FTIR Spectra of PNDI-1Boc (A) and PNDI-2Boc (B) before and after solution ladderization

Further evidence of ladderization formed through imine-bridge formation is shown in the FTIR spectrum in Figure 4.7 above. As observed in the spectra, the peaks at 3360 cm^{-1} and 3450 cm^{-1}, which correspond to the N-H stretch in the imine functionality of **PNDI-1Boc** and **PNDI-2Boc**, are lost in the spectra of the ladderized polymers **PNDI-1BocL** and **PNDI-2BocL**. In addition, the peak at 1740 cm^{-1} (1715 cm^{-1} and 1735 cm^{-1} in the case of **PNDI-2Boc**), corresponding to the C=O stretch on the NDI moiety of the uncyclized polymers, is lost after ladderization. There is also a significant gain in the intensity of the peak at 1600 cm^{-1}, corresponding to a single imine stretch in **PNDI-2BocL**, and the appearance of several peaks in the same location of the **PNDI-1BocL** spectra, believed to be due to the existence of several isomeric structures. The low intensity of the –C=O stretch group in **PNDI-1Boc** compared to **PNDI-2Boc** is most likely due to a smaller number of Boc functional groups in than in **PNDI-1Boc**.

Cyclic voltammetry measurements were performed in a standard three-electrode cell using a platinum working electrode coated with drop-cast films of the polymers, a platinum counter electrode, and a $Ag/AgNO_3$ reference electrode. Spectra were referenced to an internal standard (ferrocene/ferrocenium, 4.8 eV) to determine the LUMO levels of the five polymers. As shown in the previous chapter, the LUMO levels of the three uncyclized polymers, **PNDI-0Boc**, **PNDI-1Boc**, and **PNDI-2Boc**, were all approximately 3.8 eV, as they all possess unmodified NDI units. Ladderization was found to increase the LUMO level of both **PNDI-2BocL** and **PNDI-2BocL** to 3.54 eV as a result of a reduction in the electron-deficiency by the ladderization process, which forms an imine bridge, which is more electron-withdrawing, in place of the carbonyl group. The compiled UV-Vis and CV data are shown in Table 4.2 below.

Table 4.2 UV-Vis absorption and cyclic voltammetry data for the PNDI-xBoc(L) polymers

	soln λ_{max} abs (nm)	film λ_{max} abs (nm)	E_g^{opt} (eV)	$E_{1/2red}$ (V)	LUMO (eV)	HOMO (eV)
PNDI-0Boc	453	471	2.31	–0.96	–3.79	–6.10
PNDI-1Boc	380	384	2.19	–0.90	–3.83	–6.02
PNDI-2Boc	381	382	1.94	–0.84	–3.90	–5.84
PNDI-1BocL	467	476	2.37	–1.20	–3.54	–5.90
PNDI-2BocL	578	576	1.96	–1.18	–3.54	–5.49

4.2.3 Electrical and structural characterization

OFET devices using the five polymers were fabricated using a typical top-contact, bottom-gate geometry on p-doped Si/SiO_2 wafers. The active layers of all devices were

spin-cast from 5 mg/mL solutions of polymer in chlorobenzene. All fabrication and testing was performed in an inert atmosphere. Figure 4.8 below shows the transfer characteristics of **PNDI-0Boc**, **PNDI-1Boc**, and **PNDI-1BocL** at positive gate-source biases.

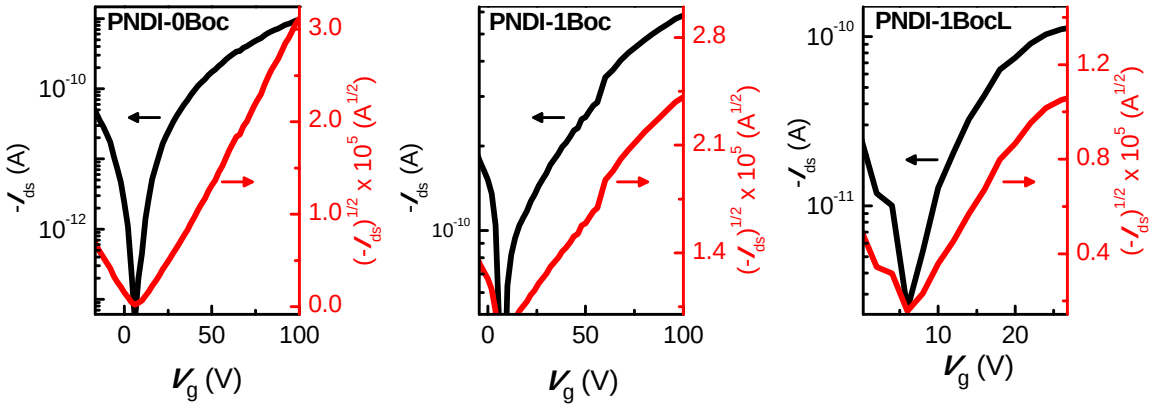

Figure 4.8 Transfer curve of polymers PNDI-0Boc, PNDI-1Boc, and PNDI-1BocL at a constant V_{ds} = 100 V

Each of these polymers shows n-type behavior at positive gate-source biases (V_g = +100 V). The polymers did not display ambipolar or p-type response; rather, they exhibited low current flow and on/off ratios below 10 when a negative gate-source bias was applied (V_g = −100 V). A linear fit was applied in the saturation region of the $I_{ds}^{1/2}$ vs V_g curve to calculate the saturated charge carrier mobility of each material according to the saturation current equation: $I_{ds} = (\mu WC_i/2L)(V_g - V_t)^2$.

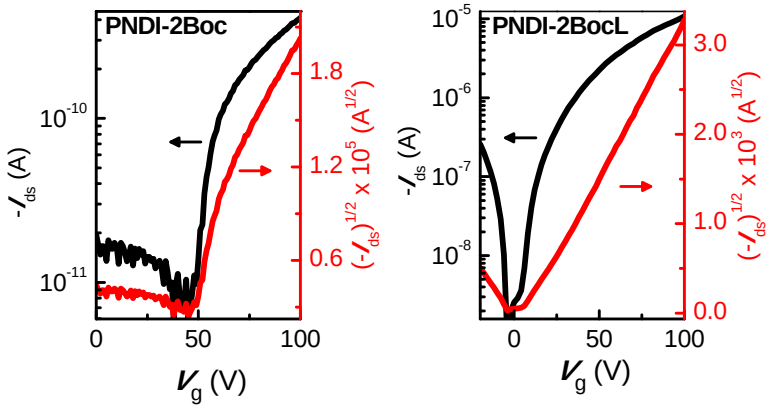

Figure 4.9 Transfer curve of PNDI-2Boc and PNDI-2BocL at a constant V_{ds} = +100 V and the square root of drain current as a function of gate voltage

An electron mobility (μ_e) as high as 2.6 × 10^{-3} cm^2/V s was measured from OFETs using **PNDI-2BocL** (Figure 4.9). As shown in Table 4.3, **PNDI-2BocL** was found to possess the highest charge carrier mobility of the series—an increase of over 3 orders of magnitude compared to the nonladderized **PNDI-2Boc** (1.9 × 10^{-6} cm^2/Vs). Very little change in electron mobility was observed between **PNDI-1Boc** and its ladderized constituent **PNDI-1BocL**. **PNDI-0Boc** also performed similarly compared to the polymers **PNDI-1Boc** and **PNDI-1BocL**. As can be seen in Figure 4.8 and Figure 4.9, although the on/off ratio of **PNDI-0Boc** was the same as the on/off ratio for **PNDI-2BocL**, both the I_{on} and I_{off} for **PNDI-0Boc** was greatly reduced compared to **PNDI-2BocL**. Complete ladderization in the case of **PNDI-2BocL** led to an increase in electron mobility, whereas the locally ladderized-subunit structure of **PNDI-1BocL** showed negligible performance gains following imine-bridge formation.

Table 4.3 Electrical properties of NDI copolymers as measured in OFET devices

	μ_e (cm^2/Vs)	$I_{on/off}$	V_t (V)
PNDI-0Boc	6×10^{-6} ($\pm 1 \times 10^{-6}$)	10^4	9
PNDI-1Boc	4×10^{-6} ($\pm 1 \times 10^{-6}$)	10^2	10
PNDI-2Boc	1.9×10^{-6} ($\pm 4 \times 10^{-7}$)	10^2	50
PNDI-1BocL	4×10^{-7} ($\pm 1 \times 10^{-7}$)	10^2	7
PNDI-2BocL	2.6×10^{-3} ($\pm 4 \times 10^{-4}$)	10^4	5

Furthermore, the 5 polymers were analyzed by X-ray diffraction (XRD). However, the XRD characterization performed on the polymer series yielded no distinct peaks- indicating that the 5 NDI polymers have very little, if any, long-range ordering in the solid state. This is further supported by the lack of a significant shift between the solution and solid state UV-Vis absorption spectra of the polymer series. Varying OFET device annealing temperatures between 80 and 200 °C had little effect on the electron charge mobility which may also coincide with the lack of a phase transition in this temperature range. In addition, surface morphology of the polymer films as observed by AFM showed no distinct features, which led us to believe the morphology in the thin films was amorphous in nature. While this insight may lead one to believe that the ladder polymers were amorphously crosslinked- solid-state ladderization experiments were performed on polymer thin-films of **PNDI-2Boc** by heating and annealing the polymers to 250 °C. The characterized **PNDI-2BocL** films made by this process showed the same indicative FTIR and UV–Vis spectra coinciding with imine-bridge formation. However,

the solid-state generated ladder polymer films were completely insoluble amid exposure to all common organic solvents, exhibited entirely amorphous structures, and performed poorly in OFET devices as a result of the formed crosslinked polymer structures.

4.2.4 Conclusions

A series of high-performance NDI-based substituted phenylene copolymers capable of forming ladderized imine-bridges upon treatment with TFA have been presented. Imine bridge formation was confirmed by FTIR, UV–Vis, and CV. A solution-based ladderization route was found to be superior compared to a solid state ladderization from a solution-processed precursor. Average electron mobilities as high as 0.0026 cm^2/Vs were measured in OFETs made from **PNDI-2BocL**. The charge-carrier mobility of the **PNDI-2BocL** showed a three order of magnitude improvement over the non-cyclized **PNDI-2Boc** polymer. XRD and AFM results show the materials to be primarily amorphous in the thin film state. The relatively high electron-mobility, suitable energy levels, and good absorption spectrum of **PNDI-2BocL** suggest the polymer's potential for use as the n-type component in various device applications.

5 Charge transfer in all-polymer bulk heterojunction blends for organic solar cells

5.1 Literature review and introduction

Solution processed organic photovoltaics (OPVs) have the potential to produce low cost electricity. Polymer and small molecule organic materials have the advantage of simple processing techniques such roll-to-roll coating and ink-jet printing, compared to their inorganic counterparts. Currently, power conversion efficiencies (PCEs) of organic photovoltaics have risen to over 10%.[64] The most efficient cells to date contain a blend of a p-type π-conjugated polymer donor and a small molecule fullerene-based acceptor.[65-69] Although these cells have reached relatively high efficiency, their photocurrent generation is hampered by the acceptor material only having weak absorbance in the visible range.[70] While some methano-fullerene derivatives, such as $PC_{71}BM$, have enhanced absorption extending into the blue region of the spectrum,[71-73] this increased absorption does not extend into the red and near-IR regions where donating polymers transmit light. In addition, the large LUMO energy offsets between donor polymers and fullerene based acceptors reduces the available open-circuit voltage and therefore limits the photovoltaic efficiency. Fullerene acceptors also suffer from grain coarsening during long annealing times,[74] which typically benefit the donor polymer through increased hole mobility.

All-polymer solar cells offer a number of advantages over fullerene-based acceptors. In a polymer/polymer blend, both the donor and acceptor can act as light harvesting materials. As acceptors, n-type polymers hold promise due to the ability to

absorb light in a tunable absorption spectrum complementary to the donor absorption spectrum because polymer synthesis affords synthetic flexibility in bandgap and energy level tuning. N-type polymers have also been shown to exhibit charge carrier mobilities as high as 0.076 cm^2/Vs in OFETs.[61] In addition, n-type polymer blends offer the variety and possible control of chemical, electronic, and mircostructure properties. However, power conversion efficiencies have been less than 2% due to a number of issues, including phase segregation and charge transfer.[75-81]

Although efficiencies of almost 2% have been reported for all polymer solar cells, they have lagged behind bulk herterojunction cells using small molecule n-type acceptors. Previous work with all-polymer systems have suffered from low short circuit current densities and low fill factor (FF). In addition, the use of n-type polymers results in unbalanced electron and hole transport, which has been shown to lead to space charge effects.[82] As early as two decades ago, laminated all-polymer OPV devices reported efficiencies as high as 1.9% using a poly(2-methoxy-5-(2-ethyl-hexyloxy)-1,4-phenylene-vinylene) (**MEH-PPV**) derivative as a donor materials and a regioregular phenyl-octyl substituted polythiophene (**POPT**) as an acceptor.[83] Further work was accomplished with **PPV** derivatives and polyfluorene copolymers acceptors such as poly(9,9′-dioctylfluorene-co-benzothiadiazole) (**F8BT**) and poly(9,9‘-dioctylfluorene-co-bis(N,N‘-(4,butylphenyl))bis(N,N‘-phenyl-1,4-phenylene)diamine) (**PFB**) showing power conversion efficiencies up to 1.8%.[84-86] More recently, benzothiadiazole based acceptors[87] and polyfluorene based acceptors[80] have been blended with **P3HT** to create OPV devices, but these n-type polymers resulted in low performing devices.

The electron mobility of the **PNDI-xTh** series of polymers, as well as their optical absorption profile make them promising candidates for all-polymer OPVs. In addition the LUMO levels of these n-type materials match well to the LUMO level of **P3HT** in order to both induce exciton disassociation and produce a large open circuit voltage.

Herein, we study the photo-induced charge transfer of all-polymer solar cells consisting of **P3HT** and a series of n-type polymers polynaphthalene diimide-thiophene copolymers. In addition, we show the optical and electrical properties of these blends. We explain why **PNDI-1Th** and **PNDI-2Th** are the best candidates as acceptors in all-polymer OPV, and preview improvements for the next generation of polymer acceptors in OPVs.

5.2 Results and discussion

5.2.1 Structure and energy band alignment

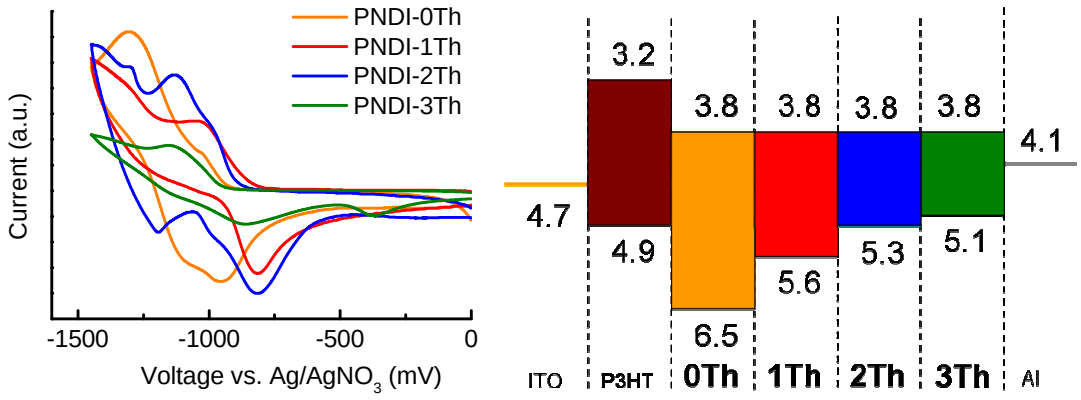

Figure 5.1 Cyclic voltammetry and HOMO and LUMO levels of the four PNDI-xTh polymers compared to P3HT

Figure 5.1 shows cyclic voltammograms of **PNDI-0Th**, **PNDI-1Th**, **PNDI-2Th** and **PNDI-3Th** n-type copolymers in addition to their HOMO and LUMO levels compared to **P3HT**. As shown in Figure 5.1, there is a 1.5 eV potential difference between the HOMO of **P3HT** (4.9 eV) and the LUMO of the all four polymers (3.8 eV). Accounting for the empirically observed voltage drop in these systems of 0.3 eV, a V_{OC} of 0.8 V is theoretically attainable.[88] The empirical relationship between LUMO offsets and maximum attainable V_{oc} is shown in equation 5.2.1 below.[89]

$$V_{oc} = \left(\left| HOMO_{donor} \right| - \left| LUMO_{acceptor} \right| \right) - 0.3V \qquad \text{Equation 5.2.1}$$

5.2.2 Optical absorbance spectroscopy

The UV-Vis absorbance spectrum of **PNDI-xTh:P3HT** blended films (normalized to the λ_{max} of P3HT) is shown in Figure 5.2. The absorption spectrum of the blends is merely a superposition of the individual spectrum (see section 3.2.1), indicating no charge transfer in the ground state. Note the absorbance for **PNDI-2Th** and **PNDI-3Th** nicely complements the **P3HT** absorbance (550 nm) allowing light absorption of the blends up to 800 nm. **PNDI-1Th** and **PNDI-2Th** also show an absorption peak below 400 nm (π-π* band).[90] The resulting spectrum of the **PNDI-2Th** blend thus covers a significant portion of the visible spectrum. In addition, it has been shown that **PCBM** can disrupt the regular packing of **P3HT**; results are seen as a loss of the **P3HT** vibronic structure (500 nm to 650 nm) in the thin film absorbance.[91-93] In the case of all four of these n-type accepting polymers, the blend films display that fine vibronic structure remains intact.

This indicates that the acceptor polymers do not prevent regular packing in **P3HT**, which could lead to improved hole mobilities in the blend films.

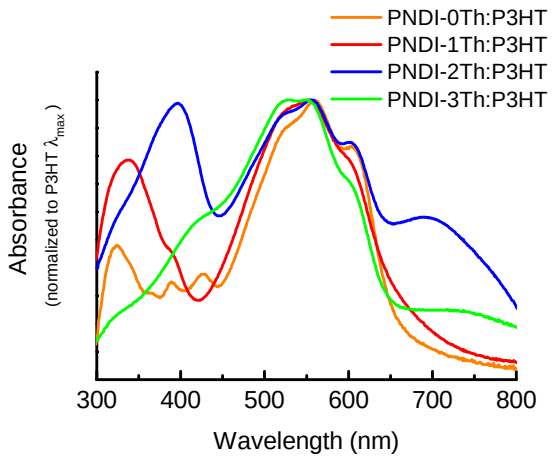

Figure 5.2 UV-Vis absorption of PNDI-xTh:P3HT blend thin films. Absorbance is normalized to the λ_{max} of P3HT.

5.2.3 Photoluminescence

To determine if the **PNDI-xTh** polymers function as suitable acceptors in all-polymer OPVs, we first show how **P3HT** photoluminescence intensity is modified by incorporation of **PNDI-xTh** into blended films. Figure 5.3 shows the intensity of the integrated polymer photoluminescence (PL) of **P3HT** films loaded with different acceptors. The polymers were blended in a 1:1 weight ratio and spin cast from chlorobenzene onto ITO substrates to produce ~100 nm thick films, then annealed for 8 minutes at 110 °C on a hotplate, similar to the OPV devices used in this section.

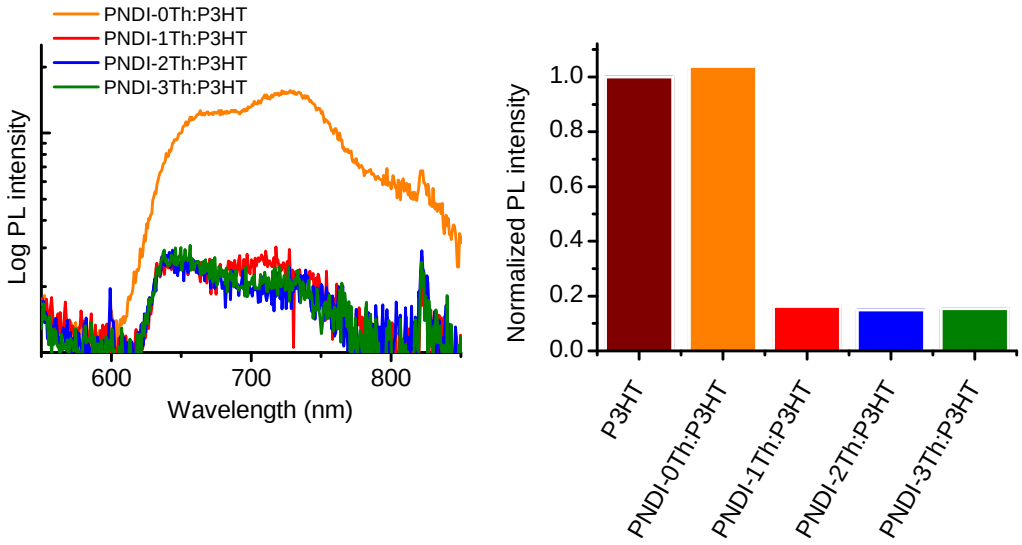

Figure 5.3 Photoluminescence (PL) spectrum of PNDI-xTH/P3HT blend films (left) and integrated PL intensity of PNDI-xTH/P3HT blend films compared to neat P3HT (right)

Polymers **PNDI-1Th**, **PNDI-2Th** and **PNDI-3Th** all serve to quench the integrated **P3HT** PL down to below 20% of its intensity in neat films. The incorporation of the homopolymer **PNDI-0Th** into **P3HT** films serves to increase the PL intensity due to the contribution of PL from **PNDI-0Th** that is present in **PNDI-0Th** pristine films. Figure 5.4 shows the time resolved PL decay for blended films and neat **P3HT** excited at 470 nm and measured using time-correlated single photon counting. The decays for **PNDI-1Th** and **PNDI-2Th** blend films show a marked decrease in lifetime compared to the neat **P3HT** film. This is consistent with the PL quenching exhibited in Figure 5.3 and demonstrates that the addition of **PNDI-1Th** and **PNDI-2Th** provides an alternative pathway to **P3HT** excitation other than PL. Similar to Figure 5.3, **PNDI-0Th** blend films show an increase in PL lifetime compared to neat **P3HT**. As before, this is likely due to the PL introduced by the **PNDI-0Th** polymer.

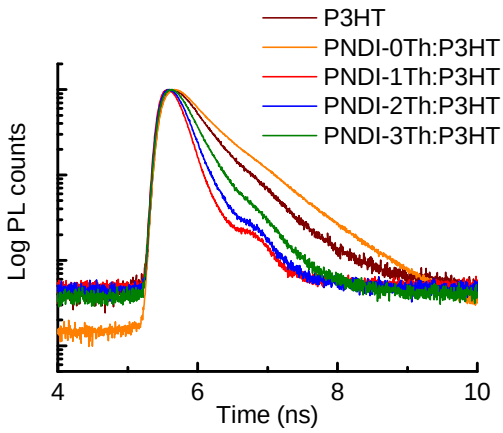

Figure 5.4 PL lifetime histograms of neat P3HT and P3HT blended with the PNDI-xTh polymers

5.2.4 Photo-induced absorption spectroscopy (PIA)

Though the **PNDI-1Th** and **PNDI-2Th** blend films clearly demonstrate a disruption of the normal radiative decay of **P3HT** photoexcitation, PL quenching experiments alone can not differentiate between photo-induced charge transfer (necessary for OPV operations) and other non-radiative decay routes such as energy transfer.

Quasi-steady-state photo-induced absorption spectroscopy (PIA) monitors the differential transmission due to long-lived photoexcitations such as triplet excitons or polarons. If charge transfer proceeds after **P3HT** photoexcitation, a positive charge is created on **P3HT** (positive polaron) and a negative charge is created on the acceptor polymer (negative polaron). The polaron charge and the associated conformational relaxation exhibit characteristic sub optical band gap energy absorption in conjugated polymers. Photo-induced charge transfer, as in PL quenching, can be followed by fast

recombination, but PIA signals indicate carriers with lifetimes long enough to be transported and extracted in photovoltaic cells.

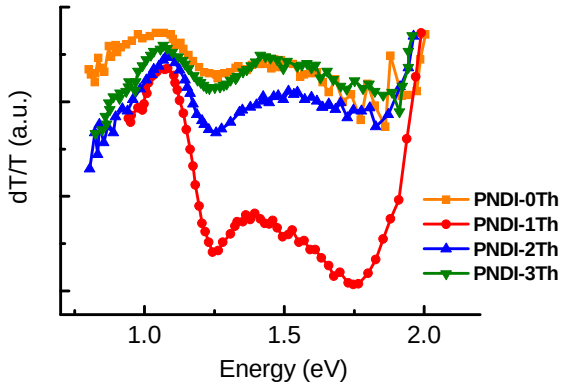

Figure 5.5 Photo-induced absorption spectra of P3HT:PNDI-xTh thin film blends.

Figure 5.5. shows the X-channel (in-phase) PIA signal for four different polymer blends containing **PNDI-0Th**, **PNDI-1Th**, **PNDI-2Th**, **PNDI-3Th** as acceptors. Detailed experimental procedures can be found in the experimental section. As seen in the spectra, there is a broad absorption peak between 1.2 eV and 1.8 eV for **PNDI-1Th** and **PNDI-2Th** blends. The **PNDI-0Th** and **PNDI-3Th** blend exhibits comparatively less absorption. The **PNDI-0Th** spectrum shows little if any evidence of long lived charges (polarons) present in the film. This is consistent with the PL quenching and lifetime measurements. As such, the following sections will not address **PNDI-0Th** as these three characterization methods (PL quenching, PL lifetime, PIA) have identified **PNDI-0Th** as a poor acceptor for **P3HT**-based OPVs. All four polymer blend films show a distinct peak at about 1.25 eV which corresponds to the positive polar feature on **P3HT** identified in the literature.[94] The peak at about 1.75 eV for **PNDI-1Th** and about 1.63 eV for

PNDI-2Th are unique to this acceptor system. As reference, **P3HT**:PCBM films show a PIA feature at 1.85 eV ascribed to **PCBM**.[95]

In order to investigate the origin of these newly observed PIA signals, spectro electrochemistry was employed. Spectral electrochemistry was performed on neat thin films of **PNDI-1Th** and **PNDI-2Th** drop cast on FTO-glass substrates. Detailed experimental procedures can be found in the experimental section.

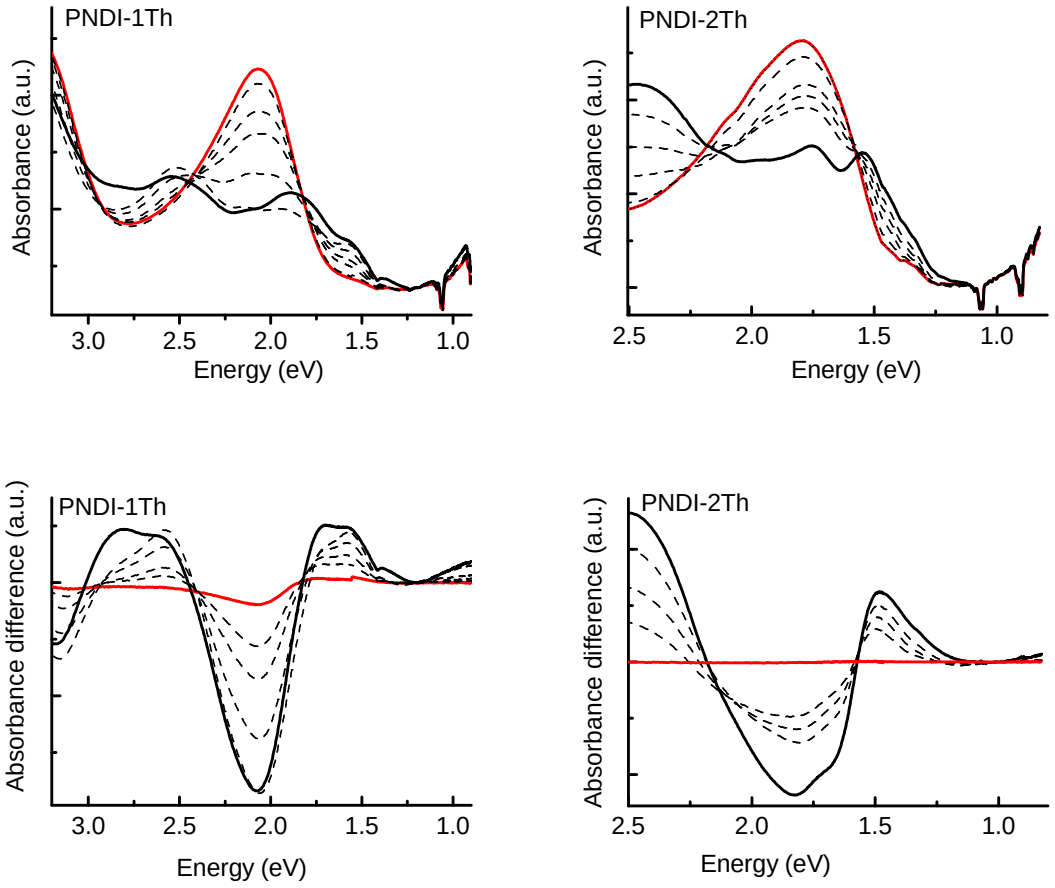

Figure 5.6 Electrochemical absorption spectra of PNDI-1Th (left) and PNDI-2Th (right). Top panels show absorbance at varying potentials. Bottom panels show difference spectra compared to the ground state.

Figure 5.6 shows the absorbance spectra of **PNDI-1Th** and **PNDI-2Th** from +0.75 V (red line) to -1.5 V (solid black line) against a silver reference. At a potential of +0.75 V, corresponding to a mild oxidizing condition, the spectra correspond to the ground state thin film absorption of the two polymers. In the case of **PNDI-1Th**, as the potential is scanned down to -1.5 V (corresponding to reducing conditions), a peak emerges at approximately 1.75 eV. This can be clearly seen in the difference spectrum and corresponds to a negative charge loaded on **PNDI-1Th**. Coupled with the PIA data, we therefore identify 1.75 eV as the **PNDI-1Th** negative polaron. The reduction cycle involving negative polaron formation was stable over many runs, consistent with the stable n-type behavior of the **PNDI-1Th** polymer. Absorption of **PNDI-2Th** vs. varying potential is shown in Figure 5.6 (right panels). As the potential is scanned from +0.75 V to -1.5 V, a broad absorption feature develops around 1.6 eV. As seen in the difference spectrum (lines help guild the eye), peaks in the reduced polymer are displayed at 1.56 eV and 1.71 eV. At a reducing potential, the absorption spectrum corresponds to a negative charge on **PNDI-2Th**. Therefore, we ascribe this spectral feature to the **PNDI-2Th** negative polaron. To the best of our knowledge, these are the first reports of negative polaron features confirmed in PNDI-based copolymers. The polaron energies are in good agreement with the PIA data, as well as the thin film band gaps.

5.2.5 Photovoltaic device characterization

In order to asses charge transport in the **PNDI-xTh:P3HT** blends, space charge limited current (SCLC) devices were fabricated (see experimental section for fabrication details). The SCLC device architecture and J-V characteristics of the two polymer blends are shown in Figure 5.7.

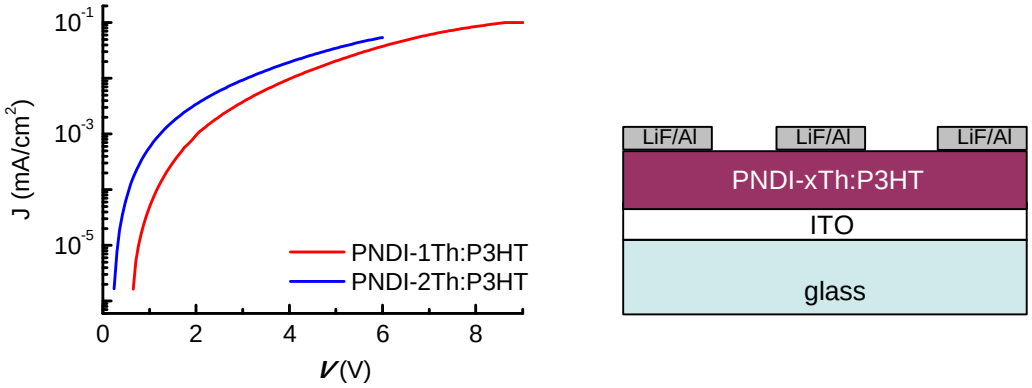

Figure 5.7 SCLC J-V characteristics and SCLC device architecture of PNDI-xTh blend thin films

The SCLC electron mobility of each of the two polymers when blended with P3HT was determined by fitting the J-V curve to the standard SCLC equation 5.2.5 shown below.[96]

$$J = \frac{9}{8}\varepsilon_0\varepsilon_p\mu\frac{V^2}{L^3} \qquad \text{Equation 5.2.5}$$

By fitting the data in the space-charge limited regime, the SCLC electron mobility of **PNDI-1Th** and **PNDI-2Th** was found to be 5 × 10^{-4} cm^2/Vs and 4 × 10^{-4} cm^2/Vs respectively. These values are smaller than the OFET mobility of these materials shown in previous sections, but consistent with the fact that the materials are in blended films, and the electric field driving current flow is much lower in the SCLC architecture than in OFET architecture. The SCLC mobilities of the these acceptor polymers also compares favorably to the SCLC hole mobility of **P3HT** reported in the literature.[97] It also confirms the previously published finding that **PNDI-2Th** and **P3HT** have comparable

mobility in blend-film based ambipolar OFETs.[98] As such, we have identified a system with balanced electron and hole transport, a necessary requirement for high performance in OPVs. This also shows that electron transport in the PNDI-xTh polymers will not be limiting factor in all-polymer OPVs containing these polymers.

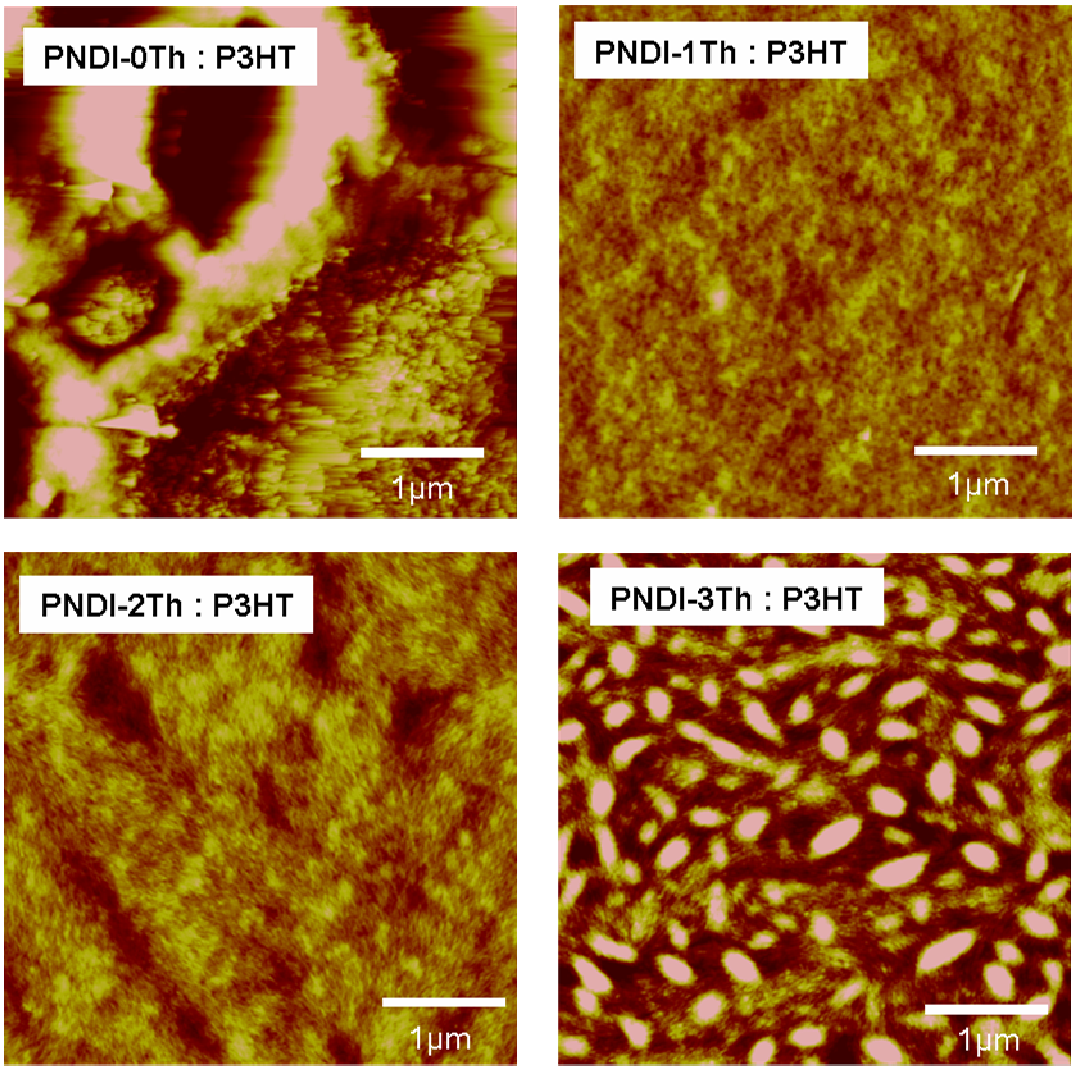

Figure 5.8 AFM surface topography of PNDI-xTh:P3HT thin films as used in OPV devices

To investigate the role of blend morphology on device performance, the surface morphology of the thin films of the OPV devices (imaged away from the deposited metal

cathode) was recorded using atomic force microscopy (AFM). As shown in Figure 5.8, the **PNDI-0Th** films show large scale phase segregation with domains larger than 1 μm, and surface features taller than the z-limit of the AFM. This poor morphology is consistent with the spectroscopic results and further indicates that the other n-type polymers are better candidates for photovoltaic devices. **The PNDI-1Th** and **PNDI-2Th** films display a fiber-like structure that is similar to the surface morphology observed in the neat films of these two polymers shown in Section 3.2.3. The surface roughness of both **PNDI-1Th:P3HT** and **PNDI-2Th:P3HT** were both below 2 nm, an indication of good conformal contact with the vacuum deposited metal electrode. The **PNDI-3Th** film displays large grain-like structures on the order of hundreds of nanometers to microns in length. Regardless of annealing conditions or solution concentrations, these features are present. This phase segregation could be the cause of **PNDI-3Th** based solar cells poor performance (negligible photocurrent generation) due to a lack of interfacial area necessary for exciton dissociation. It may also explain the lower PIA signal of the **PNDI-3Th** blends compared to the other n-type copolymers.

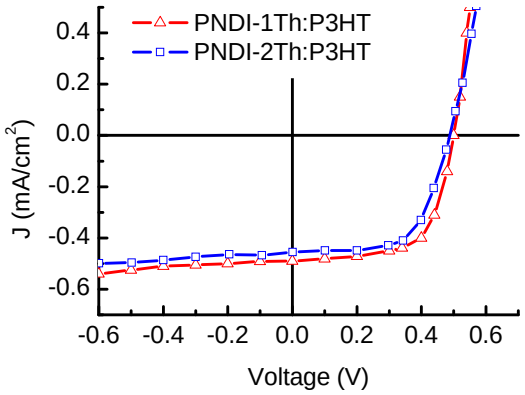

Figure 5.9 J-V characteristics of OPV devices fabricated with PNDI-1Th and PNDI-2Th as acceptors and P3HT as donor

OPV devices were fabricated in the standard architecture, using glass/ITO/PEDOT/polymer blend/LiFAl layers. Detailed device fabrication procedures can be found in the experimental section. Devices were optimized in terms of blend ratio, thickness, and annealing temperature. A 1:2 w/w ratio of **PNDI-xTh:P3HT** produced the highest photocurrent density; spin cast from either CB or *o*DCB (both solvents yielded approximately the same performance). The maximum PCE for the **PNDI-2Th:P3HT** was 0.17 % and **PNDI-1Th:P3HT** was 0.21%. The open circuit voltages using each acceptor was approximately the same, at about 0.50 V, lower than the idealized value of donor HOMO-acceptor LUMO. This may be due to the low short current density of both materials. The devices made from both **PNDI-1Th** and **PNDI-2Th** exhibit exceptional fill factor of 0.68 and 0.65 respectively. This may be due to the very nearly ideal diode behavior and the nearly pure n-type character of the **PNDI-xTh** polymers as shown in OFET devices. The high fill factor, as compared to conventional **P3HT**:**PCBM** devices, may also be related to the polymer:LiF/Al interface which has been shown in XPS studies to contain very high concentrations of the n-type polymer,[90] and an AFM surface

morphology which looks remarkably similar to the surface morphology of the neat acceptors (see previous section). A greater concentration of the acceptor at the cathode interface would potentially enhance charge extraction and therefore influence fill factor. These results are in line with the previous reports using the same materials.[77, 90] The results are tabulated in Table 5.1 below.

Table 5.1 Photovoltaic performance parameters of PNDI-1Th:P3HT and PNDI-2Th:P3HT devices

Active layer	J_{sc} (mA/cm^2)	V_{oc} (V)	FF	PCE (%)
PNDI-1Th:P3HT	0.48	0.50	65	0.21
PNDI-2Th:P3HT	0.45	0.49	68	0.17

5.2.6 Conclusion

In conclusion, we have shown the photo-excitation and charge transfer in thin film blends of **PNDI-xTh** acceptors and a **P3HT** donor, and applied these films in photovoltaic devices. UV-Vis absorption spectra show that the complementary absorbance of **PNDI-2Th** compared to **P3HT** would allow nearly full spectrum harvesting of photons in the visible range. The **PNDI-1Th** and **PNDI-2Th** polymers also effectively quench the **P3HT** PL, a necessary step for using these materials in OPVs. PIA data has also shown that relatively long-lived positive and negative polarons are formed in **PNDI-1Th** and **PNDI-2Th** blends. OPV devices containing **PNDI-1Th** and **PNDI-2Th** had low PCEs attributable to small short current densities, and V_{oc} values below the theoretical maximum given the LUMO levels of the acceptors. AFM surface topology reveals low RMS roughness and no obvious phase segregation on the micron scale for PNDI-1Th and

PNDI-2Th blend films. However, the morphology is far from ideal and AFM alone gives little insight into the chemical purity of individual polymer domains or sub-surface structure. Incorporation of less common solvent, solvent combinations, and solvent additives may yield more favorable blend morphologies and increase short circuit current density. In addition, low bandgap high performance polymers with optimum HOMO and LUMO compared to polymer acceptors could improve the V_{oc} of future devices.

6 In-situ crosslinked and n-doped PNDI-xTh polymers as an efficient electron-transport layer in inverted polymer solar cells

6.1 Literature review and introduction

Organic photovoltaics (OPV) have the potential to be inexpensive and flexible alternatives to conventional silicon-based solar cells.[4, 99, 100] The performance of OPVs depends upon both the materials they are composed of, and the interfaces between those materials. Extensive research has been performed examining the electronic and optical properties of typical materials typically used in the active layers of OPVs: p-type donor polymers[101-104] and n-type fullerene-derived acceptors.[105-109] Power conversion efficiency (PCE) of OPVs have recently passed the landmark of 10%.[64] Although the current state-of-the-art OPVs have achieved remarkable current output, the stability of these cells still needs to be addressed. The long-term stability of OPVs in the conventional architecture (see Figure 6.1) suffers due to the oxidation of the low work function metals, either Al or Ca, used as photocathodes.[110] To address this concern, the inverted architecture was introduced, where the charge carrier movement is reversed relativer to the conventional architecture due to the materials in the electron transport layer (ETL) and hole transport layer (HTL) which selectively transport and block the appropriate charge carriers.[111-113]

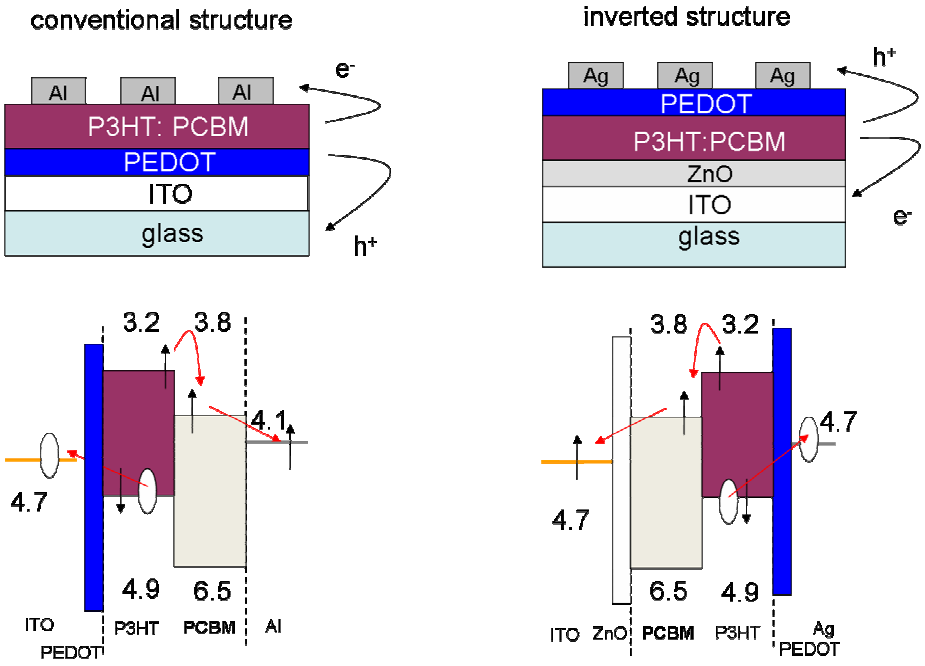

Figure 6.1 Conventional and inverted organic solar cells architectures. In the inverted structure ZnO is shown as the electron transport layer (ETL). P3HT and PCBM energy levels from literature[77, 90]

Typically, the ETL in inverted OPVs is composed of either ZnO or TiO_2.[114-116] These inorganic oxides have the appropriate energy levels to selectively transport electrons and block holes originating from the active layer to the ITO cathode. They are transparent to visible light, and have sufficient conductivity in nanometer thin films. However, the photoconductivity of ZnO can be altered by O_2 absorption under illumination,[117-119] which leads to decreased stability and short device lifetimes.[120]

An alternative ETL material needs to be able to satisfy a number of necessary requirements. It must have the appropriate energy levels, and sufficient conductivity in order to block holes and transport electrons. The ETL must also be resistant to organic solvents to ensure no solvent induced erosion occurs during processing of the active layer. In addition, low optical absorption is necessary to allow as much incident light as

possible to transmit through, to the active layer of the cell. Finally, the ETL needs to provide a smooth morphology on top of the ITO cathode, and good adhesion, with and surface energy compatibility with the active layer materials.

Organic materials have the potential to be high performing materials as ETLs due to the feasibility of tuning their electronic and optical properties through molecular design and synthesis. In particular, polymers offer the physical toughness and crack resistance necessary for flexible devices. Fullerene-based self-assembled monolayers crosslinked *in-situ* have already been shown to increase the efficiency and stability of inverted OPVs.[121, 122] To date, semiconducting polymers have seen limited use in as ETLs in OPVs due to a lack of solvent resistance that is necessary for multi-layer device processing.[123, 124]

Two inherent shortcomings of organic-based semiconducting polymers need to be addressed in order for them to be used as the ETL of inverted OPVs: conductivity and solvent resistance. Organic semiconductors have relatively low conductivities, and form poor electrical contact with electrodes compared to inorganic oxide-based ETLs.[125] Therefore, it is necessary to dope organic semiconductors to achieve sufficient conductivity for OPV operation. Increasing the conductivity of interfacial materials by chemical n-doping has been previously employed in vacuum-deposited organic small molecule solar cells.[126-129] However, n-doping polymers is more challenging than the n-doping small molecules. There are few n-dopants for organic polymers that are both stable, and solution processable. Wei *et al.* have recently reported using (4-(1,3-dimethyl-2,3-dihydro-1H-benzoimidazol-2-yl)phenyl)dimethylamine (N-DMBI) as an organic n-dopant in **PCBM** films.[130] Their work showed conductivities of **PCBM** films

doped with N-DMBI reach as high as 2×10^{-3} S/cm, Additionally, N-DMBI is soluble in common organic solvents and has demonstrated improved air stability in OFET devices with N-DMBI doped **PCBM** films compared to undoped devices.

The second major limiting factor for using organic semiconductors as interface materials is their poor solvent resistance. By definition, a solution processable ETL will be susceptible to solvent-based erosion during deposition of an active layer cast from organic solvents. To circumvent this problem, thermally crosslinkable interfacial layers based on organic small molecule semiconductors have been introduced to provide suitable solvent resistant films in both organic light-emitting diodes[131] and OPVs.[132, 133] Recently, an alternative crosslinking method using a bis(perfluorophenyl) azide (bisPFPA) crosslinker was utilized to produce crosslinked semiconducting polymer films.[134, 135] UV-induced photolysis of the azide moiety in bisPFPA produces active singlet nitrenes which can react with the alkyl side chains of semiconduting polymers with high photo-crosslinking efficiency. Because the alkyl solubilizing chains (and not the conjugated backbone) are crosslinked, this selective chemistry minimizes detrimental effects on the electrical properties of the semiconducting polymers, which are highly dependent upon a continuously conjugated backbone.

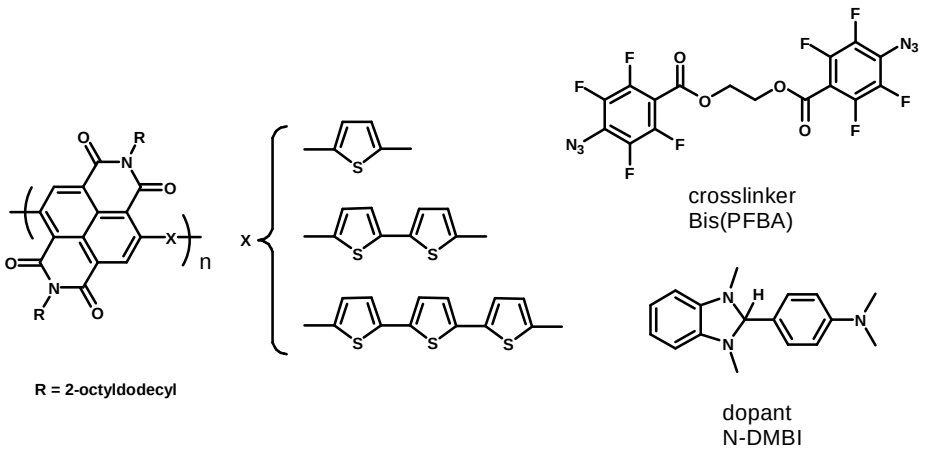

Figure 6.2 Chemical structure of PNDI-xTh polymers, the crosslinker Bis(PFBA) and the n-dopant N-DMBI

The following sections show the *in-situ* processing of an alternative ETL material comprised of PNDI-xTh polymers. The polymers were crosslinked under UV irradiation using Bis(PFBA), while concurrently n-doped with N-DMBI. These polymer-based ETL's show resistance to organic solvents used in the processing of the active layers, and sufficient conductivity to produce high performance inverted polymer solar cells with low series resistance (R_S) and high Fill Factor (FF). Chemically n-doping these organic polymer based ETLs increases the power conversion efficiencies of these cells from 0.7% to 3.4%.

6.2 Results and discussion

6.2.1 Properties of thiophene-NDI copolymer thin films

As shown in Chapter 2, NDI-thiophene copolymers have proven to be high performing n-type semiconductors in organic field effects transistors (OFETs). The synthesis and electrical characterization of the **PNDI-xTh** polymers used in this chapter is described in Chapter 2 and the experimental section. The crosslinker, bisPFPA and the dopant, N-

DMBI were synthesized according to previously reported methods.[136] To prepare the ETL films, N-DMBI, bisPFPA, and the NDI copolymers were co-dissolved in CB. The concentration of crosslinker, bisPFPA, relative to the polymers was optimized at 10 wt% and used subsequently for all devices. The doping concentration of N-DMBI relative to the polymers was varied from 0 to 15 wt%. In order to assess the film quality of the *in-situ* crosslinked and doped ETLs, optical microscopy images of a UV photo-pattern were taken. The film was covered with a photomask and exposed to deep UV light (λ = 254 nm) for 5 min at room temperature for photo-patterning, and then washed with CB to test its solvent resistance.

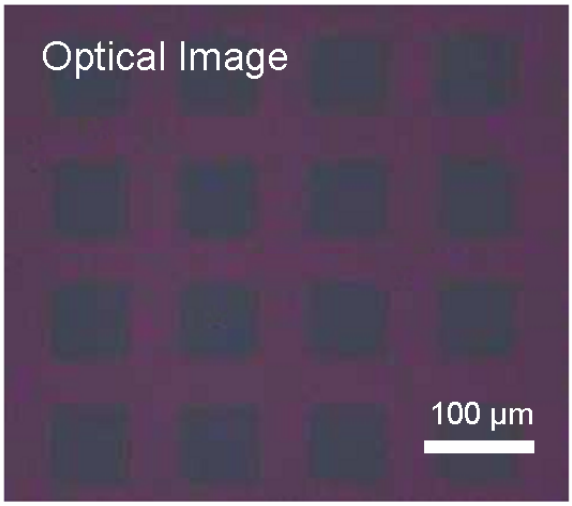

Figure 6.3 Photo-patterned x-PNDI-1Th (15%) washed with CB. Square pattern size 70 µm × 70 µm

As can be seen in Figure 6.3, UV-irradiated regions of the **PNDI-1Th** film containing 15 wt% of dopant (hereafter referred to as x-PNDI-1Th (15%)) was efficiently and homogeneously crosslinked and crosslinking occured only in the exposed areas (dark purple squares with distinct edges. Figure 6.4 shows the AFM surface morphology of the

crosslinked photo-patterned area. The film shows a smooth surface with low RMS roughness, and no discernable phase segregation.

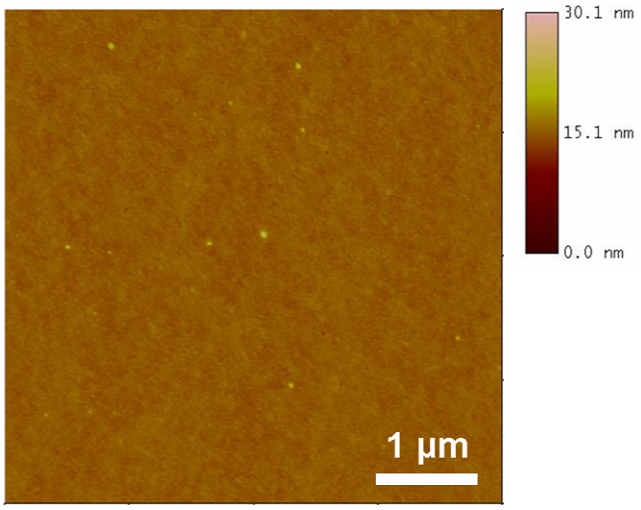

Figure 6.4 AFM image of x-PNDI-1Th (15%) scanned in the photo-patterned area.

Besides solvent resistance and interface compatibility, ETLs need to posses appropriate energy levels in order to transport electrons and block holes from the photocathode. Accordingly, the electronic structures of **PNDI-1Th** and **PNDI-1Th** (15%) were evaluated by X-ray photoelectron spectroscopy (XPS) as shown in Figure 6.5.

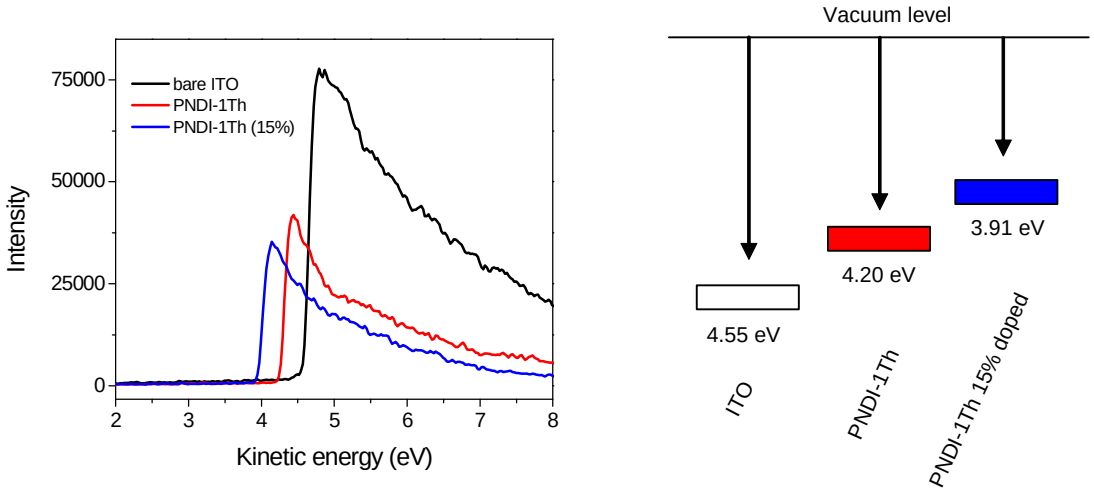

Figure 6.5 Secondary cutoffs of bare ITO, PNDI-1Th, and PNDI-1Th (15%) films on ITO substrates as measured by XPS

Using the onset of the secondary electron cut-off energy, the work function of ITO was measured to be 4.55 eV, corresponding to the ITO work function reported in the literature.[137] As Figure 6.5 shows, n-doping strongly reduces the work function of **PNDI-1Th** from 4.20 eV to 3.91 eV. This work function shift indicates the Fermi level position of the **PNDI-1Th** was shifted toward the **PCBM** LUMO level by increasing the number density of electrons through n-doping. In addition, this n-doping is likely to provide a greater hole-blocking potential than neat **PNDI-1Th** as the shift is away from the HOMO level of **P3HT**.

6.2.2 Electrical characterization

Since the electrical conductivities of the ETLs used in OPVs play a crucial role in device performance, we further investigated the electron-transporting properties of crosslinked and doped **PNDI-1Th** in OFET devices. **PNDI-1Th** and **x-PNDI-1Th** (0–15%) solutions

were prepared by the same method used for solar cell devices (polymer solutions were spin coated at 2000 rpm). The OFET devices were fabricated in the typical top-contact, bottom-gate geometry on hexamethyldisilazane (HMDS)-treated doped-Si/SiO_2 wafers. All device testing was performed in an inert atmosphere. A linear fit was applied in the saturation region of the sqrt I_{ds} vs V_g curve in order to calculate the charge carrier mobility using the standard equation of metal-oxide-semiconductor field-effect transistors: $I_{ds} = (\mu W C_0/2L)(V_g - V_t)^2$.

The characteristics of OFETs using the neat polymer (**PNDI-1Th**) showed typical n-type behavior at positive gate-source bias (V_g = +100 V), with an electron mobility of 1.9×10^{-4} cm^2/Vs similar to those reported previously in Chapter 2 (Figure 6.6 and Table 6.1). Crosslinking of **PNDI-1Th** decreased the electron mobility to 4.7×10^{-6} cm^2/Vs, which is likely due to the crosslinked network structure disrupting the regular molecular packing of the polymer. The on/off ratios of **PNDI-1Th** increased from 10^2 to 10^4 and the threshold voltage shifted slightly from 6 V to 13 V after crosslinking.

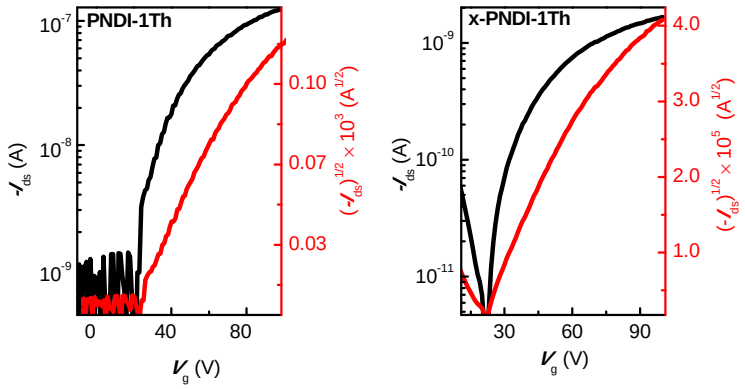

Figure 6.6 Transfer characteristics of OFETs with PNDI-1Th (left) and x-PNDI-1Th (right)

Table 6.1 OFET electrical properties for PNDI-1Th before and after crosslinking

ETM	μ ($cm^2/V \cdot s$)	$I_{on/off}$	V_t (V)
PNDI-1Th	1.9 (±0.1) × 10^{-4}	10^2	6 (±2)
x-PNDI-1Th	4.7 (±0.2)× 10^{-6}	10^4	13 (±3)

The devices comprised of n-doped **x-PNDI-1Th** revealed that n-doping significantly improves the electrical conductivity of the polymer. All of the doped devices exhibit field-independent I-V behavior with negligible on/off ratios, which is typical of conductors as shown in Figure 6.7 (a).

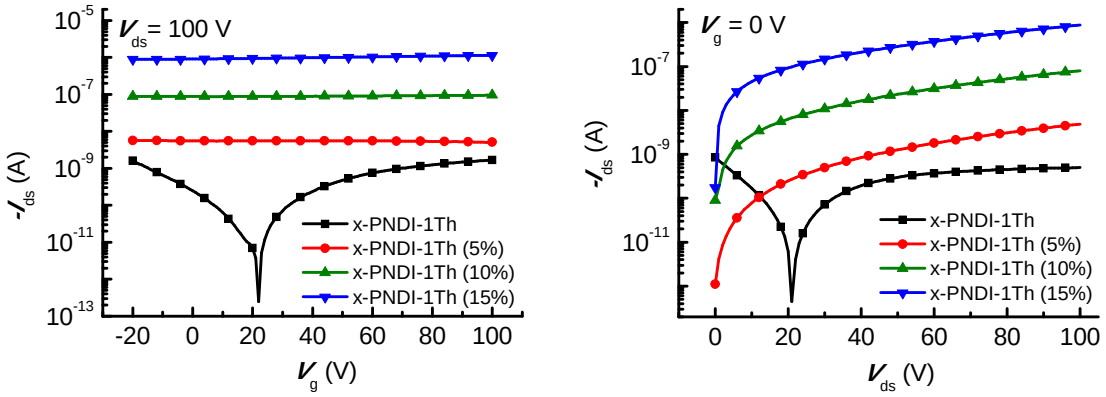

Figure 6.7 (a) Transfer curve of x-PNDI-1Th with varying doping concentrations and (b) Output characteristics of x-PNDI-1Th at various doping concentrations

Figure 6.7 (b) shows that the output current of devices increased with increasing doping concentration. The field-effect conductivity was derived from gated two-terminal measurements with the equation $\sigma = (L/A)(I_{ds}/V_{ds})$, where L and A are the channel length

and cross-sectional area of the devices, respectively.[138] As the doping concentration increased from 0 to 15%, the conductivity increased monotonically from 1.6×10^{-6} S/m to 4.0×10^{-3} S/m. The dependence of conductivity on the doping concentration of x-**PNDI-1Th**-based OFET devices helps explain the observed improvement in PCE of the solar cells shown later in this section. A summary of the electrical characteristics are shown below.

Table 6.2 Summary of conductivity for x-PNDI-1Th at different doping concentrations measured from OFET devices.

Active layer	σ (S/m)
x-PNDI-1Th	$1.6\ (\pm 0.2) \times 10^{-6}$
x-PNDI-1Th (5%)	$2.4\ (\pm 0.2) \times 10^{-5}$
x-PNDI-1Th (10%)	$3.8\ (\pm 0.4) \times 10^{-4}$
x-PNDI-1Th (15%)	$4.0\ (\pm 0.4) \times 10^{-3}$

6.2.3 Solar cell performance

OPVs were fabricated in the inverted architecture with an ITO/ETL/P3HT:$PC_{61}BM$/PEDOT:PSS/Ag stack structure and tested under simulated AM 1.5G illumination at 100 mW/cm^2 (see experimental section for detailed procedures). Three different NDI copolymers, which were crosslinked *in-situ* and n-doped from 0 to 15%, were used as ETLs. The thickness of the ETL films was optimized (about 20 nm thick) to reduce series resistance (R_s) and light absorption, while sustaining good electron

transport properties. A conventional ZnO ETL was used as a basis for comparison with the NDI copolymer base layers. The performance of the devices is shown in Figure 6.8 and the photovoltaic parameters are summarized in Table 6.3.

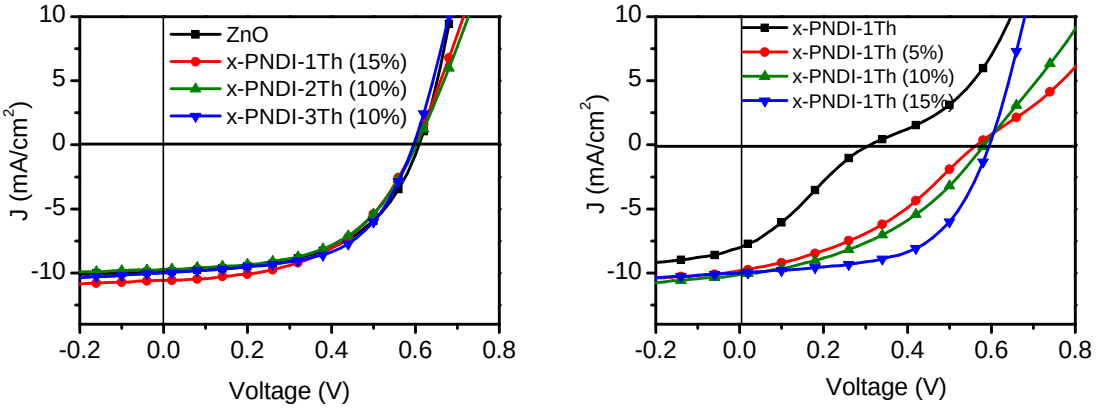

Figure 6.8 J–V characteristics of inverted OPVs for (a) ZnO and three different NDI copolymers with optimal doping levels showing maximum PCEs and (b) the evolution of J–V curves as doping concentration increases in x-PNDI-1Th layers.

Table 6.3. Summary of OPV device performance with ZnO and x-PNDI-1Th (0–15%)

ETM	V_{oc} (V)	J_{sc} (mA/cm^2)	FF	PCE (%)	R_s ($\Omega \cdot$cm^2)
ZnO	0.61 (±0.03)	9.97 (±0.05)	0.53 (±0.03)	3.2 (±0.2)	8 (±1)
x-PNDI-1Th	0.30 (±0.02)	8.25 (±0.05)	0.28 (±0.01)	0.7 (±0.1)	64(±3)
x-PNDI-1Th (5%)	0.57 (±0.03)	10.30 (±0.05)	0.36 (±0.02)	2.10 (±0.1)	41 (±2)
x-PNDI-1Th (10%)	0.58 (±0.03)	10.60 (±0.05)	0.39 (±0.02)	2.4 (±0.1)	24 (±1)
x-PNDI-1Th (15%)	0.59 (±0.03)	10.00 (±0.05)	0.58 (±0.03)	3.4 (±0.2)	12 (±1)

All devices with undoped NDI copolymers exhibit an s-shape kink in the current density-voltage (J–V) curves (Figure 6.8(b) for **PNDI-1Th** and Figure 6.9(a) and (b) for **PNDI-2Th** and **PNDI-3Th**, respectively). Upon increasing the doping concentration of the crosslinked films, devices show a progressive evolution of diode behavior in the J–V curves with improved J_{sc}, V_{oc}, FF, and PCE. Specifically, the PCE of the device with **PNDI-1Th** increases significantly from 0.7% to 3.4% with an increase in doping concentration from 0 to 15 wt% (Figure 6.8(b)). In addition, the optimized device using n-doped **PNDI-1Th** showed better performance than the control devices using ZnO as the ETL (PCE: 3.2%). **PNDI-2Th** and **PNDI-3Th** also showed the same trend of increasing PCEs, with increasing doping concentration but the maximum PCE was obtained at 10 wt% relative to the polymer (Figure 6.9(a) and (b)). The maximum PCEs of the devices with x-**PNDI-2Th** (10%) and x-**PNDI-3Th** (10%) were both 3.2% and 3.2%. A summary of the photovoltaic properties is shown in Table 6.3 and 6.4.

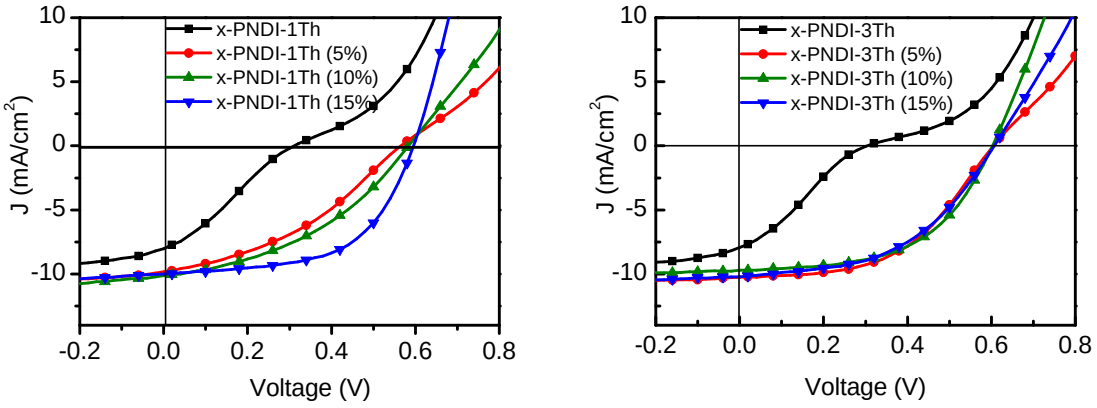

Figure 6.9 Evolution of J-V curves with increasing doping concentration in x-PNDI-2Th and PNDI-3Th ETLs.

The overall improvement in device efficiency as doping level increases is attributed to the increase in electrical conductivity and improved electron extraction efficiency for the NDI copolymers as a result of these increased doping levels. It is noteworthy that, in general, the J_{sc} and V_{oc} were largely improved by increasing doping concentrations from 0 to 5 wt% and then plateaued above 5 wt%. The enhanced conductivity of the polymers (as shown in the previous section) also results in an overall decrease in series resistance (R_s), and an increase in FF. The calculated R_s value of devices using undoped **x-PNDI-1Th** is 64 $\Omega \cdot cm^2$. By increasing the doping concentration up to 15 wt%, the R_s decreased to 12 $\Omega \cdot cm^2$ (Table 6.3). The devices with **x-PNDI-2Th** and **x-PNDI-3Th** also showed the same trend, a decreasing R_s with an increase in doping concentration, as shown in Table 6.4.

Table 6.4 Performance summary of OPV device fabricated with x-PNDI-2Th (0-15%) and x-PNDI-3Th (0-15%)

ETL	V_{oc} (V)	J_{sc} (mA/cm^2)	FF	PCE (%)	Rs ($\Omega \cdot cm^2$)
x-PNDI-2Th	0.30 (±0.02)	9.0 (±0.5)	0.31 (±0.01)	0.9 (±0.1)	37 (±2)
x-PNDI-2Th (5%)	0.52 (±0.03)	10.4 (±0.5)	0.42 (±0.02)	2.3 (±0.1)	29 (±1)
x-PNDI-2Th (10%)	0.60 (±0.03)	10.5 (±0.5)	0.52 (±0.03)	3.2 (±0.2)	13 (±1)
x-PNDI-2Th (15%)	0.59 (±0.02)	10.4 (±0.5)	0.47 (±0.02)	2.9 (±0.1)	13 (±1)
x-PNDI-3Th	0.30 (±0.02)	8.3 (±0.5)	0.26 (±0.01)	0.6 (±0.1)	102 (±5)
x-PNDI-3Th (5%)	0.60 (±0.03)	10.4 (±0.5)	0.49 (±0.02)	3.1 (±0.1)	27 (±1)
x-PNDI-3Th (10%)	0.60 (±0.03)	9.7 (±0.5)	0.54 (±0.03)	3.2 (±0.1)	14 (±1)
x-PNDI-3Th (15%)	0.60 (±0.03)	9.6 (±0.5)	0.52 (±0.03)	3.0 (±0.1)	20 (±1)

As seen in Table 6.3 and Table 6.4, there is a small but notable difference in PCE among the devices with the three undoped polymers. The device with **x-PNDI-2Th**

shows the highest PCE (0.9%), while the devices with **x-PNDI-1Th** and **x-PNDI-3Th** exhibit lower PCE values of 0.7 and 0.6%, respectively. For undoped polymer ETLs, there are two important factors governing device performance. One is the charge carrier mobility, and the other is the HOMO and LUMO energy level of the polymers. As reported in previous publications, the electron mobilities of **PNDI-1Th**, **PNDI-2Th** and **PNDI-3Th** were 3.1×10^{-3}, 3.9×10^{-2} and 7.6×10^{-2} cm^2/Vs.[61] The higher PCE and J_{sc} for the device containing **x-PNDI-2Th** may originate from superior electron mobility compared to **x-PNDI-1Th**. Although **PNDI-3Th** has the highest electron mobility, the PCE of the device containing **x-PNDI-3Th** is lower than that of **x-PNDI-1Th** and **x-PNDI-2Th**. This is likely due to energy level matching, as the HOMO level of **PNDI-3Th** (5.13 eV) is very close to the HOMO level of P3HT (5.10 eV),[61] which would decrease the hole blocking ability of **PNDI-3Th**-based ETLs. **PNDI-1Th** and **PNDI-2Th** should exhibit better hole-blocking abilities due to their deeper lying HOMO levels (-5.62 eV and -5.30 eV, respectively). On the other hand, similar efficient electron transport from **PCBM** to each of the NDI copolymers due to the LUMO levels should be observed, with the LUMOs of **PNDI-1Th**, **PNDI-2Th** and **PNDI-3Th** being -3.85 eV, -3.79 eV and -3.76 eV.

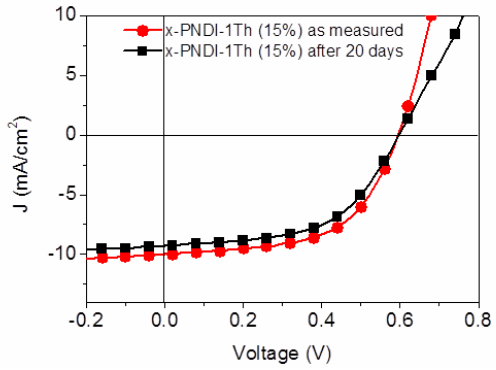

Figure 6.10 J–V characteristics of un-encapsulated inverted OPVs with x-PNDI-1Th (15%) before and after exposure to ambient conditions for 20 days.

Compared to conventional OPVs, the main advantage of inverted OPVs is their improved air-stability. Recently, the Bao group reported that OFET devices with N-DMBI doped **PCBM**[130] and pyronin B-doped perylene diimide[139] active layers show exceptional device stability in ambient conditions. To examine the air stability of the devices with **x-PNDI-1Th** (15%), unencapsulated inverted OPVs were fabricated, and device parameters were measured after storage in air for 20 days. The devices measured immediately after fabrication showed a PCE of 3.4% with V_{oc} of 0.59 V, J_{sc} of 10.0 mA/cm^2 and FF of 0.58 (Table 6.3). After 20 days, the PCE remained at 88% of the original value (PCE: 3.0%, V_{oc}: 0.59 V, J_{sc}: 9.3 mA/cm^2 and FF: 0.54) (Figure 6.10).

6.2.4 Conclusion

In conclusion, this section has demonstrated a new application uniquely suited to the **PNDI-xTh** copolymers. Through the use of *in-situ* n-doping and crosslinking, we were able to create a solvent resistant, high conductivity electron transport layer for inverted OPVs. Chemical n-doping was shown to decrease the *R*s and increase the FF of OPVs

contains these interfacial layers. The power conversion efficiency of cells containing these ETLs are comparable to the PCE of conventional inverted OPVs which contain ZnO in the ETL. In addition, the cells containing the **PNDI-xTh** ETLs showed good air-stability and consistent performance after 20 days of storage. This work helps to pave the way to all-organic OPVs, using solution processed multilayer devices.

7 Fused-thiophene naphthalene diimide copolymers for organic thin film transistors

7.1 Introduction

The following chapter describes the synthesis and characterization of a series of three naphthalene diimide-based donor-acceptor copolymers. Each of the polymers contains an acceptor unit made of a naphthalene diimide core with octadodecyle solubilizing chains, as discussed in previous sections. The co-monomers are three different fused thiophene donor units with varying electron donating potential. Optical properties of the polymers will be investigated with UV-Vis absorption spectroscopy. The thin film morphology of the copolymers will be investigated with atomic force microscopy and X-ray diffraction. Finally, the electrical performance of these materials will be evaluated using organic field-effect transistors.

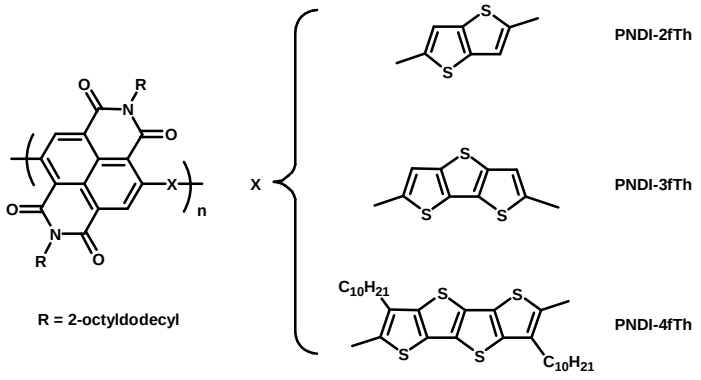

Figure 7.1 Chemical structures of the PNDI-xfTh copolymers presented in this study

The chemical structure of the NDI-fused ring thiophene copolymers polymers is shown in Figure 7.1 The polymers were synthesized via Stille coupling from a bromine functionalized NDI monomer and three different trimethyl tin functionalized fused thiophenes. **PNDI-2fTh** contains alternating series of NDI and a unit comprised of two fused thiophenes. **PNDI-3fTh** contains the same NDI monomer and a co-monomer made up of three fused thiophenes. The final polymer, **PNDI-4fTh**, contains NDI and four fused thiophene unit. To enhance processibility, solubilizing alkyl chains were incorporated into the monomer containing four fused thiophene rings. Detailed synthesis can be found in the experimental section. Multiple Soxhlet extractions were used to purify the polymers before characterization. The molecular weights of the polymers were determined with size-exclusion chromatography in THF relative to polystyrene standards. The measured number-average molecular weights of the polymers were relativity high, from 21.3 kDa to 92.4 kDa for **PNDI-3fTh** and **PNDI-4fTh** respectively. This overestimation could be due to the rigid-rod-like structure of the NDI moeity as shown in previous sections. The results are shown in Table 7.1 below.

Table 7.1 Number average molecular weight (M_n) and polydispersity index (PDI) of PNDI-xfTh polymers

	M_n (kDa)	PDI
PNDI-2fTh	**62.5**	**3.3**
PNDI-3fTh	**21.3**	**2.9**
PNDI-4fTh	**92.4**	**3.6**

7.2 Results and discussion

7.2.1 Optical characterization

The UV-Vis absorbance in solution and thin film is shown in Figure 7.2. All three polymers show two absorption peaks. Each polymer has a $\pi \rightarrow \pi^*$ transition band[140] centered at 390 nm 400 nm and 407 nm for **PNDI-2fTh**, **PNDI-3fTh**, and **PNDI-3fTh** respectively. In addition, the **PNDI-3fTh** absorbance shows a distinct shoulder peak at 310 nm. **PNDI-2fTh** shows a less distinctive shoulder at 395 nm. Each polymer also has a charge transfer band[90] which appears at longer wavelengths, in the red region of the spectrum. These peaks are centered at 560 nm, 700 nm and 710 nm for **PNDI-2fTh**, **PNDI-3fTh** and **PNDI-4fTh** respectively. As the UV-Vis absorbance shows, the $\pi \rightarrow \pi^*$ band is red shifted as the number of thiophene units are increased. This is commensurate with the increase in conjugation length of the donor thiophene moetity as extra rings are incorporated.

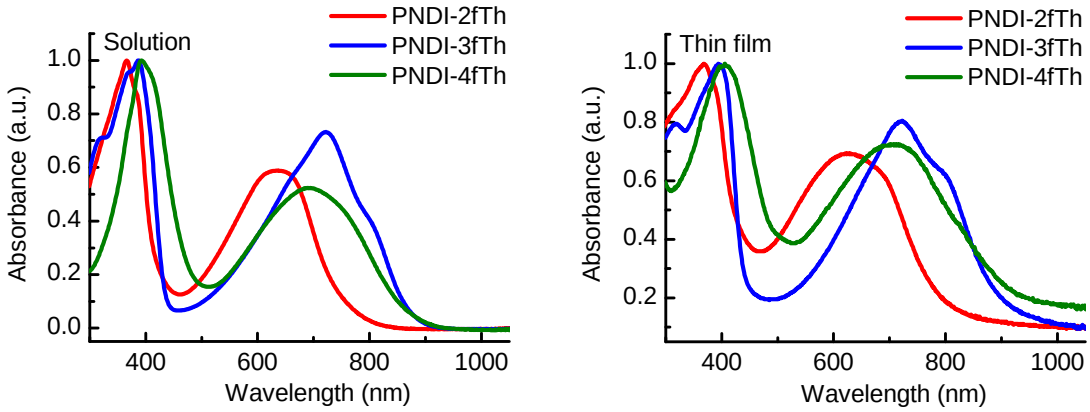

Figure 7.2 UV-Vis absorbance spectra of PNDI-xfTh polymers in $CHCl_3$ solution (left) and cast as thin films (right)

The ICT band is also red shifted as the number of thiophene units is increased. The onset of the optical absorption compared to background was used to calculate the thin film bandgaps (Eg) of the polymers. **PNDI-2fTh** has a bandgap of 1.75 eV. **PNDI-3fTh** and **PNDI-4fTh** have optical bandgaps of 1.40 eV and 1.37 eV respectively. The decrease in band gap of **PNDI-2fTh** and **PNDI-3fTh** compared to **PNDI-2fTh** is due to the change in HOMO level afforded by the increase in donation character as the number of thiophene rings increases. This increase seems to saturate when three fused thiophenes are used, as the decrease in band gap of **PNDI-3fTh** to **PNDI-4fTh** is quite small. These results are summarized in Table 7.2.

Table 7.2 Optical and electrochemical properties of the PNDI-xfTh polymers

	λ_{max} (nm)	HOMO (eV)	LUMO (eV)	E_g (eV)
PNDI-2fTh	368	-5.4	-3.8	1.57
PNDI-3fTh	391	-5.3	-3.9	1.40
PNDI-4fTh	412	-5.3	-3.9	1.37

Cyclic voltammetery performed in a typical three electrode cell vs. $Ag/AgNO_3$ was used to determine the energy levels of the three polymers as cast on a Pt wire working electrode.. All three polymers showed reversible reduction scans over many cycles. As shown in Figure 7.3, **PNDI-2fTh** and **PNDI-3fTh** showed two stable reduction waves, while **PNDI-4fTh** shows only a single wave. Oxidation scans of all three polymers were only stable for a couple runs, before a sharp reduction in current signal. LUMO energies were calculated compared to ferrecene (-4.8 eV) which was used as an internal reference. The LUMO of all three polymers is close to -3.8 eV, which is

comparable to the LUMO of the NDI monomer, and similar to the LUMO level showed for other donor-acceptor polymers using the NDI as shown in previous sections. The HOMO level of the three polymers was calculated using the thin film optical band gaps, as the oxidation scans were not repeatable. The HOMO level of the **PNDI-3fTh** (-5.3 eV) is slightly higher than **PNDI-2fTh** (-5.4 eV), attributable to the greater electron donating character of the three fused thiophene monomer. This trend does not continue, as the HOMO level of **PNDI-4fTh** (-5.3 eV) is similar to that of **PNDI-3fTh**. The results are summarized in Table 7.2.

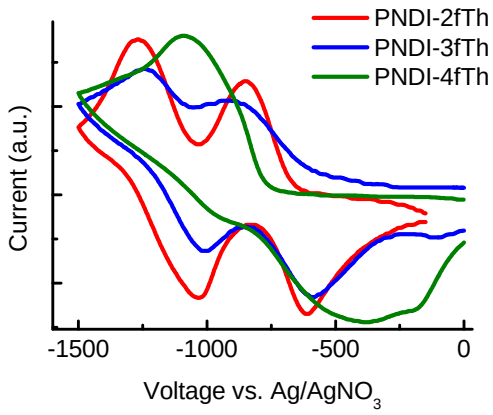

Figure 7.3 Cyclic voltammograms of PNDI-2fTh, PNDI-3fTh, and PNDI-4fTh vs. $Ag/AgNO_3$

7.2.2 Morphology

AFM was used to characterize the surface morphology of the three polymer films. Samples were prepared under the same conditions as those used to fabricate the

optimized OFET devices in order to determine any relation between surface morphology and electrical performance.

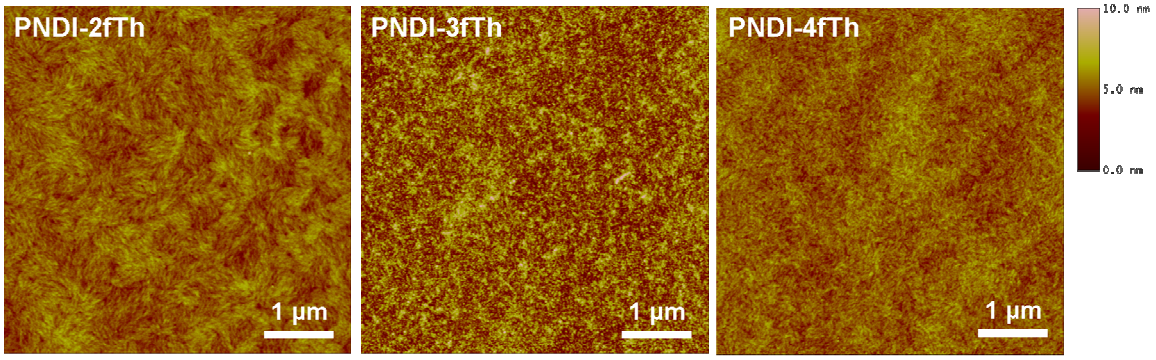

Figure 7.4 Tapping mode AFM height images of PNDI-2fTh, PNDI-3fTh, and PNDI-4fTh. Z-scale for all images is 10 nm.

As can be seen in Figure 7.4, the **PNDI-2fTh** film shows feathery-looking, rod-like structures on the sub-micron scale. There are no discernable distinct domain, nor signs of de-wetting or phase segregation. The **PNDI-3fTh** film is more granular in appearance than the **PNDI-2fTh** scan. No apparent organization can be seen in the surface morphology. Although AFM can not be used to succinctly identify relative crystallinity of polymer films, there is no clear evidence of a regular pattern or crystalline features in the **PNDI-3fTh** film. The **PNDI-4fTh** displays feathery rod-like features as in the **PNDI-2fTh** film, but at a reduced size scale, and with less distinct boundaries. It is less granular in appearance compared to the **PNDI-3fTh** film. Smooth films are typically necessary for optimum ohmic contact with electrodes in top-contact OFET devices (like the ones used in this study). The surface RMS roughness of all three polymer films was below 1 nm, satisfying the requirement.

The solid state packing structure of the three polymers was investigated by X-ray diffraction of thin films cast on SiO_2 substrates and annealed under the same conditions as the optimized OFET devices. As can be seen in Figure 7.5 all three polymers show a distinct diffraction peak between 3.9° and 4.1°. This corresponds to an inter-lamellar d-spacing between 22 Å and 23Å. This spacing is similar to the inter-lamellar spacing shown for NDI-based polymers in the other sections which is to be expected. The results are summarized in Table 7.3. Differential scanning calorimmetry (DSC) was performed on the three polymers to determine any crystalline thermal transitions as AFM and XRD indicate some crystalline structure in the polymer films. However, the DSC scans show no clear features between 20 °C and 300 °C.

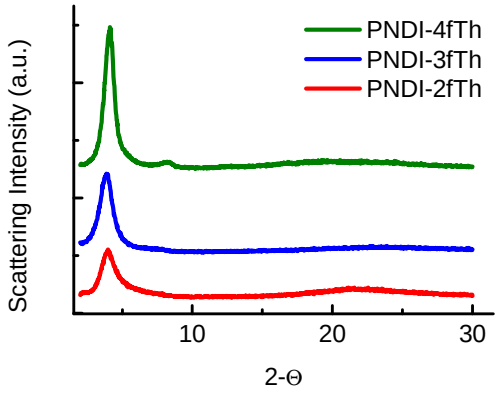

Figure 7.5 X-ray diffraction patterns of PNDI-2fTh, PNDI-3fTh and PNDI-4fTh cast as thin films

Table 7.3 XRD results and calculated d-spacing of PNDI-2fTh, PNDI-3fTh and PNDI-4fTh

	Angle 2Θ (degrees)	d-spacing (Å)
PNDI-2fTh	4.0	22
PNDI-3fTh	3.9	23
PNDI-4fTh	4.1	22

7.2.3 OFET characterization

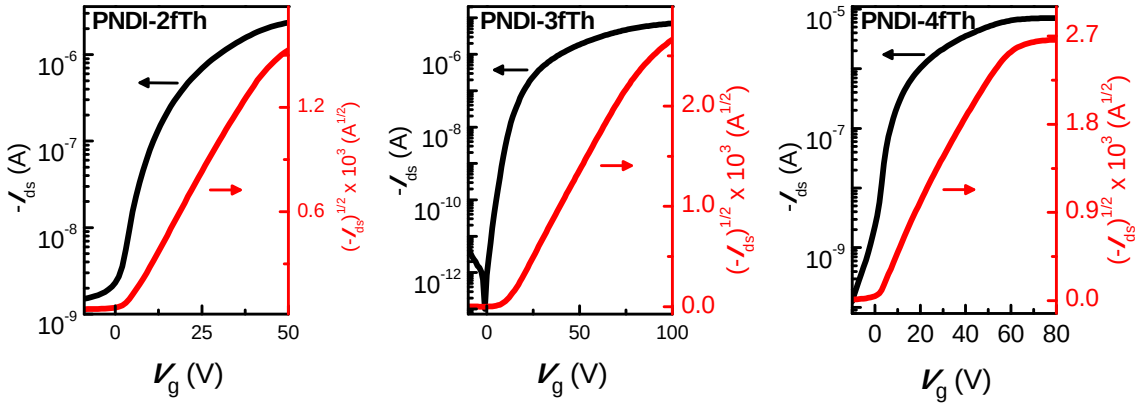

Figure 7.6 Transfer characteristics of the PNDI-xfTh OFETs. Drain current vs. gate voltage (black) sqrt of drain current vs. gate voltage (red).

Organic field-effect transistors were fabricated with the **PNDI-xfTh** polymers as active layers, in order to asses the electrical performance of these materials. Devices were constructed on doped-Si/SiO_2 wafers in the typical bottom-gate/top-contact geometry using diviyl-tetramethylsiloxane-bis(benzocyclobutene) (BCB) to enhance the hydrophobicity of the oxide surface. **PNDI-2Th** and **PNDI-4fTh** were spin-cast from a $CHCl_3$ solution. **PNDI-3fTh** was spin-cast from chlorobenzene. All device fabrication

and testing was performed in an inert atmosphere. Devices were optimized in terms of surface treatment, solvent choice, thickness, and annealing temperature.

The transfer characteristics of the devices is shown in Figure 7.6. Each of the three polymers showed typical n-type behavior at positive gate-source bias (V_g = +100 V), and negligible current under negative bias. Leakage currents for all devices was under 10^{-12} A, which is near the detection limit of the semiconductor parameter analyzer. A linear fit was applied in the saturation region of the sqrt I_{ds} vs V_g curve to calculate the charge carrier mobility using the standard equation for metal-oxide-semiconductor field-effect transistors: $I_{ds} = (\mu W\ C_0/2L)(V_g - V_t)^2$. Device aspect ratios (W/L) between and 12.5 and 66.6 were tested containing channel lengths from 15 μm to 80 μm. There was little to no effect due to electrode geometry on performance. **PNDI-2fTh** has an electron mobility of 7 (±2) × 10^{-3} cm^2/Vs and **PNDI-3fTh** had a mobility of 4.8 (±0.5) × 10^{-3} cm^2/Vs. **PNDI-4fTh** had the highest mobility of the series (1.2 (±0.6) × 10^{-2} cm^2/Vs). All three polymers had threshold voltages (V_t) of 10 V or less, and steep sub-threshold slopes. **PNDI-2fTh** and **PNDI-4fTh** displayed maximum drain current at gate voltages from +50 V to +100 V. Maximum current delivered by **PNDI-3fTh** did not arrive until V_g = 100 V. The results are summarized in Table 7.4 below.

Table 7.4 Electrical performance of the PNDI-xfTh polymers as measured in OFET devices. All values are the average of at least 10 devices.

	μ_e (cm2/Vs)	$I_{on/off}$	V_t (V)
PNDI-2fTh	7 (±2) × 10^{-3}	10^4	2
PNDI-3fTh	4.8 (±0.5) × 10^{-3}	10^8	10
PNDI-4fTh	1.2 (±0.6) × 10^{-2}	10^5	1

7.2.4 OPV characterization

In order to access the photovoltaic properties of these n-type polymers, bulk heterojunction OPVs were constructed in the conventional architecture using glass/ITO/PNDI-xfTh:P3HT active layer/Al stacks. The active layers were deposited from chloroform solution using 2:1 n-type polymer to P3HT weight ratios for **PNDI-2fTh** and **PNDI-3fTh**. Device constructed with **PNDI-4fTh** showed the best performance with 1:1 n-type polymer to **P3HT** ratio. All devices were fabricated and annealed (150 °C for 10 minutes) in a nitrogen filled glove box. The devices were tested in air under standard AM1.5 illumination. Detailed fabrication procedures can be found in the experimental section. As can be seen in Figure 7.7, **PNDI-4fTh**-based cells displayed the highest short circuit current density (0.57 mA/cm^2) of the three polymers. **PNDI-3fTh** devices had relatively smaller short circuit current densities (0.46 mA/cm^2), and **PNDI-3fTh** devices produced the smallest amount of photocurrent (0.19 mA/cm^2). in the polymer series. All three polymers displayed similar open circuit voltages (around 0.50 V) comparable to NDI polymers shown in previous chapters. The fill factors of **PNDI-4fTh** and **PNDI-3fTh** devices were 55% and 48%. **PNDI-2fTh** OPVs had relatively lower fill factors (39%) and an s-shaped J-V curve. The PCE of **PNDI-4fTh**

OPVs was the highest of the series at 0.13 %, while **PNDI-2fTh** and **PNDI-3fTh** has PCEs of 0.04 % and 0.11 % respectively. Short circuit current density had the largest influence on PCE for this series of materials, and explains why **PNDI-4fTh** had the overall highest efficiency. The relatively small J_{sc} produced by **PNDI-3fTh** resulted in the lowest PCE of the three polymers. The PCEs of these three materials are similar to the efficiencies measured for NDI polymers shown in previous sections. As **PNDI-4fTh** had the highest mobility of the three materials, it is not surprising that it also returned the highest power conversion efficiency. The results are summarized in Table 7.5.

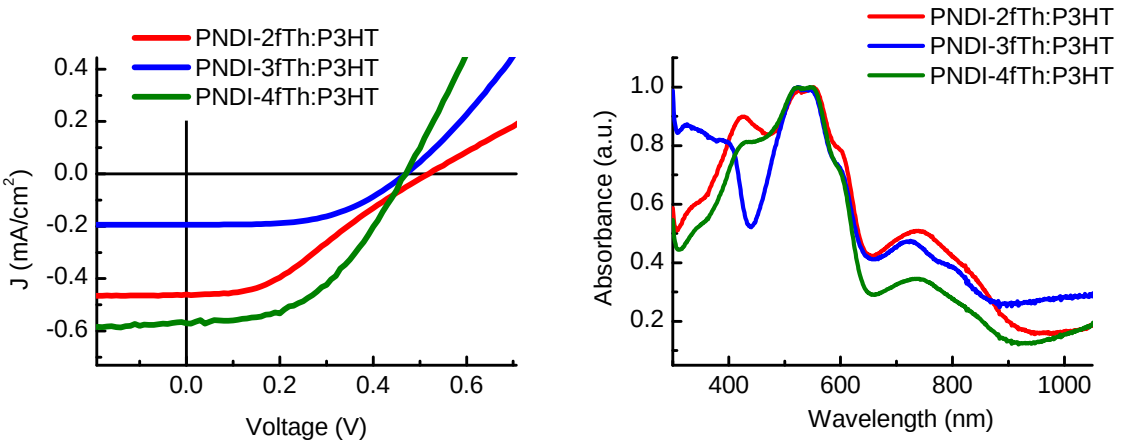

Figure 7.7 J-V characteristics of PNDI-xfTh:P3HT OPVs (left) and UV-Vis absorption spectra of PNDI-fTh:P3HT blend thin films

Table 7.5 Photovoltaic properties of PNDI-xfTh:P3HT OPVs

Active layer	J_{sc} (mA/cm^2)	V_{oc} (V)	FF	PCE (%)
PNDI-2fTh:P3HT	0.46 (±0.02)	0.51 (±0.01)	39 (±1)	0.11 (±0.01)
PNDI-3fTh:P3HT	0.19 (±0.01)	0.48 (±0.01)	48 (±1)	0.045 (±0.003)
PNDI-4fTh:P3HT	0.57 (±0.02)	0.47 (±0.02)	55 (±4)	0.13 (±0.01)

7.2.5 Conclusion

In conclusion, we have shown a series of donor-acceptor semiconducting polymers using a naphthalene diimide unit and a group of fused thiophene donors. The thin film band gaps of the polymers scale with the donating character of the fused thiophene co-monomer. The thin film morphology of the four polymers was assessed with AFM, and showed a fibular fan-like structure for polymers **PNID-2fTh** and **PNDI-4fTh**. All three polymers show some crystallinity as measured by XRD. In optimized OFET devices, **PNDI-4fTh** had the highest electrical performance of the series (μ_e-= 1.2 (±0.6) × 10^{-2} cm^2/Vs). Due to the electrical performance and solution processability of these materials, the **PNDI-xfTh** polymers were applied to OPVs. Devices containing **PNDI-4fTh** had the highest PCE of the three polymers (0.13 %). The OPVs had similar performance to NDI based polymers as shown in similar sections.

8 Conclusion and future outlook

We have shown the synthesis and characterization of p-type and n-type semiconducting thiophene copolymers. The materials research presented in this work was motivated by the need for inexpensive, environmentally stable, flexible and lightweight materials in organic electronics. Organic semiconducting polymers have the potential to replace for inorganic materials in electronic devices, but this potential can not be fully realized until fundamental materials characterization, like that which is shown in this work, is completed. The semiconducting copolymers in this work have exhibited excellent environmental stability in organic electronic devices.[141] The NDI-based polymers in have proved useful in two different applications: transistors,[61, 62] and electron transport layers in inverted OPVs.[142]

The naphthalene diimide-thiophene donor-acceptor coplymers were shown to have electron mobilities as high as 0.076 cm^2/Vs achieved in OFETs from **PNDI-3Th.** By employing alternative OFET device architectures such as top-gate bottom-contact and the use of various dielectrics and printing fabrication techniques, the measurable performance of **PNDI-3Th** should be able to exceed that of **PNDI-2Th** (0.85 cm^2/Vs) which was reported by Facchetti *et al.*[7]

The high electron-mobility, energy levels, and absorption spectrum of the **PNDI-xTh** and polymers lead to investigation of these materials as an acceptor material in all-polymer solar cells. **PNDI-1Th** and **PNDI-2Th** effectively quench the **P3HT** PL, a necessary step for using these materials in OPVs. In addition, PIA data has also shown that relatively long-lived positive and negative polarons are formed in **PNDI-1Th** and **PNDI-2Th** blends.

The **PNDI-xTh** polymers were then investigated as a candidate to replace ZnO as the electron transport layer in inverted OPVs. Through the use of *in-situ* n-doping and a novel alkyl UV-mediated crosslinking method, we were able to create a solvent resistant, and high conductivity electron transport layers. Chemical n-doping was shown to decrease electrical resistance and increase the FF of OPVs using these polymers. The device performance of cells containing these ETLs (PCE = 3.4 %) is comparable to cells which contain ZnO in the ETL.

8.1 Potential future directions

8.1.1 Screen printed inverters and logic circuits

This work presented the synthesis and characterization of both p-type polymers (carboxylated polythiophenes) and n-type polymers (naphthalene diimides). Both of these polymers were shown to be solution processable in common organic solvents. Individually, these materials can make n-channel and p-channel transistors. An ambipolar semiconductor has previously been used by Kim *et al.* to fabricate both transistors and complementary inverters. Drop casting from solution was used to deposit the polymer on a pre-patterned substrate. This method however is not possible using two materials with similar solubility.

The fabrication of inverters using ink-jet printing has recently been accomplished by Baeg *et al.*[144] They used n-type and p-type semiconducting polymers (including **P3HT)** as in their study. Their work demonstrates the possibility of alternative device fabrication method compared to spin-coating to form circuits from two different materials.

Screen printing is another processing technique which could be used to fabricate inverters and logic circuits comprised of two different semiconducting materials. Screen printing allows the ability to fabricate large area devices, as well as deposit two materials on the same substrate without the solvent based erosion which would be caused by spin coating two separate layers. After the optimization solutions blends for solvent and viscosity, they could be deposited onto pre-patterned substrates to form logic gates, and complementary inverters. The carboxylated p-type polymers shown in a previous section have advantages compared to the materials used by Baeg *et al.* because they are chemically stable and can be processed and tested in air. While spin coating can be accomplished in the inert atmosphere of a glove box, large scale screen printing would be much easier to accomplish in air.

8.1.2 P-N block copolymers

A P-N block copolymer with an A-A-A-B-B-B structure might be the ideal solar cell material. Because the p-type and n-type parts of the polymer are so close (covalently bonded in fact), exciton separation may be enhanced compared to bulk heterojunction blends. Block copolymers are known to self assemble into a variety of different structures[145] depending on the relative molecular weights of the different blocks and the χ value, which roughly equates to the difference in chemical potential between the two blocks. A possible P-N block co-polymer is shown in Figure 8.1.

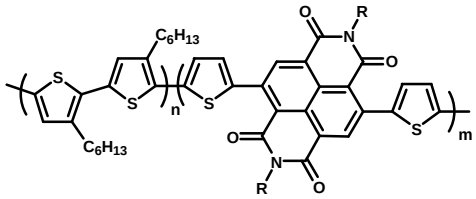

P3HT-b-PNDI-2Th

Figure 8.1 Chemical structure of a proposed P-N block copolymer made from a p-type P3HT block and an n-type PNDI-2Th block.

In the structure above, the **P3HT** block would operate as the p-type electron donor and the **PNDI-2Th** block would operate as the n-type electron acceptor. Ideal self-assembled nano-structures would be a columnar structure with the columns about 20 nm in diameter. Because the exciton diffusion length is about approximately 10 nm, this would allow every exciton the chance to get to a donor-acceptor interface in order to be split into charge carriers. A couple of different studies could be accomplished with this novel material. A morphology study could investigate the different nanostructures the P-N block copolymer forms when the material is modified and processed under various conditions. An OFET study could investigate the mobility of the polymer and possibly make ambipolar measurements as there is both p-type and n-type in one material. Finally, an organic photovoltaic study could also be attempted. Active layers of these OPVs would only require one material.

8.1.3 Carboxylated polythiophenes in thermoelectrics

The carboxylated polymers **M1, M2,** and **M3** could be investigated in thermoelectric devices. This could be accomplished using the device architecture shown below in Figure 8.2.

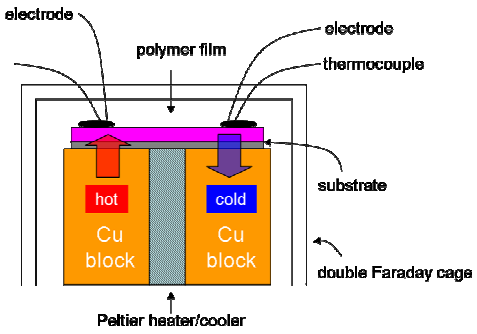

Figure 8.2 Proposed thermoelectric property measurement device. Double Faraday cage is used to prevent stray electric fields from interacting with the measurement.

The Peltier heater/cooler is used to heat one side of a copper block and cool the other side. The polymer film set on top of the block will be in a temperature gradient, hot on one side and cold on the other. The magnitude of this temperature gradient will be in the range of a couple Kelvin. Thermocouples attached to the top of the film will be used to measure the temperature. Electrodes set on either side of the film will measure the voltage difference between hot and cold sides. The ratio of the voltage difference compared to the temperature difference is the Seebeck coefficient ($S = \Delta V/\Delta T$). A double Faraday cage is necessary around the entire device in order to quell stray electric fields which may interfere with the measurements.

The **M1, M2,** and **M3** polymers are not intrinsic conductors. In order to make the films conducting, the polymers need to be doped. In previous work, the most effective doping method has been to use molecular iodine.[146] Once the doped films are constructed, the conductivity of the polymers will be measured with a standard four probe measurement. Using the measured Seebeck coefficient and conductivity, one can

calculate ZT. This is the figure of merit used to access thermoelectric performance, as shown below:

$$ZT = \frac{(S^2\sigma)T}{k}$$ Equation 5.4.1

Because of their thermal instability, typical semiconducting polymers such as P3HT, are not usually characterized at high temperatures. Previous work sought to determine the Seebeck number and thermoelectric properties of P3HT.[146] The **M1**, **M2,** and **M3** polymers are more thermally stable than other polythiophene derivatives; this advantage makes these materials good candidates as thermoelectric materials.

8.1.4 Top gate dielectric layers for device encapsulation

The typical device configuration for OFETs is a stack comprising a doped silicon substrate, a thermally grown oxide dielectric layer, solution deposited organic semiconductor and evaporated source drain electrodes as previously shown in Figure 1.2 The advantages of this fabrication method include compatibility with almost limitless different organic semiconductors and good ohmic contact between the organic semiconductor and the source-drain electrodes. However, OFET device performance is often dependant on the semiconductor/silicon oxide dielectric layer interface. To circumvent this issue, surface treatments as those presented in previous chapters, such as OTS, HMDS, and BCB, are used to treat the dielectric layer prior to depositing the organic semiconductor. Another method used by an increasing number of groups is the top gate architecture as shown in Figure 8.3.

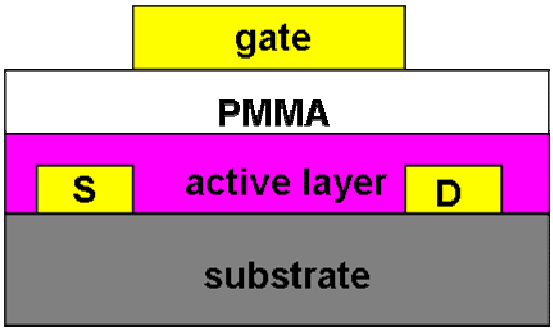

Figure 8.3 Top gate OFET architecture using PMMA as a dielectric layer[147]

Due to the favorable interface characteristics between a spin-coated polymer dielectric and an organic semiconductor active layer, top gate devices often have performance advantage as compared to the conventional bottom-gate architecture (which have an inorganic oxide/organic semiconductor interface). This configuration has been used with both p-type,[147] and n-type[148] semiconductors. A further evolution of this geometry would be not just a top dielectric layer, but the complete encapsulation of the device with the dielectric polymer as has been done in industrial packaging. Following encapsulation, then the gate electrode could be evaporated to form transistors. The dielectric polymer would serve two functions. It would be protected from both air and moisture and provide the capacitive layer necessary for charge accumulation in the organic semiconductor.

9 Experimental section

9.1 Instrumentation

UV-Vis absorption spectra were obtained using a Perkin-Elmer spectrophotometer (Lambda 9 UV/Vis/NIR). FTIR spectra were obtained using a Bruker Vector 33 Fourier transform infrared spectrophotometer equipped to analyze NaCl sample plates. ^{1}H and ^{13}C NMR spectra were obtained on a Bruker AV-300 or AV-500 spectrometer using tetramethylsilane (0.00 ppm) as an internal standard. Mass spectrometer data (HR/LR) was obtained using a JEOL HX-110 mass spectrometer and a Bruker Esquire LC-Ion Trap mass spectrometer. Polymer molecular weights were obtained using a Waters GPC SEC apparatus equipped with a 1515 Isocratic HPLC Pump, a 2487 Dual Absorbance Detector, and a 2414 Refractive Index Detector. Polystyrene GPC standards in THF were used as a reference. X-ray diffraction patterns were obtained on a Bruker AXS D8 Focus diffractometer using an accelerating voltage of 40kV and a Cu-K_{α} source. Thermal transitions were measured by DSC using a Texas Instruments DSC2010 with a heating and cooling rate of 5 °C/min under a constant flow of nitrogen. Cyclic voltammetry was obtained under nitrogen using a BAS CV-50 W voltammetric analyzer with 0.1 M tetra-*n*-butylammonium hexafluorophosphate in anhydrous acetonitrile as supporting electrolyte at a scan rate of 50 mV/s. Platinum wire working and counter electrodes as well as a $Ag/AgNO_3$ reference electrode were used. Ferrocene (Fc/Fc^{+}) was designated as an internal standard for all measurements. The reference energy level used for ferrocene as compared to vacuum was 4.8 eV.

9.2 Experimental - P-type carboxylated polythiophenes

9.2.1 OFET device fabrication and testing

Thin film transistor devices were constructed with active layers made from the polymers. Devices were fabricated on Si/SiO_2 wafers in the top contact geometry using 45-50 nm of gold as the electrodes. All device fabrication for the **M1**, **M2**, and **M3** polymers was performed in air except for the final metal deposition step, which was performed under high vacuum. P3HT devices were fabricated in a nitrogen atmosphere. Both octadecyltrichlorosilane (OTS) and non-OTS treated substrates were tested, but the non-OTS devices yielded better performance for the ester-functionalized polymers. P3HT devices included OTS monolayers.

Heavily doped p-type silicon <100> substrates from Montco Silicon Technologies Inc. with a 300 nm (±5 nm) thermal oxide layer were first cut into 1.5 cm square wafers using a diamond tip stylus. The substrates were labeled, then excess dust was removed with dry nitrogen gas under high pressure. The substrates were rinsed then sonicated for 10 min. with acetone, methanol, and isopropyl alcohol. The wafers were dried under a stream of nitrogen, then subjected to air plasma for 2 min.

The polymer layer was applied by spin casting a solution of the polymer in anhydrous *o*DCB (**M1** 2.5 mg/mL, **M2** 2.0 mg/mL, **M3** 2.0 mg/mL) at 1100 rpm. The **M1** polymer solution was heated to 40 °C and the **M2** and **M3** polymer solutions were heated to 60 °C prior to spin coating to form clear solutions. All solutions were filtered using a 0.2 μm PTFE filter before spin casting. The substrates were heated on a 80 °C hot plate prior to spin coating in order to maintain polymer solubility. OFET devices were annealed in air at 110 °C for 10 minutes.

Inter-digitated source and drain electrodes made of gold (W = 9000 μm, L= 90 μm) with an aspect ratio (W/L) of 100 were deposited on top of the polymer active layer by evaporating a 50 nm thick gold film at 0.5 Å/s through a shadow mask from a resistively heated Mo boat under high vacuum (2.0×10^{-6} torr). The devices were tested in air as p-type OFETs using an Agilent 4155B semiconductor parameter analyzer. Further device testing was conducted one month after fabrication. During storage, the devices were kept in air and protected from light. The source, drain and gate electrodes of the OFET devices were connected to the parameter analyzer using thin pin electrodes. Two test types were conducted with each device, a transfer curve and a set of family curves. Family curves were obtained by measuring the drain current of the transistor compared to the source-drain voltage at different discrete gate voltages. Transfer curves were obtained by measuring the source-drain current while varying the gate voltage at a constant source-drain voltage. At least 6 devices were fabricated using each polymer and the average mobility is presented.

9.2.2 Synthesis

2,5-Bis(trimethylstannyl)thiophene,[149] **5,5"-bis(trimethylstannyl)-2,2':5',2"-terthiophene**,[52] and **2-bromothiophene-4-carboxylic acid**[150] were prepared using literature procedures.

Dodecyl 2-bromothiophene-4-carboxylate. To 2-bromothiophene-4-carboxylic acid (8.56 g, 41.3 mmol) was added $SOCl_2$ (100 mL). The mixture was heated at reflux under nitrogen for 12 h. The solvent was removed by distillation, then by high vacuum. To this was added $C_{12}H_{25}OH$ (19.4 g, 0.10 mol) dissolved in pyridine (15 mL). The

reaction was stirred under nitrogen at 80 °C for 12 h. The product mixture was poured into 1 M HCl (300 mL) in an ice slurry, then extracted with ether, followed by washing with sat. $NaHCO_3$ then brine. After the solvent was removed, the product mixture was separated by silica gel chromatography using 1:50 ethyl acetate/hexane as solvent. The solvent was removed, and the product was dried to afford a clear colorless oil (6.71 g, 43% yield). ^{1}H NMR (300 MHz, $CDCl_3$, δ): 8.00 (d, 1H), 7.48 (d, 1H), 4.27 (t, 2H), 1.74 (m, 2H), 1.24-1.43 (m, 18H), 0.90 (t, 3H). ^{13}C NMR (500 MHz, $CDCl_3$, δ) 165.6, 138.3, 138.0, 134.3, 116.8, 81.1, 69.0, 35.9, 33.6, 33.3, 32.7, 10.0, 26.7, 18.12. MS (EI) m/z: 374.1 (M^+)

Didodecyl 2,2'-bithiophene-4,4'-dicarboxylate. To a mixture of dodecyl 2-bromothiophene-4-carboxylate (7.51 g, 20.0 mmol) in THF cooled to 0 °C, was added 2M *i*PrMgCl in THF (5 mL, 10 mmol). The mixture was stirred under nitrogen for 1 h. A yellow to dark red color change was observed. The reaction mixture was warmed to room temperature and Ni(dppp)Cl_2 (59 mg, 0.1 mmol) catayst was added. The mixture was headed to 40 °C and stirred for 36 h. The product mixture was filtered to remove the catayst, extracted with chloroform, then washed with sat. $NaHCO_3$ and brine. $MgSO_4$ was added to remove any residual water, and filtered off. The product was separated by silica gel chromatography using 200:1 hexane/ethyl acetate as solvent. The solvent was removed, and the product was dried to give a white crystalline solid (0.79 g, 13% yield). Mp 196 °C. ^{1}H NMR (300 MHz, $CDCl_3$, δ): 8.02 (d, 2H), 7.60 (d, 2H), 4.30 (t, 4H), 1.77 (m, 4H), 1.21-1.48 (m, 36H), 0.90 (t, 6H). ^{13}C NMR (500 MHz, $CDCl_3$, δ) 166.4, 140.9,

138.6, 135.7, 128.6, 69.1, 35.92, 33.7, 33.6, 33.5, 33.4, 33.3, 32.7, 10.0, 26.7, 18.12. (EI) m/z: 590.3 (M^+)

Didodecyl 5,5'-dibromo-2,2'-bithiophene-4,4'-dicarboxylate. To a 3-neck flask attached to a condenser under nitrogen was added didodecyl 2,2'-bithiophene-4,4'-dicarboxylate (0.69 g, 1.1 mmol) dissolved in 20 mL of chloroform. To this was added Br_2 (0.55 g, 3 mmol) in chloroform (20 mL) dropwise. The brownish red solution was stirred at 0 °C for 30 min. The temperature was increased to 60 °C, and the reaction stirred for 12 h. The resulting red solution was poured into 250 mL of 0 °C DI H_2O/ice. 20 mL of 10% Na_2SO_3 was added to remove the Br_2. The product was extracted with $CHCl_3$, washed with brine, then dried with $MgSO_4$. The solvent was removed under reduced pressure resulting in a waxy white solid (0.29 g 33% yield). ^{1}H NMR (300 MHz, $CDCl_3$, δ): 7.3 (s, 2H), 4.30 (t, 4H), 1.75 (m, 4H), 1.21-1.31 (m, 36H), 0.88 (t, 6H). The NMR matches with literature values.[28]

Poly(didodecyl 2,2'-bithiophene-4,4'-dicarboxylate-co-thiophene (M1). A mixture of didodecyl 5,5'-dibromo-2,2'-bithiophene-4,4'-dicarboxylate (97 mg, 0.13 mmol) and 2,5-bis(trimethylstannyl)-thiophene (53 mg, 0.13 mmol)**,** dry toluene (15 mL) and DMF (3.7 mL) was added to a 50 mL three neck flask equipped with a condenser and hooked up to nitrogen. $Pd(PPh_3)_4$ (7.5 mg, 0.5 mol%) in dry toluene (5 mL), prepared under nitrogen, was added to this mixture. The reactants were heated to 110 °C and stirred for 24 h. The solution was cooled to room temperature and poured into 50 mL of methanol. The precipitate was vacuum filtered using a fine pore ceramic frit, and dried.

The dark purple solid was Soxhlet-extracted using DCM for 24 h. The resulting DCM solution was cooled to room temperature, and poured into methanol (100 mL). The dark purple precipitate was vacuum filtered in a fine ceramic mesh frit, then dried under high vacuum to remove any excess solvent. The product was dried under high vacuum, resulting in dark purple polymer (79 mg, 88% yield). ^{1}H NMR (500 MHz, *o*DCB *d*4, 50 ºC): 7.74 (s, 2H), 7.69 (s, 2H), 7.28 (s, 1H), 7.02 (s, 1H), 4.42 (s, 4H), 1.84 (br s, 4H) 1.25-1.51 (m, 36H), 0.95 (s, 6H). M_n = 7100 Da, PDI = 1.6.

Poly(didodecyl 2,2'-bithiophene-4,4'-dicarboxylate-*co*-2,2-bithiophene (M2). was prepared using a modified literature procedure.[28] A mixture of didodecyl 5,5'-dibromo-2,2'-bithiophene-4,4'-dicarboxylate (96 mg, 0.13 mmol) and 5,5'-bis(trimethylstannyl)-2,2'-bithiophene (63 mg, 0.13 mmol)**,** dry toluene (15 mL) and DMF (3.7 mL) was added to a 50 mL three neck flask equipped with a condenser and hooked up to nitrogen. $Pd(PPh_3)_4$ (7.5 mg, 0.5 mol%) in dry toluene (5 mL), prepared under nitrogen, was added to this mixture. The reactants were heated to 110 °C and stirred for 24 h. The solution was cooled to room temperature and poured into methanol (50 mL). The precipitate was vacuum filtered using a fine pore ceramic frit, and dried. The dark purple solid was Soxhlet-extracted using DCM for 24 h. The product was dried under high vacuum resulting in a dark purple polymer (50.2 mg, 51% yield). ^{1}H NMR (500 MHz, *o*DCB *d*4, 50 ºC): 7.66 (s, 2H), 7.28 (s, 2H), 7.02 (s, 2H), 4.45 (s, 4H), 1.87 (br s, 4H) 1.25-1.51 (m, 36H), 0.95 (s, 6H). M_n = 6700 Da, PDI = 1.9. The NMR matches with literature values.[28]

Poly(didodecyl 2,2'-bithiophene-4,4'-dicarboxylate-co-2,2':4",2'-terthiophene (M3). A mixture of didodecyl 5,5'-dibromo-2,2'-bithiophene-4,4'-dicarboxylate (95 mg, 0.13 mmol) and 2,5-Bis(trimethylstannyl)-thiophene (73 mg, 0.13 mmol)**,** 15 mL dry toluene (15 mL) and DMF (3.7 mL) was added to a 50 mL three neck flask equipped with a condenser and hooked up to nitrogen. $Pd(PPh_3)_4$ (7.5 mg, 0.5 mol%) in dry toluene (5 mL), prepared under nitrogen, was added to this mixture. The reactants were heated to 110 °C and stirred for 24 hours. The solution was cooled to room temperature and poured into 50 methanol (50 mL). The precipitate was vacuum filtered using a fine pore ceramic frit, and dried. The dark purple crystalline solid was Soxhlet-extracted using DCM for 24 h. The resulting chloroform solution was cooled to room temperature, and poured into methanol (100 mL). The dark purple precipitate was vacuum filtered in a fine ceramic mesh frit, then dried under high vacuum to remove any excess solvent to produce a dark purple polymer (65 mg, 60% yield). ^{1}H NMR (500 MHz, *o*DCB *d*4, 50 ºC): 7.67 (s, 2H), 7.30 (s, 2H), 7.10 (s, 4H), 4.46 (s, 4H), 1.87 (br s, 4H) 1.19-1.59 (m, 36H), 0.95 (s, 6H). M_n = 5100 Da, PDI = 1.2.

9.3 Experimental - PNDI n-type thiophene copolymers

9.3.1 OFET device fabrication and testing

Organic field-effect transistors were fabricated as typical top-contact bottom-gate devices on silicon substrates. Heavily doped p-type silicon <100> substrates from Montco Silicon Technologies Inc. with a 500 nm (±5 nm) thermal oxide layer acted as a common gate with a dielectric layer (C_i = 1.10 × 10^{-8} F/cm^2) as well as the substrate. After cleaning the

substrates by sequential ultrasonication in acetone, methanol, and isopropyl alcohol for 10 minutes, the substrates were treated by air plasma prior to forming a self-assembled monolayer of octadecyltrichlorosilane (OTS) via vapor deposition. The substrates were then washed with chloroform and isopropyl alcohol to remove physisorbed silane agents. Polymer thin films were deposited from a 5 mg/mL chloroform:*o*DCB solution (98:2) by spin-coating (1000 rpm for 60 s). The devices were thermally annealed with varying temperature lengths to optimize device performance. The **PNDI-0Th**, **PNDI-1Th**, and **PNDI-3Th** polymers were all annealed at 150 °C; the **PNDI-2Th** polymer was annealed at 110 °C. Interdigitated source and drain electrodes (W = 9000 μm, L = 90 μm) made of gold (50 nm thick) were deposited on top of the polymer active layer by thermo evaporation at 1.0 Å/s through a shadow mask from a resistively heated Mo boat under high vacuum (5.0×10^{-7} torr). A HP4145B semiconductor parameter analyzer controlled by locally written LabView codes through a GPIB interface was used for OFET device characterization. Transfer curves were fitted in the saturation regiem for mobility calculations. All device fabrication and electrical characterization were performed in a nitrogen atmosphere.

9.3.2 Synthesis

All reagents used for synthesis were obtained from Sigma Aldrich and were used as-is without further purification with the exception of the two catalysts: $Ni(COD)_2$ and $Pd(PPh_3)_2Cl_2$, which were obtained from Strem Chemicals. The monomers used to synthesize the four NDI-polymers were synthesized using standard literature procedures—specifically, NDI-Br_2,[13, 41, 48, 51] and the stannylated thiophenes, **1**,**2** and **3**.[41, 52]

Synthesis of PNDI-0Th: To an air-free schlenk flask, $Ni(COD)_2$ (0.179 g, 0.65 mmol), 2,2'-bipyridine (0.064 g, 0.41 mmol), and COD (0.07 g, 0.65 mmol) were added within a dry glove box and dissolved with toluene (1.5 mL) and DMF (0.35 mL). The capped and sealed vessel was heated to 80 °C for 30 minutes prior to injecting a solution of NDI-Br_2 (0.2 g, 0.28 mmol) in toluene (1.5 mL). The reaction was heated at 80 °C for 6 days. The reaction was cooled to ambient and quenched with 2 N HCl (2 mL) and stirred for 15 minutes. Chloroform was added (25 mL) and extracted. The organic layer was washed twice with 2 N HCl (20 mL). The aqueous layers were combined and extracted twice with chloroform. The organics were combined and stirred with a saturated Na_4EDTA solution (10 mL) for 12 hours. The organics were washed with water, dried over $MgSO_4$, and filtered over a pad of silica. The solution was concentrated and precipitated to methanol. The precipitated polymer was subjected to a Soxhlet extraction with acetone to remove low-molecular weight polymer fragments. The polymer was redissolved in chloroform and precipitated into methanol to yield a fibrous yellow solid (70%). ^1H (300 MHz, $CDCl_3$): 8.65 (br s, 2H), 3.98 (br, 4H), 1.91 (m, 2H), 1.24 (m, 64H), 0.86 (m, 12H).

General synthesis for PNDI-n-Th: To an air-free schlenk flask, $Pd(PPh_3)_2Cl_2$ (0.005 mmol), NDI-Br_2 (0.10 mmol), and **1**,[8] **2**,[8] or **3**[21] (0.10 mmol) were added within a dry glove box and dissolved with toluene (5 mL). The capped and sealed vessel was heated at 90 °C for 4 days prior to injecting bromobenzene (0.2 mL) and stirring for 12 hours. The reaction was cooled to ambient and KCl (1 g) in water (2 mL) was injected and stirred for 2 hours. The solution was extracted with chloroform (2 × 60 mL). The

combined organics were washed with water (2 × 50 mL) and dried over Na_2SO_4. The solution was concentrated by vacuum and precipitated into methanol. The precipitated polymer was subjected to a Soxhlet extraction with acetone for 48 hours to remove low-molecular weight polymer fragments. The polymer was redissolved in chloroform, precipitated into methanol, and dried under reduced pressure. See Table 1 for further polymer data. **PNDI-1Th:** Dark blue solid (87%). ^{1}H (300 MHz, $CDCl_3$): 8.97 (br s, 2H), 7.45 (br, 2H), 4.14 (br, 4H), 2.02 (m, 2H), 1.10-1.45 (m, 64H), 0.83 (m, 12H). **PNDI-2Th:** Dark blue solid (95%). ^{1}H (300 MHz, $CDCl_3$): 8.80 (br s, 2H), 7.33 (br, 4H), 4.11 (br, 4H), 2.04 (m, 2H), 1.07-1.54 (m, 64H), 0.86 (m, 12H). **PNDI-3Th:** Dark green solid (97%). ^{1}H (300 MHz, $CDCl_3$): 8.80 (br s, 2H), 7.32 (br, 6H), 4.10 (br, 4H), 1.97 (m, 2H), 1.08-1.60 (m, 64H), 0.87 (m, 12H).

9.4 Experimental - Ladderized n-type naphthalene bisimide copolymers

9.4.1 DFT calculations

Density functional theory (DFT) calculations were performed using the Gaussian 03 software package using the B3LYP calculation method and 6-31G basis set.[151-153] Geometry optimization followed by frequency calculation was performed to obtain the lowest energy conformations.

9.4.2 OFET device fabrication and testing

Thin film transistors were fabricated as typical top-contact bottom-gate devices on silicon substrates. Heavily doped p-type silicon <100> substrates from Montco Silicon

Technologies Inc. with a 300 nm (±5 nm) thermal oxide layer acted as common gate, dielectric layer, and substrate. The substrates were cleaned by sequential ultrasonication in acetone, methanol, and isopropyl alcohol for 10 min followed by an air plasma treatment. The optimized conditions used for obtaining the electron mobility measurements are as follows: polymer thin films were deposited from a filtered 5 mg/mL chlorobenzene solution by spin-coating at 1000 rpm for 60 s (octadecyltrichlorosilane (OTS) treated substrates were also tested, but yielded poor performance compared to devices fabricated on bare oxide layer substrates). The devices were dried on a temperature-controlled hot-plate at 150 °C for 10 min under nitrogen atmosphere. Interdigitated source and drain electrodes (W = 9000 μm, L = 90 μm) made of gold (50 nm thick) were deposited through shadow masks on top of the polymer active layer by thermo evaporation at 1.0 Å/s by a resistively heated Mo boat under high vacuum (5.0×10^{-7} Torr). At least four devices were fabricated to obtain average electron mobilities.

9.4.3 Synthesis

All reagents used for synthesis were obtained from Sigma-Aldrich and were used as-is without further purification with the exception of the catalyst, $Pd(PPh_3)_2Cl_2$, which was obtained from Strem Chemicals. The monomers used to synthesize the NDI-polymers were synthesized using standard literature procedures—specifically, NDI–Br_2,[41, 48, 51, 154] and the stannylated phenyl monomers; **1**[155] and **3**.[63]

N-(2,5-dibromophenyl),1-dimethylethyl ester carbamic acid (2c). To a 100 mL air-free Schlenk flask, 2,5-dibromobenzoic acid (**2a**) (2.5 g, 8.9 mmol) was added to 30 mL

of toluene followed by oxalyl chloride (1.7 g, 13.4 mmol) and a catalytic amount of DMF (1 drop). The solution was heated at reflux for 2 h. The gold-colored clear reaction solution was cooled to room temperature to provide a yellow residue (**2b**) after the solvent was removed under reduced pressure, which was not isolated. The residue was dissolved in dry dichloromethane (14 mL) and added dropwise to a solution of saturated (6.4 M) sodium azide (7 mL), ^{t}BuNH$_4$Br (4.1 mg), and dichloromethane (3.5 mL) at −5 °C over 1.5 h. The biphasic mixture was stirred for 10 min after the addition was complete. The organic phase was separated and the aqueous phase was extracted with cold dichloromethane (2 × 20 mL). The organic phases were combined and washed with cold water (2 × 30 mL). The solution was then dried over $MgSO_4$ at 0 °C and filtered over a mixture of Celite and $MgSO_4$. The filtrate was subsequently dried over CaH_2 at 0 °C for 40 min. The mixture was filtered again through a pad of Celite and $MgSO_4$. The light yellow filtrate was added to ^{t}BuOH (15 mL) and heated at reflux overnight. The cloudy-white solution was cooled to room temperature and the solvent removed under reduced pressure to provide an off-white solid. The residue was purified via flash chromatography using a mixture of ethyl acetate and hexane (1:4) as eluent. **2c** was isolated as a white solid (2.4 g, 77%). ^{1}H (300 MHz, $CDCl_3$): δ 8.32 (d, 1H), 7.26 (d, 1H), 6.94 (dd, 1H), 6.92 (s, 1H), 1.46 (s, 9H). ^{13}C (75 MHz, $CDCl_3$): δ 151.9, 137.4, 133.1, 126.6, 122.5, 122.0, 110.5, 81.6, 28.2 (3). HRMS-FAB^{+} (*m*/*z*): calcd for $C_{11}H_{13}O_2NBr_2$, 350.92947; found, 350.92859; *m*/*z* 351 (14%), 296 (39%), 251 (16%), 165 (8%), 154 (100%), 107 (32%).

N-(*tert*-Butoxycarbonyl)-1-amino-2,5-bis(trimethylstannyl)benzene (2). A 50 mL air-free Schlenk flask was charged with **2c** (1.1 g, 3.1 mmol) in diethyl ether (20 mL) at −78 °C. 1.6 M MeLi (2.05 mL, 3.3 mmol) was added to the solution dropwise and allowed to stir for 10 min at −78 °C. The solution was allowed to warm to 0 °C. The yellow solution was slowly transferred via cannula to a 100 mL air-free Schlenk flask containing 1.7 M ^{t}BuLi (6.08 mL, 10.3 mmol) in diethyl ether (7 mL) at −78 °C. The mixture was stirred for 4 h at −78 °C before allowing the reaction to slowly warm to 0 °C. The dark orange slurry was recooled to −78 °C before adding 1 M trimethyltin chloride (8.33 mL, 8.33 mmol). The light clear orange solution was allowed to warm to 0 °C before quenching with water (20 mL). The organics were separated and the aqueous phase was extracted with diethyl ether (2 × 20 mL). The organics were combined and washed with water (2 × 30 mL) and brine (30 mL). The isolated organics were dried over Na_2SO_4, filtered, and the solvent removed under reduced pressure to produce a red-orange oil. The residue was purified via flash chromatography by eluting through basic silica (treated with 9:1 hexane:triethylamine) using hexane as eluent. **2** was isolated as a white crystalline solid (0.31 g, 19%). ^{1}H (300 MHz, $CDCl_3$): 7.56 (s, 1H), 7.39 (d, 1H), 7.25 (d, 1H), 6.24 (s, 1H), 1.50 (s, 9H), 0.32 (s, 9H), 0.28 (s, 9H). ^{13}C (75 MHz, $CDCl_3$): δ 153.93, 143.68, 142.82, 136.42, 136.03, 132.23, 130.53, 80.28, 28.44 (3), −8.55 (3), −9.49 (3). MS/EI: *m*/*z* 540 (Na^+), 504 (17%), 448 (100%), 400 (10%), 286 (15%), 165 (46%), 135 (10%).

General synthesis for PNDI-xBoc: To an air-free Schlenk flask, $Pd(PPh_3)_2Cl_2$ (0.005 mmol), NDI–Br_2 (0.10 mmol), and **1**,[155] **2**, or **3** [63] (0.10 mmol) were added within a dry glovebox and dissolved with toluene (5 mL). The capped and sealed vessel was heated at

90 °C for 4 days prior to injecting bromobenzene (0.2 mL) and stirring for 12 h. The reaction was cooled to ambient and KF (1 g) in water (2 mL) was injected and stirred for 2 h. The solution was extracted with chloroform (2 × 60 mL). The combined organics were washed with water (2 × 50 mL) and dried over Na_2SO_4. The solution was concentrated by vacuum and precipitated into methanol. The precipitated polymer was subjected to a Soxhlet extraction with acetone and methanol for 48 h to remove low-molecular weight polymer fragments. The polymer was redissolved in chloroform, precipitated into methanol, and dried under reduced pressure. **PNDI-0Boc**: orange solid (87%). ^{1}H (300 MHz, $CDCl_3$): 8.89 (br, 2H), 7.58 (br, 4H), 4.11 (br, 4H), 2.01 (m, 2H), 1.03–1.49 (m, 64H), 0.84 (m, 12H). ^{13}C (300 MHz, $CDCl_3$): 163–162, 147, 140, 136, 129–128, 128–125, 124–123, 45, 37–36, 32, 31, 30–29, 26, 23–22, 14. **PNDI-1Boc**: red solid (74%). ^{1}H (500 MHz, $CDCl_3$): 8.90 (br, 2H), 8.26 (br, 1H), 7.92–7.51 (br, 1H), 7.30 (br, 1H), 6.12 (br, 1H), 4.15 (br, 4H), 2.04 (m, 2H), 0.97–1.73 (m, 73H), 0.86 (m, 12H). ^{13}C (125 MHz, $CDCl_3$): 163–162, 153–152, 147, 144, 141, 137–134, 129–123, 81–80, 45, 37–36, 32–31, 31–29, 29–28, 27–26, 23–22, 14. **PNDI-2Boc**: brown-red solid (76%). ^{1}H (500 MHz, $CDCl_3$): 8.91 (br, 2H), 7.99 (br, 2H), 6.03 (br, 2H), 4.16 (br, 4H), 2.03 (m, 2H), 0.99–1.61 (m, 82H), 0.85 (m, 12H). ^{13}C (125 MHz, $CDCl_3$): 164–160, 154–152, 144–143, 141, 139–136, 134–130, 129–123, 122–119, 81–80, 45, 37–36, 32–31, 31–29, 29–27, 27–26, 23–22, 14.

General ladderization treatment generating PNDI-xBocL: Literature procedures were adapted to form the ladder polymers.[63] To a single-neck round-bottom flask, **PNDI-*x*Boc** (0.1 mmol) was dissolved in dichloromethane (5–10 mL). Trifluoroacetic acid (3–4 mL)

and anisole (0.5 mL) were added and the mixture was heated at reflux overnight. The reaction solution was subsequently cooled to room temperature and the solution was carefully and slowly added to a mixed solvent of triethylamine (10 mL) and acetone (100 mL). The precipitate was collected by filtration and then dissolved in triethylamine (5 mL). The solution was heated in a screw-cap vial at 80 °C overnight. The solution was then cooled to room temperature, precipitated in acetone, and filtered. The solids were washed with acetone and dried to yield the final ladderized polymer product. **PNDI-1BocL**: red solid (74%). ^{1}H (500 MHz, $CDCl_3$): 9.74–10.50 (br, 2H), 7.83–9.53 (br, 3H), 3.79–4.52 (br, 4H), 1.88–2.52 (m, 2H), 0.95–1.79 (m, 64H), 0.84 (m, 12H). ^{13}C (125 MHz, $CDCl_3$): 165–160, 150–140, 138–134, 130–120, 110, 45, 37–36, 32–31, 31–29, 27–26, 23–22, 14. **PNDI-2BocL**: violet-black solid (93%). ^{1}H (500 MHz, $CDCl_3$): 9.63–10.50 (br, 1H), 9.24 (br, 2H), 7.04–8.76 (br, 1H), 5.23 (br, 4H), 2.37 (m, 2H), 1.04–2.25 (m, 64H), 0.87 (m, 12H). ^{13}C (125 MHz, $CDCl_3$): 165–158, 151–146, 145–137, 135–117, 115–106, 45, 37–35, 32–31, 31–29, 29–27, 27–26, 23–22, 14.

9.5 Experimental - All-polymer blends for organic solar cells

9.5.1 Spectroscopic methods

Photoluminecence (PL) and photo-induced absorption (PIA) spectra were measured simultaneously using standard lock-in techniques.[88] A 455 nm LED was electronically modulated by an Agilent 33120A Arbitrary Waveform Generator and a home-built driver circuit and was used to optically pump the sample while the change in transmitted light induced by the pump was probed with a monochromated tungsten lamp. A Si/InGaAs

photodetector with sensitivity from the visible to the near-IR coupled with an SR830 lock-in amplifier was used to detect these changes, which are reported as dT/T values. The phase of the lock-in was set such that polymer PL or scattered LED pump light appeared entirely as a positive signal in the X-channel. Thus, a fast absorption induced by the pump appears as a negative dT/T signal in the X-channel. Corrections were made to subtract any film PL or scattered pump light from the PIA spectra.

Fluorescence decays of the blend thin films were obtained using the time-correlated single photon counting (TCSPC) technique on a PicoQuant FluoTime 100 spectrometer equipped with a PicoHarp 300 TCSPC module. The instrument utilizes a fast Hamamatsu (model PMA 182-N) photomultiplier tube as the detector and a 470 nm pulsed diode laser (LDH-P-C-470, PicoQuant) as the excitation source. The decay curves were analyzed using the FluoFit software package provided by PicoQuant. All measurements were done at room temperature under N_2 flow.

9.5.2 Spectroelectrochemistry

Films of **PNDI-1Th** and **PNDI-2Th** were deposited onto cleaned fluorine doped tin oxide (FTO) slides (Hartford Glass, 20 × 6 mm). Prior to polymer deposition the conductive surfaces of the FTO were treated with 3-mercaptopropyl-trimethoxysilane while heating at 70 ˚C for 5 minutes, rinsed with chloroform to remove excess silane, then cured at 120 ˚C for 30 minutes. The treated FTO was then masked to a 6 × 6 mm^2 area, and the polymers were drop-coated from chloroform. After drying, the mask was removed and the films were inserted into a cuvette containing a 0.1 M solution of tetrabutylammonium hexafluorophosphate in acetonitrile with a silver quasi-reference electrode (calibrated to the ferrocene/ferrocenium redox couple) and a platinum counter

electrode. The electronic absorption spectra as a function of electrochemical potential were collected on a Cary 500 (Varian) spectrophotometer and a μ-autolab II potentiostat was used to control the potential.

9.5.3 OPV fabrication and testing

ITO-coated glass substrates (15 Ω/□, supplied by Colorado Concept Coatings) were cleaned via sequential ultrasonication in a mild detergent, deionized water, acetone, and isopropyl alcohol then dried under a stream of nitrogen, then air plasma treated for 5 min under vacuum (200 mTorr). A 40 nm thick PEDOT:PSS (Clevios PVP Al 4083) was spin-coated then dried air at 140 °C for 10 min. Active layer solutions in anhydrous chlorobenze composed of **P3HT** (Rieke Metal, Sepiolid P100) and **PNDI-xTh** polymers (20 mg/mL) were stirred overnight and filtered prior to spin coating. The 220 nm active layers were spin-coated in a nitrogen filled glove box. 100 nm of Al were evaporated under vacuum (5×10^{-7} Torr) through shadow masks to form the electrodes. Finally the devices were annealed at 110 °C for 10 min. The J–V characteristics of OPVs were tested using a Keithley 2400 source measurement unit controlled by locally written labview codes. An Oriel xenon lamp (450 W) coupled with an AM1.5 filter was used, with a light intensity of 100 mW cm^{-2}. Light intensity was calibrated with a standard silicon photodiode with a KG5 filter traceable to the National Renewable Energy Laboratory. All fabrication and testing was performed in a nitrogen filled glove box. At least five devices were made and tested for each polymer. Average values are reported.

9.6 Experimental - Crosslinked and doped PNDI-xTh as ETL in inverted OPV

9.6.1 Fabrication and characterization of OFET devices

Thin film transistors were fabricated as typical top contact, bottom gate devices on silicon substrates. Heavily doped p-type silicon <100> substrates from Montco Silicon Technologies Inc. with a 300 nm (±5 nm) thermal oxide layer acted as a common gate and dielectric layer. After cleaning the substrates by sequential ultrasonication in acetone, methanol, and isopropyl alcohol for 10 min followed by air plasma treatment, a self-assembled monolayer of hexamethyldisilazane (HMDS) was formed by vapor deposition. The substrates were then washed with chloroform and isopropyl alcohol to remove physisorbed silane agents. Polymer thin films were deposited from a 0.5 wt% chlorobenzene solution by spin-coating (2000 rpm for 30 s). Additional solutions contained 10 wt% of crosslinker, and 5, 10, and 15 wt% of the dopant. Selected substrates were submitted to a UV crosslinking treatment (λ = 254 nm) for 6 min. Thermal annealing was performed at 110 °C on a hot-plate for 10 min under nitrogen atmosphere. Inter-digitated source and drain electrodes (W = 9000 μm, L = 90 μm) made of gold (50 nm thick) were deposited on top of the active layers by thermal evaporation at 1.0 Å/s through a shadow mask from a resistively heated Mo boat under high vacuum (5.0×10^{-7} torr). A HP4145B semiconductor parameter analyzer controlled by locally written LabView codes through a GPIB interface was used for characterization. All device characterization was performed in a nitrogen atmosphere.

9.6.2 Fabrication and characterization of inverted OPVs:

To fabricate the inverted OPVs, ITO glass substrates resistance were cleaned with de-ionized water, acetone, and isopropyl alcohol, and then treated with oxygen plasma. Polymer thin films (x-PNDI-nTh (0-15%)) were deposited from a 0.5 wt% chlorobenzene solution by spin-coating (4000 rpm for 30s). Polymer solutions contained 10 wt% of crosslinker, and 5, 10, and 15 wt% of the dopant. The substrates were submitted to a thermal annealing (150 °C for 10 min) and a UV crosslinking (λ = 254 nm, 6 min) under nitrogen atmosphere. Afterward, a chlorobenzene solution (60 mg/mL) of **PCBM** (American Dye Source, Inc., 99.0% purity) and P3HT (Rieke Metals, Inc., 4002-E grade) (0.7:1 weight ratio) was spin-coated on the electron transporting layer and annealed at 160 °C for 10 min. After annealing, a PEDOT:PSS solution (H. C. Starck, Clevios 4083) was spin-coated onto the active layer, and then the devices were annealed for 10 min at 120 °C. A metal electrode (100 nm Ag) was then vacuum-deposited through shadow masks at a rate of 2 Å/s. The J–V characteristics of OPVs were tested using a Keithley 2400 source measurement unit controlled by locally written labview codes. An Oriel xenon lamp (450 W) coupled with an AM1.5 filter was used, with a light intensity of 100 mW cm^{-2}. Light intensity was calibrated with a standard silicon photodiode with a KG5 filter traceable to the National Renewable Energy Laboratory. All fabrication and testing was performed in a nitrogen filled glove box.

9.7 Experimental - Fused thiophene NDI copolymers

9.7.1 Synthesis

Thieno[3,2-b]thiophene, **thieno[3,2-b]thieno[2’,3’-d]thiophene**, **3,7-didecanyl thieno[3,2-b]thieno[2',3':4,5]thieno[2,3-d]thiophene**[156] and the corresponding NDI monomer[61] were synthesized according to reference procedures.

5,5’-bis(methylstannyl)-thieno[3,2-b]thiophene. n-Butyl lithium (2.5 M in hexane) (4.5 mL, 11.3 mmol) was added dropwise at -78 ºC to thieno[3,2-b]thiophene (700 mg, 5 mmol) in THF (20 mL) and stirred at -78 ºC for 1 h, followed by 1 h of stirring at room temperature. After cooling to -78 ºC, trimethyltin chloride (2.4 g, 12 mmol) was added. The mixture was warmed to RT and stirred for 1 h. The reaction was diluted with ethyl acetate (50 mL), washed with H_2O (2 × 20 mL) and brine (2 × 20 mL) then dried over $MgSO_4$. After removal of solvent under reduced pressure, give the product as a colorless oil (1.92, 82%). ^{1}H NMR (400 MHz, $CDCl_3$): δ 7.24 (s, 2H), 0.90 (t, J = 7.0Hz, 18H). ^{13}C NMR (100 MHz, $CDCl_3$): δ 147.83, 140.36, 126.45, 12.21.

5,5’-bis(trimethylstannyl)-thieno[3,2-b]thieno[2’,3’-d]thiophene. (4)

n-Butyl lithium (2.5 M in hexane) (4.5 mL, 11.3 mmol) was added dropwise at -78 ºC to thieno [3,2-b]thieno [2’,3’-d]thiophene (980 mg, 5 mmol) in THF (20 mL) and stirred at -78 ºC for 1 h, then warmed to room temperature and stirred for 1 h. After cooling to -78 ºC, trimethyltin chloride (2.4 g, 12 mmol) was added and the mixture was warmed to r.t. and stirred for 1 h. The reaction was diluted with ethyl acetate (50 mL), washed with H_2O (2 × 20 mL) and brine (2 × 20mL) then dried over $MgSO_4$. After removal of solvent, give

the product as a colorless oil (2.25, 86%). ^{1}H NMR (400 MHz, CDCl3): δ 7.25 (s, 2H), 0.88 (t, J = 7.0Hz, 18H). ^{13}C NMR (100 MHz, $CDCl_3$): δ 143.82, 138.85, 136.24, 128.23, 11.93.

5,5'-bis(trimethylstannyl)-3,7-didecanyl thieno[3,2-b]thieno[2',3':4,5]thieno[2,3-d]thiophene. n-Butyl lithium (2.5 M in hexane) (1.8 mL, 4.5 mmol) was added dropwise at -78 ºC to 3,7-didecanyl thieno[3,2-b]thieno[2',3':4,5]thieno[2,3-d]thiophene (1.07 g, 2 mmol) in THF (10 mL) and stirred at -78 ºC for 1 h, then warmed to room temperature and stirred for 1 h. After cooling to -78 ºC, trimethyltin chloride (1.2 g, 6 mmol) was added and the mixture was warmed to RT and stirred for 1 h. The reaction was diluted with ethyl acetate (30 mL), washed with H_2O (2 x 20 mL) and brine (2 x 20mL) then dried over $MgSO_4$. After removal of solvent, give the product as a colorless oil (1.33, 77%). ^{1}H NMR (400 MHz, CD2Cl2): δ 2.51 (t, 4H), 1.64 (m, 4H), 1.27 (m, 28H), 0.89 (t, 6H). 0.88 (t, J = 7.0Hz, 18H). ^{13}C NMR (100 MHz, $CDCl_3$): δ 141.3, 136.4, 133.2, 132.0, 120.7, 32.3, 30.0, 30.0, 29.9, 29.8, 29.7, 29.0, 23.1, 14.3, 11.93.

General synthetic procedure for PNDI-2fTh, PNDI-3fTh and PNDI-4fTh: All of the polymers were prepared by a similar procedure. To a Schlenk flask was introduced compound **7** (496 mg, 0.5 mmol), corresponding fused thiophene monomer (0.5 mmol), and anhydrous toluene (4 mL). The solution was flushed with nitrogen for 10 min, and then a catalytic amount of tris(dibenzylideneacetone) dipalladium(0) (8.6 mg, 3 mol%) and tri(*o*-tolyl)phosphine (22.9 mg, 15 mol %) was added. After the resulting flask was degassed three times via freeze-pump-thaw cycles, the reactants were heated up to 90 °C

for 24 h. Then the reaction was cooled to room temperature and added into methanol dropwise. The precipitate was collected by filtration and washed by Soxhlet extraction with methanol, acetone, hexane, and chloroform. The chloroform fraction was then concentrated and precipitated into methanol. The solid was filtered and dried under vacuum for 1 day.

Polymer **PNDI-2fTh**: Blue solid; Yield 92%; ^{1}H NMR (400 MHz, CDCl3): δ 8.89 (s, 2H); 7.65 (s. 2H), 4.22 (bs, 4H), 2.07 (bs, 2H), 1.26 (m, 68H), 0.89 (m, 12H). *M*n = 62.5 kDa; PDI = 3.3; M_w = 206.3 kDa

Polymer **PNDI-3fTh**: blue solid; Yield 98%; ^{1}H NMR (300 MHz, $CDCl_3$): δ 8.87 (s, 2H), 7.61 (s, 2H), 4.31 (brs, 4H), 2.13 (brs, 2H), 1.29 (m, 68H), 0.83 (m, 12H). M_n = 21.3 kDa; PDI = 2.9; M_w = 61.8 kDa

Polymer **PNDI-4fTh**: Green solid; Yield 92%; ^{1}H NMR (300 MHz, $CDCl_3$): 8.87 (s, 2H), 4.31 (brs, 4H), 3.53 (br, 4H), 2.13 (brs, 2H), 1.26-1.32 (m, 100H), 0.86, (m, 6H), 0.83 (m, 12H). M_n = 92.4 kDa; PDI = 3.6; M_w = 332.6 kDa.

9.7.2 OFET Device fabrication and testing

Organic field-effect transistors were fabricated as typical top-contact bottom-gate devices on silicon substrates. Heavily doped p-type silicon <100> substrates from Montco Silicon Technologies Inc. with a 300 nm (±5 nm) thermal oxide layer acted as a common gate with a dielectric layer as well as the substrate. After cleaning the substrates by sequential ultrasonication in acetone, methanol, and isopropyl alcohol for 10 minutes, the substrates were treated with a BCB (1% w/w in tolunene spin-cast at 2k rpm) then headed 250 °C overnight in an inert atmosphere. Polymer thin films were spin-cast from a 5 mg/mL

chloroform solution (1200 rpm for 60 s). The devices were thermally annealed with varying temperature lengths to optimize device performance. Source and drain electrodes (with various channel lengths and widths) made of gold (50 nm thick) were deposited on top of the polymer active layer by thermal evaporation at 1.0 Å/s through a shadow mask from a resistively heated Mo boat under high vacuum (5.0×10^{-7} torr). A HP4145B semiconductor parameter analyzer controlled by locally written LabView codes through a GPIB interface was used for OFET device characterization. Transfer curves were fitted in the saturation regime for mobility calculations. All device fabrication and electrical characterization were performed in a nitrogen atmosphere. At least ten devices were fabricated and tested for each polymer. The average values are reported.

9.7.3 OPV fabrication and testing

ITO-coated glass substrates (15 Ω/□, supplied by Colorado Concept Coatings) were cleaned via sequential ultrasonication in a mild detergent, deionized water, acetone, and isopropyl alcohol then dried under a stream of nitrogen, then air plasma treated for 5 min under vacuum (200 mTorr). A 40 nm thick PEDOT:PSS (Clevios PVP Al 4083) was spin-coated then dried air at 140 °C for 10 min. Active layer solutions in anhydrous chloroform composed of **P3HT** (Rieke Metal, Sepiolid P100) and **PNDI-fTh** polymers (20 mg/mL) were stirred overnight and filtered prior to spin coating. Different weight ratios were tested, 2:1 w/w for **PNDI-2fTh**:**P3HT** and **PNDI-3fTh**:**P3HT** and 1:1 w/w for **PNDI-4fTh** yielded the best results. The active layers were spin-coated at 2k rpm in a nitrogen filled glove box. 80 nm of Al were evaporated under vacuum (5×10^{-7} Torr) through shadow masks at 2 Å/sec to form 10 mm^2 electrodes. Finally the devices were annealed at 110 °C for 10 min. box. The J–V characteristics of OPVs were tested using

a Keithley 2400 source measurement unit controlled by locally written labview codes. An Oriel xenon lamp (450 W) coupled with an AM1.5 filter was used, with a light intensity of 100 mW cm^{-2}. Light intensity was calibrated with a standard silicon photodiode with a KG5 filter traceable to the National Renewable Energy Laboratory. All fabrication and was performed in a nitrogen filled glove box. Testing was preformed in air. At least four devices were tested for each polymer with the average values reported.

10 References

1. H. Sirringhaus, N. Tessler and R. H. Friend, *Science*, 1998, **280**, 1741-1744.

2. G. M. Wang, J. Swensen, D. Moses and A. J. Heeger, *J. Appl. Phys.*, 2003, **93**, 6137-6141.

3. I. McCulloch, M. Heeney, C. Bailey, K. Genevicius, I. Macdonald, M. Shkunov, D. Sparrowe, S. Tierney, R. Wagner, W. M. Zhang, M. L. Chabinyc, R. J. Kline, M. D. McGehee and M. F. Toney, *Nat. Mater.*, 2006, **5**, 328-333.

4. C. J. Brabec, N. S. Sariciftci and J. C. Hummelen, *Adv. Funct. Mater.*, 2001, **11**, 15-26.

5. J. Peet, J. Y. Kim, N. E. Coates, W. L. Ma, D. Moses, A. J. Heeger and G. C. Bazan, *Nat. Mater.*, 2007, **6**, 497-500.

6. W. L. Ma, C. Y. Yang, X. Gong, K. Lee and A. J. Heeger, *Adv. Funct. Mater.*, 2005, **15**, 1617-1622.

7. M. Jorgensen, K. Norrman and F. C. Krebs, *Sol. Energy Mater. Sol Cells*, 2008, **92**, 686-714.

8. F. C. Krebs, J. E. Carle, N. Cruys-Bagger, M. Andersen, M. R. Lilliedal, M. A. Hammond and S. Hvidt, *Sol. Energy Mater. Sol Cells*, 2005, **86**, 499-516.

9. M. O. Reese, A. J. Morfa, M. S. White, N. Kopidakis, S. E. Shaheen, G. Rumbles and D. S. Ginley, *Sol. Energy Mater. Sol Cells*, 2008, **92**, 746-752.

10. M. L. Chabinyc, R. A. Street and J. E. Northrup, *Appl. Phys. Lett.*, 2007, **90**.

11. H. Sirringhaus, P. J. Brown, R. H. Friend, M. M. Nielsen, K. Bechgaard, B. M. W. Langeveld-Voss, A. J. H. Spiering, R. A. J. Janssen, E. W. Meijer, P. Herwig and D. M. de Leeuw, *Nature*, 1999, **401**, 685-688.

12. K. Felix Sunjoo, G. Xugang, D. W. Mark and A. J. Samson, *Adv. Mater.*, 2009, **9999**, NA.

13. Z. Chen, Y. Zheng, H. Yan and A. Facchetti, *J. Am. Chem. Soc.*, 2008, **131**, 8-9.

14. R. W. I. de Boer, M. E. Gershenson, A. F. Morpurgo and V. Podzorov, *Phys. Status Solidi A*, 2004, **201**, 1302-1331.

15. H. Y. Chen, J. H. Hou, S. Q. Zhang, Y. Y. Liang, G. W. Yang, Y. Yang, L. P. Yu, Y. Wu and G. Li, *Nat. Photonics*, 2009, **3**, 649-653.

16. A. Babel and S. A. Jenekhe, *J. Am. Chem. Soc.*, 2003, **125**, 13656-13657.

17. J. Zaumseil and H. Sirringhaus, *Chem. Rev.*, 2007, **107**, 1296-1323.

18. G. Dennler, C. Lungenschmied, H. Neugebauer, N. S. Sariciftci and A. Labouret, *J. Mater. Res.*, 2005, **20**, 3224-3233.

19. S. Gunes, H. Neugebauer and N. S. Sariciftci, *Chem. Rev.*, 2007, **107**, 1324-1338.

20. C. Videlot-Ackermann, J. Ackermann, H. Brisset, K. Kawamura, N. Yoshimoto, P. Raynal, A. El Kassmi and F. Fages, *J. Am. Chem. Soc.*, 2005, **127**, 16346-16347.

21. H. K. Tian, J. W. Shi, D. H. Yan, L. X. Wang, Y. H. Geng and F. S. Wang, *Adv. Mater.*, 2006, **18**, 2149-2152.

22. M. O. Ahmed, C. M. Wang, P. Keg, W. Pisula, Y. M. Lam, B. S. Ong, S. C. Ng, Z. K. Chen and S. G. Mhaisalkar, *J. Mater. Chem.*, 2009, **19**, 3449-3456.

23. Y. N. Li, Y. L. Wu, P. Liu, M. Birau, H. L. Pan and B. S. Ong, *Adv. Mater.*, 2006, **18**, 3029-3032.

24. F. Demanze, A. Yassar and F. Garnier, *Macromolecules*, 1996, **29**, 4267-4273.

25. P. Sonar, S. P. Singh, P. Leclere, M. Surin, R. Lazzaroni, T. T. Lin, A. Dodabalapur and A. Sellinger, *J. Mater. Chem.*, 2009, **19**, 3228-3237.

26. Y. Yamaguchi, T. Tanaka, S. Kobayashi, T. Wakamiya, Y. Matsubara and Z.-i. Yoshida, *J. Am. Chem. Soc.*, 2005, **127**, 9332-9333.

27. M. X. Chen, X. Crispin, E. Perzon, M. R. Andersson, T. Pullerits, M. Andersson, O. Inganas and M. Berggren, *Appl. Phys. Lett.*, 2005, **87**.

28. A. R. Murphy, J. S. Liu, C. Luscombe, D. Kavulak, J. M. J. Frechet, R. J. Kline and M. D. McGehee, *Chem. Mat.*, 2005, **17**, 4892-4899.

29. E. J. Meijer, C. Detcheverry, P. J. Baesjou, E. van Veenendaal, D. M. de Leeuw and T. M. Klapwijk, *J. Appl. Phys.*, 2003, **93**, 4831-4835.

30. Z. Bao, A. Dodabalapur and A. J. Lovinger, *Appl. Phys. Lett.*, 1996, **69**, 4108-4110.

31. M. Heeney, C. Bailey, K. Genevicius, M. Shkunov, D. Sparrowe, S. Tierney and I. McCulloch, *J. Am. Chem. Soc.*, 2005, **127**, 1078-1079.

32. Y. F. Li, Y. Cao, J. Gao, D. L. Wang, G. Yu and A. J. Heeger, *Synth. Met.*, 1999, **99**, 243-248.

33. M. Onoda, K. Tada, A. A. Zakhidov and K. Yoshino, *Thin Solid Films*, 1998, **331**, 76-81.

34. R. J. Kline and M. D. McGehee, *Polym. Rev.*, 2006, **46**, 27-45.

35. M. Jaiswal and R. Menon, *Polym. Int.*, 2006, **55**, 1371-1384.

36. B. S. Ong, Y. L. Wu, P. Liu and S. Gardner, *J. Am. Chem. Soc.*, 2004, **126**, 3378-3379.

37. A. R. Murphy and J. M. J. Frechet, *Chem. Rev.*, 2007, **107**, 1066-1096.

38. H. Sirringhaus, P. J. Brown, R. H. Friend, M. M. Nielsen, K. Bechgaard, B. M. W. Langeveld-Voss, A. J. H. Spiering, R. A. J. Janssen and E. W. Meijer, *Synth. Met.*, 2000, **111**, 129-132.

39. A. N. Aleshin, H. Sandberg and H. Stubb, *Synth. Met.*, 2001, **121**, 1449-1450.

40. J. A. Letizia, M. R. Salata, C. M. Tribout, A. Facchetti, M. A. Ratner and T. J. Marks, *J. Am. Chem. Soc.*, 2008, **130**, 9679-9694.

41. X. Guo and M. D. Watson, *Org. Lett.*, 2008, **10**, 5333-5336.

42. S. Huttner, M. Sommer and M. Thelakkat, *Appl. Phys. Lett.*, 2008, **92**, 093302.

43. K. C. See, C. Landis, A. Sarjeant and H. E. Katz, *Chem. Mat.*, 2008, **20**, 3609-3616.

44. B. A. Jones, A. Facchetti, M. R. Wasielewski and T. J. Marks, *J. Am. Chem. Soc.*, 2007, **129**, 15259-15278.

45. M. M. Ling, P. Erk, M. Gomez, M. Koenemann, J. Locklin and Z. N. Bao, *Adv. Mater.*, 2007, **19**, 1123-1127.

46. A. L. Briseno, S. C. B. Mannsfeld, P. J. Shamberger, F. S. Ohuchi, Z. Bao, S. A. Jenekhe and Y. Xia, *Chem. Mat.*, 2008, **20**, 4712-4719.

47. X. Zhan, Z. a. Tan, B. Domercq, Z. An, X. Zhang, S. Barlow, Y. Li, D. Zhu, B. Kippelen and S. R. Marder, *J. Am. Chem. Soc.*, 2007, **129**, 7246-7247.

48. H. Yan, Z. H. Chen, Y. Zheng, C. Newman, J. R. Quinn, F. Dotz, M. Kastler and A. Facchetti, *Nature*, 2009, **457**, 679-U671.

49. B. Crone, A. Dodabalapur, Y. Y. Lin, R. W. Filas, Z. Bao, A. LaDuca, R. Sarpeshkar, H. E. Katz and W. Li, *Nature*, 2000, **403**, 521-523.

50. H. Klauk, U. Zschieschang, J. Pflaum and M. Halik, *Nature*, 2007, **445**, 745-748.

51. G. Koeckelberghs, L. De Cremer, W. Vanormelingen, W. Dehaen, T. Verbiest, A. Persoons and C. Samyn, *Tetrahedron*, 2005, **61**, 687-691.

52. D. E. Seitz, S. H. Lee, R. N. Hanson and J. C. Bottaro, *Synth. Commun.*, 1983, **13**, 121-128.

53. E. Elandaloussi, P. Frere and J. Roncali, *Chem. Commun.*, 1997, 301-302.

54. J. Roncali, *Chem. Rev.*, 1997, **97**, 173-205.

55. S. Huttner, M. Sommer, U. Steiner and M. Thelakkat, *Appl. Phys. Lett.*, 2010, **96**, 073503.

56. B. C. Thompson, Y.-G. Kim, T. D. McCarley and J. R. Reynolds, *J. Am. Chem. Soc.*, 2006, **128**, 12714-12725.

57. N. Blouin, A. Michaud, D. Gendron, S. Wakim, E. Blair, R. Neagu-Plesu, M. Belletete, G. Durocher, Y. Tao and M. Leclerc, *J. Am. Chem. Soc.*, 2007, **130**, 732-742.

58. U. Asawapirom, R. Guntner, M. Forster, T. Farrell and U. Scherf, *Synthesis*, 2002, 1136-1142.

59. S.-M. Kang and Y. Leblebici, *CMOS Integrated Circuits: Analysis and Design*, McGraw-Hill, New York, 1996.

60. Y. Chen, W. Huang, C. Li and Z. Bo, *Macromolecules*, 2010, **43**, 10216-10220.

61. M. M. Durban, P. D. Kazarinoff and C. K. Luscombe, *Macromolecules*, 2010, **43**, 6348-6352.

62. M. M. Durban, P. D. Kazarinoff, Y. Segawa and C. K. Luscombe, *Macromolecules*, 2011, **44**, 4721-4728.

63. Y. Yao and J. M. Tour, *Macromolecules*, 1999, **32**, 2455-2461.

64. K. Bourzac, in *Technology Review*, 2012.

65. S. C. Price, A. C. Stuart, L. Yang, H. Zhou and W. You, *J. Am. Chem. Soc.*, **133**, 4625-4631.

66. E. J. Zhou, J. Z. Cong, Q. S. Wei, K. Tajima, C. H. Yang and K. Hashimoto, *Angew. Chem.-Int. Edit.*, 2011, **50**, 2799-2803.

67. Y. Bao, C. C. Liu, S. Lu, J. K. Xu, F. X. Jiang, Y. Z. Li and Z. Zhang, *Chin. Phys. Lett.*, 2010, **27**, 057201.

68. J. Yang, R. Zhu, Z. Hong, Y. He, A. Kumar, Y. Li and Y. Yang, *Adv. Mater.*, 2011, **23**, 3465-3470.

69. Y. Sun, C. J. Takacs, S. R. Cowan, J. H. Seo, X. Gong, A. Roy and A. J. Heeger, *Adv. Mater.*, **23**, 2226-2230.

70. T. J. Savenije, J. E. Kroeze, X. Yang and J. Loos, *Adv. Funct. Mater.*, 2005, **15**, 1260-1266.

71. M. M. Wienk, J. M. Kroon, W. J. H. Verhees, J. Knol, J. C. Hummelen, P. A. van Hal and R. A. J. Janssen, *Angew. Chem.-Int. Edit.*, 2003, **42**, 3371-3375.

72. S. H. Park, A. Roy, S. Beaupre, S. Cho, N. Coates, J. S. Moon, D. Moses, M. Leclerc, K. Lee and A. J. Heeger, *Nat Photon*, 2009, **3**, 297-302.

73. M. C. Scharber, M. Koppe, J. Gao, F. Cordella, M. A. Loi, P. Denk, M. Morana, H.-J. Egelhaaf, K. Forberich, G. Dennler, R. Gaudiana, D. Waller, Z. Zhu, X. Shi and C. J. Brabec, *Adv. Mater.*, 2009, **22**, 367-370.

74. E. Verploegen, R. Mondal, C. J. Bettinger, S. Sok, M. F. Toney and Z. Bao, *Adv. Funct. Mater.*, 2010, **20**, 3519-3529.

75. M. M. Alam and S. A. Jenekhe, *Chem. Mater.*, 2004, **16**, 4647.

76. S. A. Jenekhe and S. J. Yi, *Appl. Phys. Lett.*, 2000, **77**, 2635.

77. S. Fabiano, Z. Chen, S. Vahedi, A. Facchetti, B. Pignataro and M. A. Loi, *J. Mater. Chem.*, 2011, **21**, 5891-5896.

78. T. J. K. Brenner, I. Hwang, N. C. Greenham and C. R. McNeill, *J. Appl. Phys.*, 2010, **107**, 114501.

79. E. Zhou, J. Cong, Q. Wei, K. Tajima, C. Yang and K. Hashimoto, *Angew. Chem.-Int. Edit.*, 2011, **50**, 2799-2803.

80. C. R. McNeill, A. Abrusci, J. Zaumseil, R. Wilson, M. J. McKiernan, J. H. Burroughes, J. J. M. Halls, N. C. Greenham and R. H. Friend, *Appl. Phys. Lett.*, 2007, **90**, 193506-193503.

81. G. Sang, Y. Zou, Y. Huang, G. Zhao, Y. Yang and Y. Li, *Appl. Phys. Lett.*, 2009, **94**, 193302-193303.

82. V. D. Mihailetchi, J. Wildeman and P. W. M. Blom, *Phys. Rev. Lett.*, 2005, **94**, 126602.

83. M. Granstrom, K. Petritsch, A. C. Arias, A. Lux, M. R. Andersson and R. H. Friend, *Nature*, 1998, **395**, 257-260.

84. R. A. Marsh, C. R. McNeill, A. Abrusci, A. R. Campbell and R. H. Friend, *Nano Lett.*, 2008, **8**, 1393-1398.

85. C. R. McNeill, S. Westenhoff, C. Groves, R. H. Friend and N. C. Greenham, *J. Phys. Chem. C.*, 2007, **111**, 19153-19160.

86. T. Kietzke, H.-H. Horhold and D. Neher, *Chem. Mat.*, 2005, **17**, 6532-6537.

87. Y. Kim, S. Cook, S. A. Choulis, J. Nelson, J. R. Durrant and D. D. C. Bradley, *Chem. Mat.*, 2004, **16**, 4812-4818.

88. D. Veldman, S. C. J. Meskers and R. A. J. Janssen, *Adv. Funct. Mater.*, 2009, **19**, 1939-1948.

89. M. C. Scharber, D. Mühlbacher, M. Koppe, P. Denk, C. Waldauf, A. J. Heeger and C. J. Brabec, *Adv. Mater.*, 2006, **18**, 789-794.

90. J. R. Moore, S. Albert-Seifried, A. Rao, S. Massip, B. Watts, D. J. Morgan, R. H. Friend, C. R. McNeill and H. Sirringhaus, *Adv. Energy Mater.*, 2011, **1**, 230-240.

91. C. Jenny, C. Jui-Fen, C. S. Frank, H. F. Richard and S. Carlos, *Appl. Phys. Lett.*, 2009, **94**, 163306.

92. V. D. Mihailetchi, H. X. Xie, B. de Boer, L. J. A. Koster and P. W. M. Blom, *Adv. Funct. Mater.*, 2006, **16**, 699-708.

93. C. R. McNeill, A. Abrusci, I. Hwang, M. A. Ruderer, P. Müller-Buschbaum and N. C. Greenham, *Adv. Funct. Mater.*, 2009, **19**, 3103-3111.

94. R. Asterbacka, C. P. An, X. M. Jiang and Z. V. Vardeny, *Science*, 2000, **287**, 839-842.

95. K. M. Noone, S. Subramaniyan, Q. Zhang, G. Cao, S. A. Jenekhe and D. S. Ginger, *J. Phys. Chem. C.*, 2011, **115**, 24403-24410.

96. V. D. Mihailetchi, J. K. J. van Duren, P. W. M. Blom, J. C. Hummelen, R. A. J. Janssen, J. M. Kroon, M. T. Rispens, W. J. H. Verhees and M. M. Wienk, *Adv. Funct. Mater.*, 2003, **13**, 43-46.

97. M. Giulianini, E. R. Waclawik, J. M. Bell and N. Motta, *J. Appl. Phys.*, 2010, **108**, 014512.

98. K. Szendrei, D. Jarzab, Z. Chen, A. Facchetti and M. A. Loi, *J. Mater. Chem.*, 2010, **20**, 1317-1321.

99. J. J. M. Halls, C. A. Walsh, N. C. Greenham, E. A. Marseglia, R. H. Friend, S. C. Moratti and A. B. Holmes, *Nature*, 1995, **376**, 498-500.

100. G. Yu, J. Gao, J. C. Hummelen, F. Wudl and A. J. Heeger, *Science*, 1995, **270**, 1789-1791.

101. R. C. Coffin, J. Peet, J. Rogers and G. C. Bazan, *Nat Chem*, 2009, **1**, 657-661.

102. Y. Li and Y. Zou, *Adv. Mater.*, 2008, **20**, 2952-2958.

103. Y. Liang, Y. Wu, D. Feng, S.-T. Tsai, H.-J. Son, G. Li and L. Yu, *J. Am. Chem. Soc.*, 2008, **131**, 56-57.

104. J. Hou, H.-Y. Chen, S. Zhang, G. Li and Y. Yang, *J. Am. Chem. Soc.*, 2008, **130**, 16144-16145.

105. P. A. Troshin, H. Hoppe, J. Renz, M. Egginger, J. Y. Mayorova, A. E. Goryachev, A. S. Peregudov, R. N. Lyubovskaya, G. Gobsch, N. S. Sariciftci and V. F. Razumov, *Adv. Funct. Mater.*, 2009, **19**, 779-788.

106. C. Yang, J. Y. Kim, S. Cho, J. K. Lee, A. J. Heeger and F. Wudl, *J. Am. Chem. Soc.*, 2008, **130**, 6444-6450.

107. Y. He, H.-Y. Chen, J. Hou and Y. Li, *J. Am. Chem. Soc.*, 2010, **132**, 1377-1382.

108. Y. He, G. Zhao, B. Peng and Y. Li, *Adv. Funct. Mater.*, 2010, **20**, 3383-3389.

109. G. Zhao, Y. He and Y. Li, *Adv. Mater.*, 2010, **22**, 4355-4358.

110. M. Jørgensen, K. Norrman and F. C. Krebs, *Sol. Energy Mater. Sol Cells*, 2008, **92**, 686-714.

111. Y. Azahin, S. Alem, R. de Bettignies and J.-M. Nunzi, *Thin Solid Films*, 2005, **476**, 340-343.

112. M. Y. Song, K. J. Kim and D. Y. Kim, *Sol. Energy Mater. Sol Cells*, 2005, **85**, 31-39.

113. A. Watanabe and A. Kasuya, *Thin Solid Films*, 2005, **483**, 358-366.

114. S. K. Hau, H. L. Yip, N. S. Baek, J. Y. Zou, K. O'Malley and A. K. Y. Jen, *Appl. Phys. Lett.*, 2008, **92**.

115. M. S. White, D. C. Olson, S. E. Shaheen, N. Kopidakis and D. S. Ginley, *Appl. Phys. Lett.*, 2006, **89**, 143517.

116. C. Waldauf, M. Morana, P. Denk, P. Schilinsky, K. Coakley, S. A. Choulis and C. J. Brabec, *Appl. Phys. Lett.*, 2006, **89**, 233517.

117. C. S. Kim, S. S. Lee, E. D. Gomez, J. B. Kim and Y.-L. Loo, *Appl. Phys. Lett.*, 2009, **94**, 113302-113303.

118. G. Lakhwani, R. F. H. Roijmans, A. J. Kronemeijer, J. Gilot, R. A. J. Janssen and S. C. J. Meskers, *J. Phys. Chem. C.*, 2010, **114**, 14804-14810.

119. T. Kuwabara, Y. Kawahara, T. Yamaguchi and K. Takahashi, *ACS Appl. Mater. Interfaces*, 2009, **1**, 2107-2110.

120. T. Kuwabara, C. Iwata, T. Yamaguchi and K. Takahashi, *ACS Appl. Mater. Interfaces*, 2010, **2**, 2254-2260.

121. S. K. Hau, Y.-J. Cheng, H.-L. Yip, Y. Zhang, H. Ma and A. K. Y. Jen, *ACS Appl. Mater. Interfaces*, 2010, **2**, 1892-1902.

122. S. K. Hau, H. L. Yip, O. Acton, N. S. Baek, H. Ma and A. K. Y. Jen, *J. Mater. Chem.*, 2008, **18**, 5113-5119.

123. D. A. Rider, B. J. Worfolk, K. D. Harris, A. Lalany, K. Shahbazi, M. D. Fleischauer, M. J. Brett and J. M. Buriak, *Adv. Funct. Mater.*, 2010, **20**, 2404-2415.

124. L. Motiei, Y. Yao, J. Choudhury, H. Yan, T. J. Marks, M. E. v. d. Boom and A. Facchetti, *J. Am. Chem. Soc.*, 2010, **132**, 12528-12530.

125. A. G. Werner, F. Li, K. Harada, M. Pfeiffer, T. Fritz and K. Leo, *Appl. Phys. Lett.*, 2003, **82**, 4495-4497.

126. K. Harada, F. Li, B. Maennig, M. Pfeiffer and K. Leo, *Appl. Phys. Lett.*, 2007, **91**, 092118-092113.

127. A. Nollau, M. Pfeiffer, T. Fritz and K. Leo, *J. Appl. Phys.*, 2000, **87**, 4340-4343.

128. K. Walzer, B. Maennig, M. Pfeiffer and K. Leo, *Chem. Rev.*, 2007, **107**, 1233-1271.

129. C. K. Chan, W. Zhao, A. Kahn and I. G. Hill, *Appl. Phys. Lett.*, 2009, **94**, 203306-203303.

130. P. Wei, J. H. Oh, G. Dong and Z. Bao, *J. Am. Chem. Soc.*, 2010, **132**, 8852-8853.

131. F. Huang, Y.-J. Cheng, Y. Zhang, M. S. Liu and A. K. Y. Jen, *J. Mater. Chem.*, 2008, **18**, 4495-4509.

132. A. W. Hains, J. Liu, A. B. F. Martinson, M. D. Irwin and T. J. Marks, *Adv. Funct. Mater.*, 2010, **20**, 595-606.

133. Y. Sun, X. Gong, B. B. Y. Hsu, H.-L. Yip, A. K. Y. Jen and A. J. Heeger, *Appl. Phys. Lett.*, 2010, **97**, 193310-193313.

134. R.-Q. Png, P.-J. Chia, J.-C. Tang, B. Liu, S. Sivaramakrishnan, M. Zhou, S.-H. Khong, H. S. O. Chan, J. H. Burroughes, L.-L. Chua, R. H. Friend and P. K. H. Ho, *Nat Mater*, 2010, **9**, 152-158.

135. P. E. Keivanidis, S.-H. Khong, P. K. H. Ho, N. C. Greenham and R. H. Friend, *Appl. Phys. Lett.*, 2009, **94**, 173303-173303.

136. S. X. Cai, J. C. Nabity, M. N. Wybourne and J. F. W. Keana, *Chem. Mat.*, 1990, **2**, 631-633.

137. M. M. Beerbom, B. Lägel, A. J. Cascio, B. V. Doran and R. Schlaf, *J. Electron Spec. and Rel. Phenom.*, 2006, **152**, 12-17.

138. N. Cho, H.-L. Yip, S. K. Hau, K.-S. Chen, T.-W. Kim, J. A. Davies, D. F. Zeigler and A. K. Y. Jen, *J. Mater. Chem.*, 2011, **21**, 6956-6961.

139. J. H. Oh, P. Wei and Z. Bao, *Appl. Phys. Lett.*, 2010, **97**, 243305-243303.

140. L. F. Drummy, R. J. Davis, D. L. Moore, M. Durstock, R. A. Vaia and J. W. P. Hsu, *Chem. Mat.*, 2011, **23**, 907-912.

141. P. D. Kazarinoff, P. J. Shamburger, F. S. Ohuchi and C. K. Luscombe, *J. Mater. Chem.*, 2010, **20**, 3040-3045.

142. N. Cho, H.-L. Yip, J. A. Davies, P. D. Kazarinoff, D. F. Zeigler, M. M. Durban, Y. Segawa, K. M. O'Malley, C. K. Luscombe and A. K. Y. Jen, *Adv. Energy Mater.*, 2011, **1**, 1148-1153.

143. F. S. Kim, X. Guo, M. D. Watson and S. A. Jenekhe, *Adv. Mater.*, 2010, **22**, 478-482.

144. K. J. Baeg, D. Khim, D. Y. Kim, S. W. Jung, J. B. Koo, I. K. You, H. Yan, A. Facchetti and Y. Y. Noh, *J. Polym. Sci., Part B: Polym. Phys.*, 2011, **49**, 62.

145. F. S. Bates and G. H. Fredrickson, *Phys. Today*, 1999, **52**, 32-38.

146. Y. Shinohara, K. Ohara, H. Nakanishi, Y. Imai and Y. Isoda, *Functionally Graded Materials Viii*, 2005, **492-493**, 141-144.

147. H. Bronstein, Z. Chen, R. S. Ashraf, W. Zhang, J. Du, J. R. Durrant, P. Shakya Tuladhar, K. Song, S. E. Watkins, Y. Geerts, M. M. Wienk, R. A. J. Janssen, T. Anthopoulos, H. Sirringhaus, M. Heeney and I. McCulloch, *J. Am. Chem. Soc.*, 2011, **133**, 3272-3275.

148. H. Yan, Z. Chen, Y. Zheng, C. Newman, J. R. Quinn, F. Dotz, M. Kastler and A. Facchetti, *Nature*, 2009, **457**, 679-686.

149. C. Vanpham, R. S. Macomber, H. B. Mark and H. Zimmer, *J. Org. Chem.*, 1984, **49**, 5250-5253.

150. E. Campaigne and R. C. Bourgeois, *J. Am. Chem. Soc.*, 1954, **76**, 2445-2447.

151. A. D. Becke, *J. Chem. Phys.*, 1993, **98**, 5648-5652.

152. C. Lee, W. Yang and R. G. Parr, *Phys. Rev. B*, 1988, **37**, 785-789.

153. M. J. Frisch, *Gaussian 03, revision E.01*, Gaussian, Inc., Pittsburgh, PA, 2003.

154. A. S. Molinari, H. Alves, Z. Chen, A. Facchetti and A. F. Morpurgo, *J. Am. Chem. Soc.*, 2009, **131**, 2462-2463.

155. W. Kaim, H. Tesmann and H. Bock, *Chem. Berichte*, 1980, **113**, 3221-3234.

156. M. He and F. Zhang, *J. Org. Chem.*, 2007, **72**, 442-451.

VITA

Peter D. Kazarinoff grew up in Ithaca, NY. In high school he was the bass player in a punk rock band, a varsity soccer captain, and an eagle scout. Peter attended Oberlin College for one year, where he played NCAA Division 3 soccer, hockey and lacrosse. He then transferred to Cornell University and majored in Chemistry. While at Cornell, he studied abroad in Sydney, Australia and moved there after graduation. Peter has a long-time interest in teaching, and started his professional teaching career at The Governor's Academy, the nation's oldest boarding school. While there, he converted a car to run on vegetable oil from the dinning hall. After research stints at CU Boulder, and UC Berkley, he arrived at the University of Washington and earned a PhD in Materials Science and Engineering working in the Luscombe Group on p-type and n-type semiconducting polymers. He currently lives in Seattle with his wife, daughter and a chicken named Baby.